

1 **Technical note: Surface fields for global environmental modelling**

2 Margarita Choulga¹, Francesca Moschini¹, Cinzia Mazzetti¹, Stefania Grimaldi², Juliana
3 Disperati³, Hylke Beck⁴, Peter Salamon², Christel Prudhomme¹

4 ¹European Centre for Medium-Range Weather Forecasts (ECMWF), Reading, RG2 9AX, United Kingdom

5 ²Joint Research Centre (JRC), European Commission, Ispra, 21027, Italy

6 ³Fincons Group, Vimercate, 20871, Italy

7 ⁴King Abdullah University of Science and Technology (KAUST), Thuwal, Saudi Arabia

8 *Correspondence to:* Margarita Choulga (margarita.choulga@ecmwf.int) and Christel Prudhomme
9 (christel.prudhomme@ecmwf.int)

10 **Abstract.** Climate change has resulted in more frequent occurrences of extreme events, such as flooding and
11 heavy snowfall, which can have a significant impact on densely populated or industrialised areas. Numerical
12 models are used to simulate and predict these extreme events, enabling informed decision-making and planning
13 to minimise human casualties and to protect costly infrastructure. LISFLOOD is an integrated hydrological model
14 underpinning the European and Global Flood Awareness Systems (EFAS and GloFAS, respectively) developed
15 by the Copernicus Emergency Management Service (CEMS). The CEMS_SurfaceFields_2022 dataset is a new
16 set of high-resolution surface fields at 1 and 3 arcminute resolution (approximately 2 and 6 km at the equator
17 respectively) based on a wide variety of high-resolution and up-to-date data sources. The 1 arcminute fields cover
18 Europe while the surface fields at 3 arcminute cover the global land surface (excluding Antarctica). The dataset
19 encompasses (i) catchment morphology and river networks, (ii) land use, (iii) vegetation cover type and properties,
20 (iv) soil properties, (v) lake information, and (vi) water demand. This manuscript details the complete workflow
21 used to generate the CEMS_SurfaceFields_2022 fields, including the data sources and methodology. Whilst
22 created together with upgrades to the open source LISFLOOD code, the CEMS_SurfaceFields_2022 fields can
23 be used independently for a wide range of applications, including as input to hydrological, Earth System or
24 environmental models, or for carrying out general analyses across spatial scales, ranging from global and regional
25 to local levels (especially useful for regions outside Europe), expected to improve accuracy, detail, and realism of
26 applications.

27 **1 Introduction**

28 Current numerical Earth system models are highly complex. Thanks to the availability of High Performance
29 Computers, cloud computing, and a wide range of high-resolution environmental data derived from the use of
30 ground, unconventional and satellite measurement sensors, numerical global models are even able to reach
31 kilometre-scale horizontal resolution. But increase in spatial resolution also means that the Earth system and
32 environmental models have to represent more surface and atmospheric processes and their interactions, which can
33 become challenging, for example in complex orographic areas. Model accuracy heavily depends on the quality of
34 the input surface fields (i.e. how realistic and up-to-date they are), and it is essential to minimise errors in surface
35 fields. New high-resolution (i.e. 10-100 m) surface datasets based on daily satellite observations are now
36 frequently released and continuously supported by e.g. the Copernicus program (e.g. Global Land Cover:
37 Buchhorn et al., 2021; GHSL-BUILT-S: Pesaresi and Politis, 2022; Schiavina et al., 2022), which helps in
38 achieving the goal of minimising surface field errors. It was shown, e.g. in Kimpson et al. (2023), that the use of
39 accurate and up-to-date underlying information to generate model's input surface fields can substantially reduce
40 skin temperature errors even at 30 km horizontal resolution (Kimpson et al., 2023).

41 Following the digital revolution of cloud archiving and computing, where data, software and information
42 technology (IT) infrastructure can be accessed by anyone from everywhere, the Earth systems and environmental
43 modelling community has also moved from codes developed by a single organisation and few contributors, to so-
44 called 'community models'. Community model's reference code is open for free use and/ or development
45 according to sharing principles. Such models include Joint UK Environmental Simulator JULES¹ (Best et al.,
46 2011; Clark et al., 2011; Marthews et al., 2022), OpenIFS² (Sparrow et al., 2021; Carver, 2022; Huijnen et al.,

¹ JULES is a land surface model whose development is coordinated by the UK Met Office and UKCEH.

² OpenIFS is a Numerical Weather Forecast model available to external users for research and training.

2022; Köhler et al., 2023), the Community Land Model CLM³ (Lawrence et al., 2019), and LISFLOOD-OS⁴ (Van Der Knijff and De Roo, 2008). To promote the seamless development of science, and facilitate research community efforts in working with the same code and input data, providing feedback, and improving the code and the data itself, powerful web-based platforms can be used. One of them is the Google Earth Engine (GEE; Gorelick et al., 2017), a free-of-charge platform that provides easy, web-based access to an extensive catalogue of satellite imagery and other geospatial data in an analysis-ready format. The data catalogue is embedded into Google computing platform that lets you easily implement all personal workflows, which facilitates global-scale analysis and visualization (GEE: FAQ, 2023). GEE was chosen for the generation of a new vast surface field set due to its high resolution data catalogue and powerful computation capabilities. This manuscript presents the methodology used to prepare the CEMS_SurfaceFields_2022 dataset containing all surface fields necessary to run the LISFLOOD-OS model at resolutions ~2 km at the equator or 1 arcminute (over Europe; 1 arcminute resolution at mid-latitude of the domain (47.50 N) is ~1.25 km) and ~6 km at the equator or 3 arcminute (globally). CEMS_SurfaceFields_2022 were used in the set-up of the Early Warning Systems of the Copernicus Emergency Management Service of the European Union for the European⁵ and global⁶ domains operational in December 2023 (EFASv5 and GloFASv4). Details on raw data collection, scientific protocol, and technical methods aim to allow the adequate understanding and interpretation of the surface field datasets. For any interested user it is possible to generate their own datasets by replicating or adapting the workflow to different fields, geographical domain, spatial resolution, or content as relevant for downstream application. The manuscript is structured as follows: Section 2 provides an overview of the surface fields, explains the criteria to select reference data, where and how they were processed, and outlines the general methodology to produce the surface fields; Section 3 to Section 8 details the reference data and specific methodology applied to each surface field category, including examples of application; Section 9 provides all the relevant information for data access; Section 10 discusses the challenges of creating a consistent high resolution continental and global scale set of surface fields and the opportunities disclosed by their availability.

2 Surface fields for distributed environmental modelling

2.1 General information

Environmental models, especially land surface and hydrological models, simulate how water moves across canopy, surface, subsurface, ground and eventually river channels using mechanistic equations that describe the physics of these processes. Each model represents processes with more or less complexity, depending on the model purpose and expected output (Rosbjerg and Madsen, 2006). With most represented terrestrial processes depending on the landscape, information describing the spatial variation in the geophysical and vegetation characteristics is needed. Such characteristics include morphological features (e.g. channel geometry, orography or slope), soil hydraulic property, land and vegetation features (e.g. ecosystem cover type, leaf area index (LAI), evaporation rates, crop type, planting and harvesting dates), and if relevant, human intervention information such as population density or type of water usage.

LISFLOOD is a semi-distributed, physically based hydrological model which has been designed for the modelling of rainfall-runoff processes in large and transnational catchments (Bates and De Roo, 2000; De Roo et al., 2000; De Roo et al., 2001; Van Der Knijff and De Roo, 2008; Van Der Knijff et al., 2010; Burek et al., 2013). In its most prominent application, LISFLOOD is used by the Copernicus Emergency Management Services' EFAS and GloFAS to provide medium range and seasonal riverine flow forecasts (Alfieri et al., 2020). LISFLOOD is also widely used for a variety of applications, including water resources assessment (drought forecast); analysis of the impacts of land use changes, river regulation measures, water management plans; climate change analysis (e.g. Vanham et al., 2021).

To facilitate users' uptake and enable the seamless development of science, LISFLOOD has been released as open source in 2019, i.e. LISFLOOD-OS. The open-source suite includes the LISFLOOD hydrological model and a set of auxiliary tools for model setup, calibration, and post-processing of the results. For instance, the pre-processor

³ CLM is an Earth System Model with strong climate component maintained by the National Centre for Atmospheric Research but available for use by the wider research community.

⁴ LISFLOOD-OS is a spatially distributed water resources model developed by the Joint Research Centre and available for use and development through a share code repository (available online: <https://ec-jrc.github.io/lisflood/#lisflood>; <https://ec-jrc.github.io/lisflood-code/>, last accessed: 21.01.2024).

⁵ European Flood Awareness System EFAS version 5 (Smith et al., 2016; information available online: <https://www.efas.eu/>, last accessed: 21.01.2024).

⁶ Global Flood Awareness System GloFAS version 4 (Hirpa et al., 2018; Alfieri et al., 2020; Harrigan et al., 2023; information available online: <https://www.globalfloods.eu/>, last accessed: 21.01.2024).

94 LISFLOOD-LISVAP can be used to compute evapotranspiration, which together with total precipitation and
95 average temperature, are the three meteorological variables strictly required as input to the hydrological model.
96 The modelling of runoff processes in different climates and socio-economic contexts then requires a set of raster
97 fields (i.e. set of surface fields presented in this manuscript) to provide information of terrain morphology, surface
98 water bodies, soil properties, land cover and land use features, water demand. The total number of fields range
99 between 66, when only the essential rainfall-runoff processes are modelled, to a total 108 for a more
100 comprehensive model set-up in which, for instance, lakes, reservoirs, water demand for anthropogenic use are
101 included (available online: <https://ec-jrc.github.io/lisflood-model/>, last accessed: 21.01.2024).
102 The main model's field (i.e. in technical for model operation/ running sense) is a 'mask' – a Boolean field that
103 defines model boundaries, i.e. grid cells over which the model performs calculations and grid cells which are
104 skipped (e.g. ocean grid cells). Whilst the surface fields described in this manuscript follow specific requirements
105 of the LISFLOOD-OS model, it is a source of versatile information that can be used for any environmental
106 modelling application, either directly, or following a transformation, as relevant, as a full set or as a few consistent
107 fields.

108 2.2 Reference data and methodology

109 To produce CEMS_SurfaceFields_2022 surface fields only open source, freely available, updated as recently as
110 possible, with recognised reference on their quality data sources were used (see Appendix 1 for all relevant
111 reference data details). Note that whilst the majority of surface fields contain no time element, vegetation and
112 water demand fields explicitly describe the annual cycle (vegetation, rice) or annual time evolution (water
113 demand) and therefore have more stringent requirements regarding the data source. Global single-source datasets
114 (e.g. Te Chow, 1959; Supit et al., 1994; Allen et al., 1998; Buchhorn et al., 2021) were favoured to regional and/
115 or multiple data sources that needed to be combined in order to produce the required data unless sub-set
116 information was of much better quality (e.g. Moiret-Guigand, 2021). CEMS_SurfaceFields_2022 surface fields
117 are based on 25 different data sources and consist of 140 gridded fields grouped into six following groups: (i)
118 catchment morphology and river network, (ii) land use, (iii) vegetation cover type and properties, (iv) soil
119 properties, (v) lake information, and (vi) water demand.

120 Considering the high resolution (i.e. hundreds of meters) and volume of data (i.e. GB) of most input datasets used
121 to generate the surface fields, a high performing data manipulation platform was needed. GEE (Gorelick et al.,
122 2017) was selected as it provides (embedded) a vast high resolution data catalogue (e.g. ready available MERIT
123 DEM elevation dataset, CGLS-LC100 and CLC2018 land cover datasets) and powerful computation capabilities.
124 It also allows to upload any raster and vector data (e.g. GeoTiff or shapefiles) and to conduct each surface field
125 tailored computations. All GEE scripts were written in JavaScript to produce GeoTiff files, which were converted
126 to the final file format (NetCDF) locally after transfer from GEE platform.

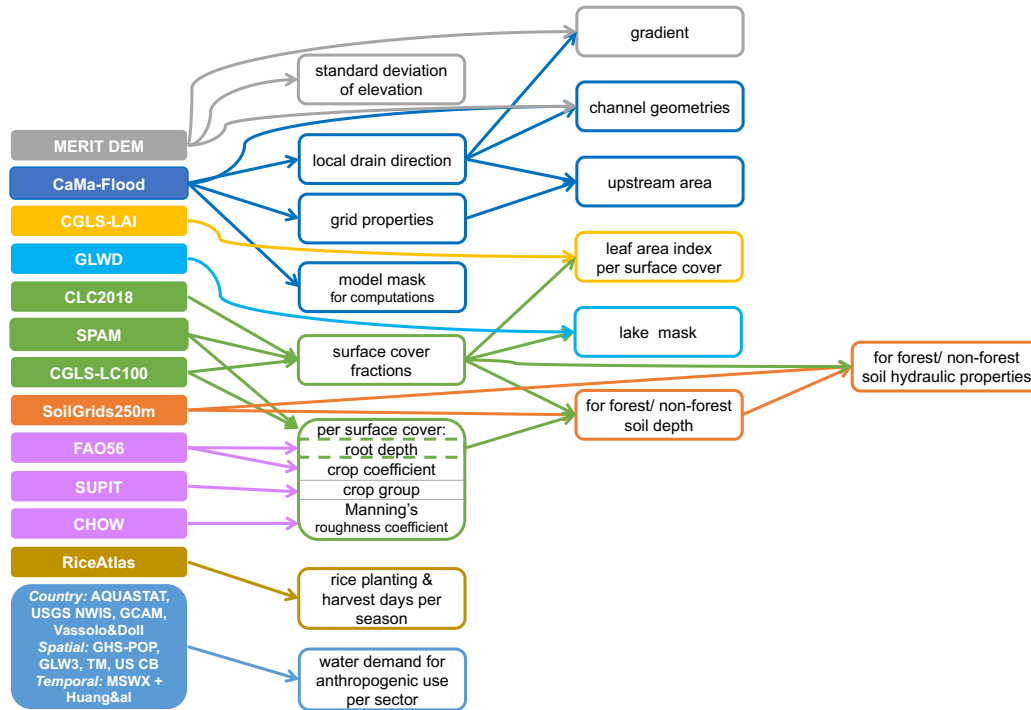
127 To ensure a consistent representation of physical processes at all scales, surface fields should be as coherent as
128 possible among each other – between variables and across scales. Coherency can be achieved by using, where
129 possible, the same input datasets to derive different field types (e.g. unique forest information input to create all
130 forest-related surface fields), and making sure spatial aggregation or disaggregation across scales results in
131 expected values. Figure 1 shows a simplified scheme that relates input datasets (e.g. CGLS-LC100) with the
132 resulting surface fields (e.g. surface cover fractions – forest, inland water, and sealed surface fraction fields), also
133 highlighting fields requiring intermediary and sequential steps (e.g. forest fraction is needed to create soil
134 parameter fields over forested and non-forested areas).

135 For processes with horizontal dependency such as river routing, the relationship between grid cells (e.g. how the
136 grid cells are connected) must be defined first so that all dependent fields can be generated on the same grid
137 coordinates, spatial resolution and using consistent input data. For example, local drainage direction (LDD)
138 defines how water moves across the model grid cells as a river drainage network (see Figure 2) and strongly
139 depends on elevation data (see Section 3 for more details). Because of the complex spatial dependency of a river
140 drainage network, LDD must be created directly from elevation data at the required grid and resolution and cannot
141 be resampled from a previous LDD field of a different grid and/ or resolution. It is then used to define information
142 on the river network, including upstream drainage area and gradient. Note that Figure 1 misses an arrow from
143 MERIT DEM to LDD only because this step was mainly done by CaMa-Flood developers (see Section 3.2 for
144 more details).

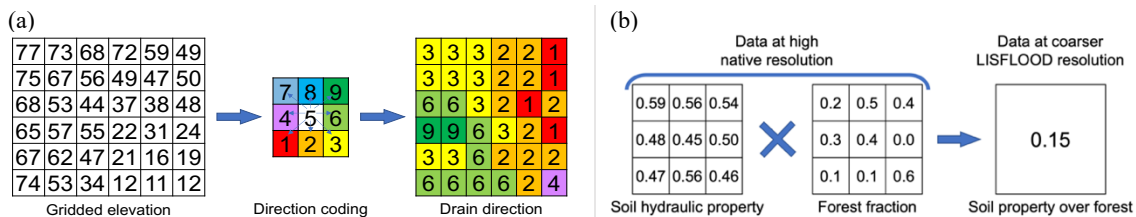
145 Four steps are involved in generating a particular surface field (see Table 1), with step 3 being the most complex
146 and varied (see Figure 2 for an example), and step 4 being necessary only for some model specifications (here as
147 required by LISFLOOD, see Table 2).

148 All techniques applied (see Table 1) to generate CEMS_SurfaceFields_2022 are reproducible to different input
149 data and/ or for different output data specifications. Further details on specific manipulations associated with each
150 field category are given in sections below as relevant. Each section has a table with exact data source used per
151 surface field, and step-by-step description of transformations applied to the data to compute the final fields

152 included in CEMS_SurfaceFields_2022 (full technical descriptions for all fields are explained in the LISFLOOD
 153 user guide, available online: https://ec-jrc.github.io/lisflood-code/4_Static-Maps-introduction/, last accessed:
 154 21.01.2024). Although the specific requirements for the dataset were defined by LISFLOOD for EFAS and
 155 GloFAS implementation, summarised in Table 2, they are consistent with requirements of any other
 156 environmental models. Regional examples of a sub-set of CEMS_SurfaceFields_2022 are provided to show the
 157 level of detail available at each resolution and field, and to emphasise the consistency through all the fields, a
 158 critical requirement for environment modelling and analysis. Examples are focusing on three regions of the world:
 159 the Po River (Europe), the Amazon River (South America) and the Brahmaputra River (Asia), with additional
 160 examples provided in Appendix 4.
 161



162
 163 **Figure 1. Flow chart connecting input datasets and surface fields created. Dashed border denotes intermediate fields,**
 164 **that are not part of the final dataset catalogue.**



165
 166 **Figure 2. Examples of data manipulation for (left column, plot a) transformation of elevation data into LDD (done**
 167 **within CaMa-Flood), and (right column, plot b) upscaling with weighted average for one final grid cell of soil hydraulic**
property over forested area.

168 **Table 1. The four steps of a particular surface field generation and associated data manipulations.**

Order	Description	Purpose	Function
1	Raw file preparation	Vector gridding, region merging	
		Upscaling (spatial/ temporal aggregation)	Arithmetic mean, mode, sum, standard deviation (weighted) resampling from auxiliary data
2	Unit conversion	Converting values from native to fraction per grid cell	Surface area, percentage or categorical to fractions per grid cell (see Appendix 2 for more details)
3	Value computation	Transforming	Mathematical equation/ function needed to generate the output variable
		Reprojecting	Interpolation (changing grid, preserving resolution in meters)
		Upscaling (spatial [default]/ temporal aggregation)	Arithmetic mean, mode, sum, standard deviation (weighted) resampling from auxiliary data (changing resolution, preserving grid)
		Downscaling (spatial [default]/ temporal disaggregation)	Nearest neighbour (changing resolution, preserving grid)
		Limiting	Force a minimum/ maximum value to satisfy e.g. calculation precision, physical meaning and/ or model requirement
4	Zero/ NoData filling	Replace zero/ NoData by the most appropriate values	LIGHT. Constant value, unweighted global mean, unweighted global mode
			DEEP. Values from next coarser resolution (up to an agreed maximum resolution); if still missing, method LIGHT

169
170

Table 2. Dataset files technical specifications.

Type	Specification
Format	NetCDF
Projection	EPSG:4326 - WGS84: World Geodetic System
Horizontal resolution	Europe: 1 arcminute (~1.86 km at the equator) [file size 4530x2970 grid cells]
	Globe: 3 arcminute (~5.57 km at the equator) [file size 7200x3600 grid cells]
Domain bound	Europe: [North = 72.25 N; South = 22.75 N; West = 25.25 W; East = 50.25 E]
	Globe: [North = 90.00 N; South = 90.00 S; West = 180.00 W; East = 180.00 E]
Missing value (i.e. NoData) location	Over land: none
	Over ocean: all ocean grid cells have missing value (i.e. ocean is masked based on 'mask' field)
Missing value (i.e. NoData) number	For Integer variable type: 0
	For Real variable type: -999999.0
Variable type	Integer: Int8
	Real: Float32

171 3 Catchment morphology and river network

172 3.1 General information

173 Morphology and channel shape information are essential for the computation of snow melting, temperature
174 scaling, and river routing. Alternatively, standard deviation of elevation and other orographic sub-grid parameters
175 are critical for radiation parametrization, especially for shadowing effect. Channel geometry fields are needed to
176 describe overbank inundation and infer inundated areas in wetland methane and soil carbon modelling. Land
177 morphology is derived from elevation and its variability within a single cell can be represented through slope,
178 standard deviation, aspect, etc. River drainage information, derived from elevation, is used to connect the model
179 cells according to the direction of the surface runoff, with channel geometry information used for routing
180 processes.

181 The dataset contains 14 morphology and river network variables (names in brackets in italics correspond to the
182 field names in the data repository):

- 183 • Morphologic information: local drainage direction (i.e. flow direction from one cell to another; *LDD*,
184 dimensionless), upstream drainage area (*upArea*, m²), grid cell area (*pixarea*, m²), grid cell length
185 (*pixleng*, m), standard deviation of elevation (*elvstd*, m), gradient (i.e. elevation gradient; *gradient*, m/m);
- 186 • Kinematic wave equation for routing: channel bottom width (*chanbw*, m), channel length (*chanlenght*,
187 m), channel gradient (*changrad*, m/m), Manning's roughness coefficient for channels (*chanman*, s/m^{1/3});
- 188 • River network information: channel mask (i.e. presence of river channel; *chan*, dimensionless), channel
189 side slope (i.e. channel's horizontal distance divided by vertical distance; *chans*, m/m);

- Open water evaporation: bankfull channel depth (*chanbnkf*, m), channel flood plain (i.e. width of the area where the surplus of water is distributed when the water level in the channel exceed the channel depth; *chanflpn*, m).

3.2 Reference data and methodology

Environmental models require an accurate description of terrain and hydro-morphology to represent the hydrodynamics at the spatial resolution of the model. Here all catchment morphology and river network fields are derived from (i) The Catchment-based Macro-scale Floodplain (CaMa-Flood) Global River Hydrodynamics Model v4.0 maps (further referred as CaMa-Flood), and (ii) The MERIT DEM: Multi-Error-Removed Improved-Terrain Digital Elevation Model v.1.0.3 (further referred as MERIT DEM). For reference data details see Appendix 1. All fields follow a complex sequential workflow (see Figure 3 and Table 1). Note that whilst some river network fields were already directly available from the CaMa-Flood catalogue (e.g. LDD, channel length), they had to be adapted to the specific requirements of LISFLOOD. Fields also had to be specifically consistent with an interconnected river network described by the D8 algorithm (O’Callaghan and Mark, 1984; Figure 2a) different to that used by the CaMa-Flood algorithm.

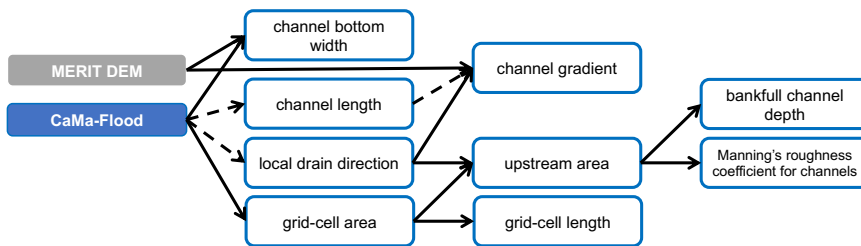


Figure 3. Workflow of complex manipulations to create some of the morphology and river network fields; solid arrows indicate a function transformation, dashed – modification of existing input data to LISFLOOD specifications.

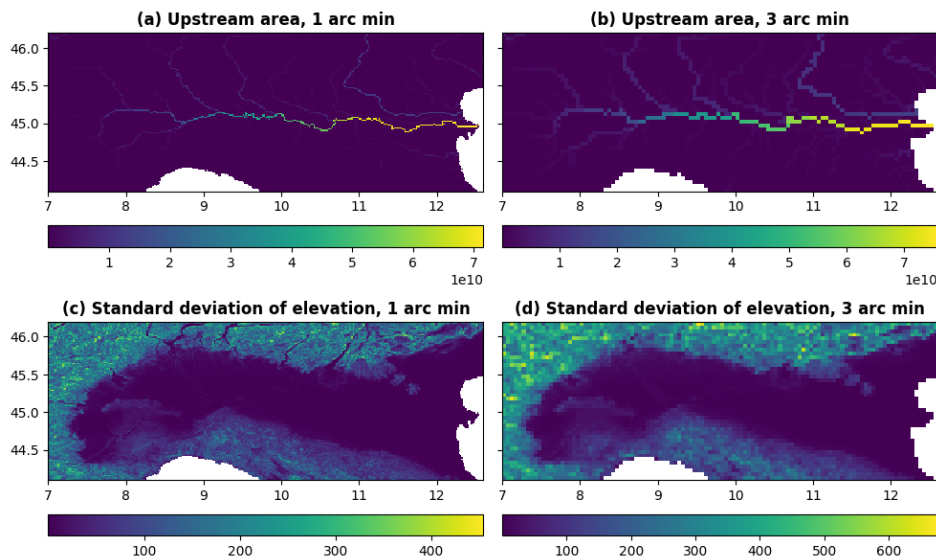
Table 1. Morphology and river network fields, their description, data source and applied transformation; * denotes transformation following Burek et al. (2014); name in brackets in *italics* next to each field corresponds to the name in the data repository.

Field type	Description	Data source (variable)	Transformation
Local drainage direction (<i>LDD</i>)	Connects every grid cell forming a river network from springs to mouth	CaMa-Flood (flwd)	Direction coding, ensuring grid cell connectivity
Grid cell area (<i>pixarea</i>)	Area of every grid cell	CaMa-Flood (flwd)	Grid cell area based on a given coordinate reference system and resolution
Grid cell length (<i>pixlength</i>)	Length of every grid cell	<i>pixarea</i>	$pixlength = \frac{pixarea}{resolution}$, where <i>resolution</i> – 1.86 km and 5.57 km for 1 and 3 arcminute respectively
Upstream drainage area (<i>upArea</i>)	Accumulated area of all connected grid cells of the LDD from springs (start; lowest values) to mouth (end; highest values)	<i>LDD</i> ; <i>pixarea</i>	PCRaster Accuflux function (Karssenberget al., 2010)
Standard deviation of elevation (<i>elvstd</i>)	Amount of elevation variation within a grid cell	MERIT DEM	Upscaling (spatial) with standard deviation
Gradient (<i>gradient</i>)	Elevation gradient between two connected grid cells	MERIT DEM; <i>LDD</i>	$gradient = \frac{abs(elv_{uc} - elv_{dc})}{D_{uc,dc}}$, where <i>elv</i> – elevation, <i>uc</i> and <i>dc</i> – upstream and downstream cell, <i>D_{uc,dc}</i> – distance between upstream and downstream cells
Channel bottom width (<i>chanbw</i>)	Width of the bottom of the channel	CaMa-Flood (width); <i>upArea</i>	Recomputing zero and negative values based on equation* $chanbw = upArea \cdot 0.0032$
Channel length (<i>chanlength</i>)	Length of river channel in each grid cell (can exceed grid-size to account for meandering river)	CaMa-Flood (rivlen)	No transformation was carried out

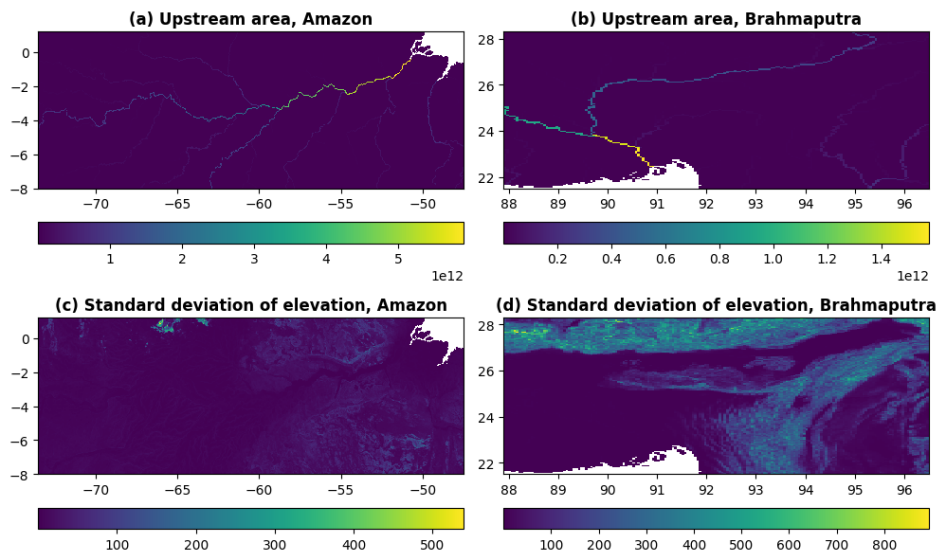
Channel gradient (<i>changrad</i>)	Gradient (slope) of river channel inside a grid cell	MERIT DEM; <i>LDD</i> ; <i>chanlength</i>	$changrad = \frac{abs(elv_{uc} - elv_{dc})}{chanlength_{uc}}$, where <i>elv</i> – elevation, <i>uc</i> and <i>dc</i> – upstream and downstream cell; Note: <i>LDD</i> is used to define <i>uc</i> and <i>dc</i>
Manning's roughness coefficient for channels (<i>chanman</i>)	Manning's roughness coefficient of river channel for each grid cell	MERIT DEM; <i>upArea</i>	Transformation based on equation* $chanman = 0.25 + 0.015 \cdot \min\left(\frac{50}{upArea_{km^2}}, 1\right) + 0.030 \cdot \min\left(\frac{elv_m}{2000}, 1\right)$, where <i>elv</i> – elevation, <i>km</i> ² and <i>m</i> – values in <i>km</i> ² and <i>m</i>
Channel mask (<i>chan</i>)	Channel presence in the grid cell indicator. Note LISFLOOD specific requirement to have channels in every 'mask' grid cell	'mask' (main model's field)	Channel mask is equal to 1 everywhere
Side slope (<i>chans</i>)	Slope of river banks (i.e. horizontal distance divided by vertical distance)		Side slope of all channels is 45°, hence side slope is equal to 1 everywhere
Bankfull channel depth (<i>chanbnkf</i>)	Channel depth (i.e. river bed depth)	<i>upArea</i>	Transformation based on equation* $chanbnkf = 0.27 \cdot upArea_{km^2}^{0.33}$, where <i>km</i> ² – values in <i>km</i> ²

211 3.3 Regional examples

212 Most fields in catchment morphology and river network category are quite technical and hard to interpret. The
 213 ones that can be easy digested are upstream area and standard deviation of elevation which are presented in Figure
 214 4 for Po River area in 1 and 3 arcminute resolution, and in Figure 5 for Amazon River and Brahmaputra River
 215 areas at 3 arcminute resolution. The field of standard deviation of elevation shows high level of detail over the
 216 Brahmaputra River and the benefit of high resolution dataset is clearly seen over the Po River.
 217



218
 219 **Figure 4. Upstream drainage area in square meters (upper row, plots a and b) and standard deviation of elevation in**
 220 **meters (lower row, plots c and d) at 1 arcminute (~1.9 km at the equator, left column, plots a and c) and 3 arcminute**
 221 **(~5.6 km at the equator, right column, plots b and d) resolution for Po River area in Italy.**



222
223
224
225

Figure 5. Upstream drainage area in square meters (upper row, plots a and b) and standard deviation of elevation in meters (lower row, plots c and d) at 3 arcminute (~ 5.6 km at the equator) resolution for Amazon River area (left column, plots a and c) and Brahmaputra River area (right column, plots b and d).

226 4 Land use fields

227 4.1 General information

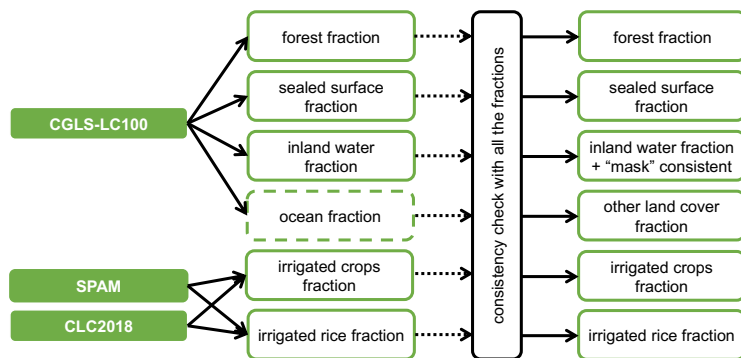
228 Land use is an essential component of environmental models. Many models use a sub-grid cell approach where a
 229 single grid cell can include several different land uses with each land use being subject to different prominent
 230 physical processes. This approach allows to keep a high level of accuracy when representing how different types
 231 of land cover affect e.g. the hydrological cycle (e.g. evaporation is different in urban areas compared to forests)
 232 while limiting the increase in computational time. Application of land surface fractions includes grid cell weighted
 233 average skin temperature calculations, biogenic flux calculations, urban planning, and climate mitigation plan
 234 preparation. For example, sealed surface fraction is necessary for carbon budget calculations and trace gas
 235 emissions in general, more explicitly for anthropogenic and residential emission calculations. Irrigated crop and
 236 irrigated rice fractions (combined with rice planting and harvesting days) useful for crop yield and methane
 237 emissions modelling.

238 The dataset differentiates between six different land uses (names in brackets in italics correspond to the field
 239 names in the data repository):

- 240 • Forest: areas where the main hydrological processes are canopy interception, evapotranspiration from
 241 canopies, canopies drainage and evapotranspiration, root uptake and evaporation from the soil (fraction
 242 of forest; *fracforest*, dimensionless fraction);
- 243 • Sealed surface: impervious areas where there is no water infiltration into the soil, i.e. water is
 244 accumulated in the surface depression, yet evaporates, but once the depression is full, water is transported
 245 by a surface runoff (fraction of sealed surface; *fracsealed*, dimensionless fraction);
- 246 • Inland water: open water bodies where the most prominent hydrological process is evaporation (fraction
 247 of inland water; *fracwater*, dimensionless fraction);
- 248 • Irrigated crops: areas used by agriculture – water is abstracted from ground water and surface water
 249 bodies to irrigate the fields. The main hydrological processes connected with the irrigated crops are
 250 canopy interception, evapotranspiration from canopies, canopies drainage and evapotranspiration, root
 251 uptake and evaporation from the soil (fraction of all irrigated crops, excluding rice; *fracirrigated*,
 252 dimensionless fraction);
- 253 • Irrigated rice: areas used to grow rice with flooded irrigation agricultural technique, when water is
 254 abstracted from the inland water bodies and delivered to the rice fields. The main hydrological processes
 255 connected with rice fields are soil saturation, flooding, rice growing phase, soil drainage phase (fraction
 256 of irrigated rice; *fracrice*, dimensionless fraction);
- 257 • Other land cover: used in canopy interception, evaporation from the canopies, canopy drainage, plant
 258 evapotranspiration, evaporation from the soil hydrological processes. The relative importance of these
 259 processes depends on the LAI (fraction of other cover types; *fracother*, dimensionless fraction).

260 **4.2 Reference data and methodology**

261 In models explicitly accounting for sub-grid variability, the fraction of each land use in every cell must be provided
 262 so that process representation for each land use can be weighted accordingly. Here the majority of land use fields
 263 are derived from The Copernicus Global Land Service (CGLS) Land Cover (LC) 100m map (further referred as
 264 CGLS-LC100). Irrigated crops and irrigated rice fractions are derived from (i) The Spatial Production Allocation
 265 Model (SPAM) – Global Spatially-Disaggregated Crop Production Statistics Data for 2010 v2.0 (further referred
 266 as SPAM2010), and (ii) The Coordination of Information on the Environment (CORINE) Land Cover (CLC)
 267 inventory for 2018 (further referred as CLC2018). For reference data details see Appendix 1. The derivation of
 268 fractions of the five land use classes used in LISFLOOD (and additional ocean fraction for consistency check)
 269 each follows specific steps (see Figure 6) summarised in Table 2. Note that LISFLOOD requires all ‘mask’ (main
 270 model’s field) grid cells to have at least one non-zero fraction type. Hence the extra step in the generation of the
 271 inland water fraction field was to set empty grid cells (i.e. grid cells that based on the data source are fully covered
 272 with ocean) as fully covered with inland water.
 273



274 **Figure 6. Workflow of complex manipulations to create land use fields; solid arrows indicate a function transformation,**
 275 **dotted – upscaling; dashed boxes indicate the intermediate fields used for other field generation.**
 276

277 **Table 2. Fraction of land use fields, their description, data source and applied transformations; ‘sum’ refers to the sum**
 278 **of all fractions except ‘other land cover fraction’; cells with bold italics show required intermediate fields; name in**
 279 **brackets in italics next to each field corresponds to the name in the data repository.**

<i>Field type</i>	<i>Description</i>	<i>Data source (variable)</i>	<i>Transformation (in order)</i>
Forest fraction <i>(fracforest)</i>	Evergreen and deciduous needle leaf and broad leaf tree areas	CGLS-LC100 (tree-coverfraction)	Unit conversion % to fraction; Reprojecting and upscaling to final grid and resolution with mean; Consistency check with other fractions
Sealed surface fraction <i>(fracsealed)</i>	Urban areas, characterizing the human impact on the environment	CGLS-LC100 (urban-coverfraction)	Unit conversion % to fraction, scaled by 0.75 ⁷ ; Reprojecting and upscaling to final grid and resolution with mean; Consistency check with other fractions
Inland water fraction <i>(fracwater)</i>	Rivers, freshwater and saline lakes, ponds and other permanent water bodies over the continents	CGLS-LC100 (water-permanent-coverfraction)	Force Fox Basin and Caspian Sea to be fully covered with water; Unit conversion % to fraction; Reprojecting and upscaling to final grid and resolution with mean; Consistency check with other fractions; Cross-checking with ‘mask’ and forcing empty grid cells as inland water
Irrigated crops fraction <i>(fracirrigated)</i>	Irrigated areas of all possible crops excluding rice	SPAM (spam2010v1r0_global_physical-area_CROP_i, 41 crops rice excluding)	Shapefile gridding to its native resolution (~10 km); Unit conversion ha to fractions; Reprojecting and downscaling to CLC2018 grid and resolution (~100 m) with nearest neighbour
		CLC2018 (landcover = ‘212’)	Unit conversion class to fraction
			Merging SPAM- and CLC2018-derived fractions, priority to CLC2018;

⁷ For the sealed surface fraction, it is assumed that water can infiltrate in roughly 25 % of urban areas at kilometre scale through e.g. trees along the road, bushes along the fence, grass or moss between concrete tiles or cobble stones.

			Reprojecting and upscaling to final grid and resolution with mean; Consistency check with other fractions
Irrigated rice fraction (<i>fracrice</i>)	Irrigated areas of rice	SPAM (spam2010v1r0_global_physiocal-area_RICE_i)	Shapefile gridding to its native resolution (~10 km); Unit conversion ha to fractions; Reprojecting and downscaling to CLC2018 grid and resolution (~100 m) with nearest neighbour
		CLC2018 (landcover = '213')	Unit conversion class to fraction
			Merging SPAM- and CLC2018-derived fractions, priority to CLC2018; Reprojecting and upscaling to final grid and resolution with mean; Consistency check with other fractions
Other land cover fraction (<i>fracother</i>)	Agricultural areas, non-forested natural area, pervious surface of urban areas	Non-negative residual from 1 subtracting 'sum' of all other fractions	$fracother = \max((1 - sum), 0)$
Ocean fraction (<i>fracocean</i>)	Oceans	CGLS-LC100 (discrete_classification = '200')	Unit conversion class to fraction; Forcing NoData to zero over 'mask' grid cells, otherwise – fully covered; Reprojecting and upscaling to final grid and resolution with mean; Consistency check with other fractions

280

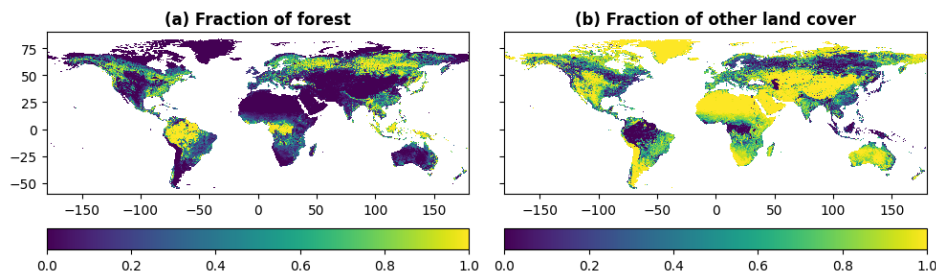
281 To ensure consistency between fractions, the sum of all fraction fields must be 1 at any resolution. When sum is
282 greater than 1, the inland water fraction value is assumed correct (input data corrected prior computation over Fox
283 Basin and Caspian Sea) and all other fractions are corrected (*fracXX*) following Eq. (1):

$$284 \quad fracXX = fracXX_{raw} \left(1 - \frac{fracwater_{raw} + fracocean_{raw} + fracforestr_{raw} + fracsealed_{raw} + fracirrigated_{raw} + fracrice_{raw} - 1}{fracforest_{raw} + fracsealed_{raw} + fracirrigated_{raw} + fracrice_{raw}} \right), \quad (1)$$

285 where *raw* refers to the original (i.e. before consistency check) fraction of *XX* which can be the forest, irrigated
286 crops, rice and sealed surfaces.

287 The generated fraction fields, e.g. forest (see Figure 7a) and other land cover (see Figure 7b), have generally good
288 consistency with other up-to-date products like ESA CCI Land Cover time-series v2.0.7 (ESA CCI map viewer
289 <https://maps.elie.ucl.ac.be/CCI/viewer/>, last accessed: 21.01.2024; Defourny et al., 2017).

290



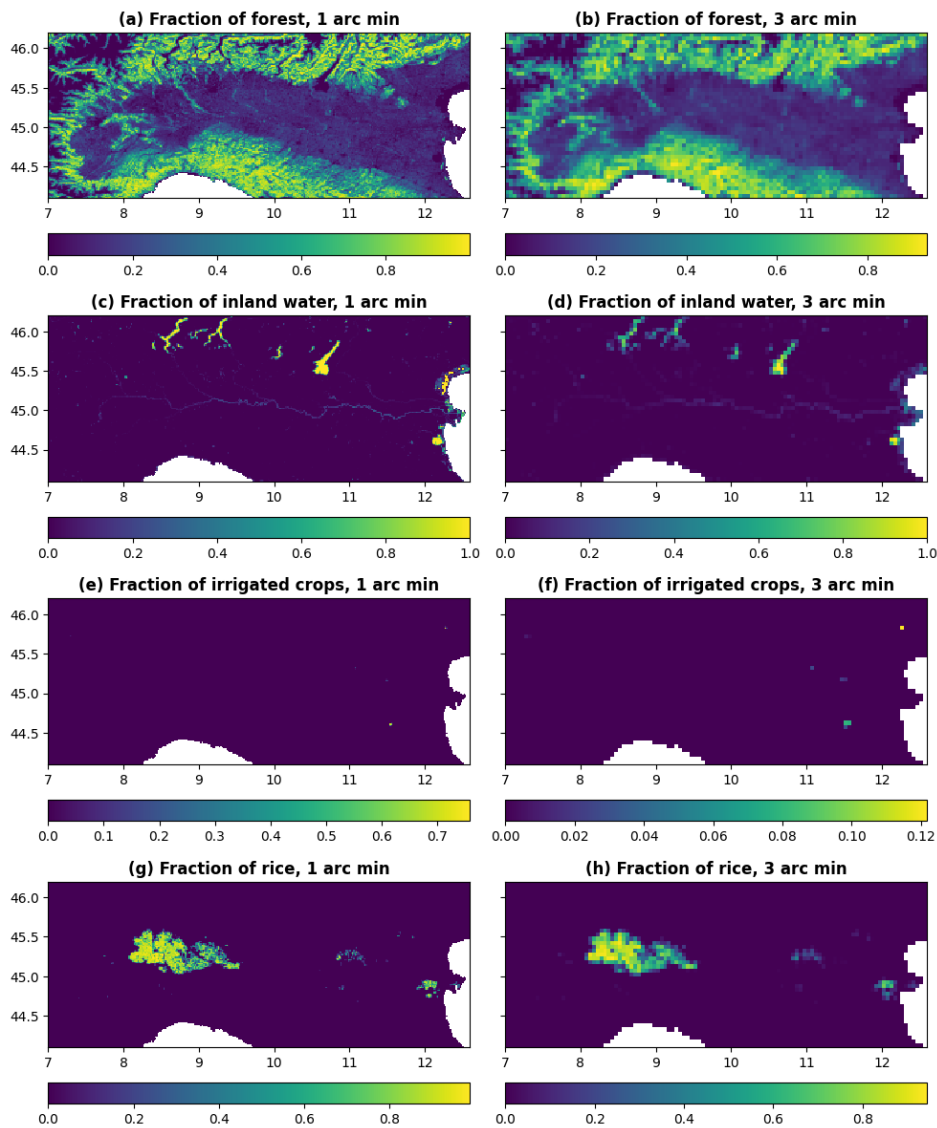
291

292 **Figure 7. Fraction of forest (left column, plot a) and fraction of other land cover (right column, plot b) at 3 arcminute**
293 **(~5.6 km at the equator) resolution for global region.**

294 4.3 Regional examples

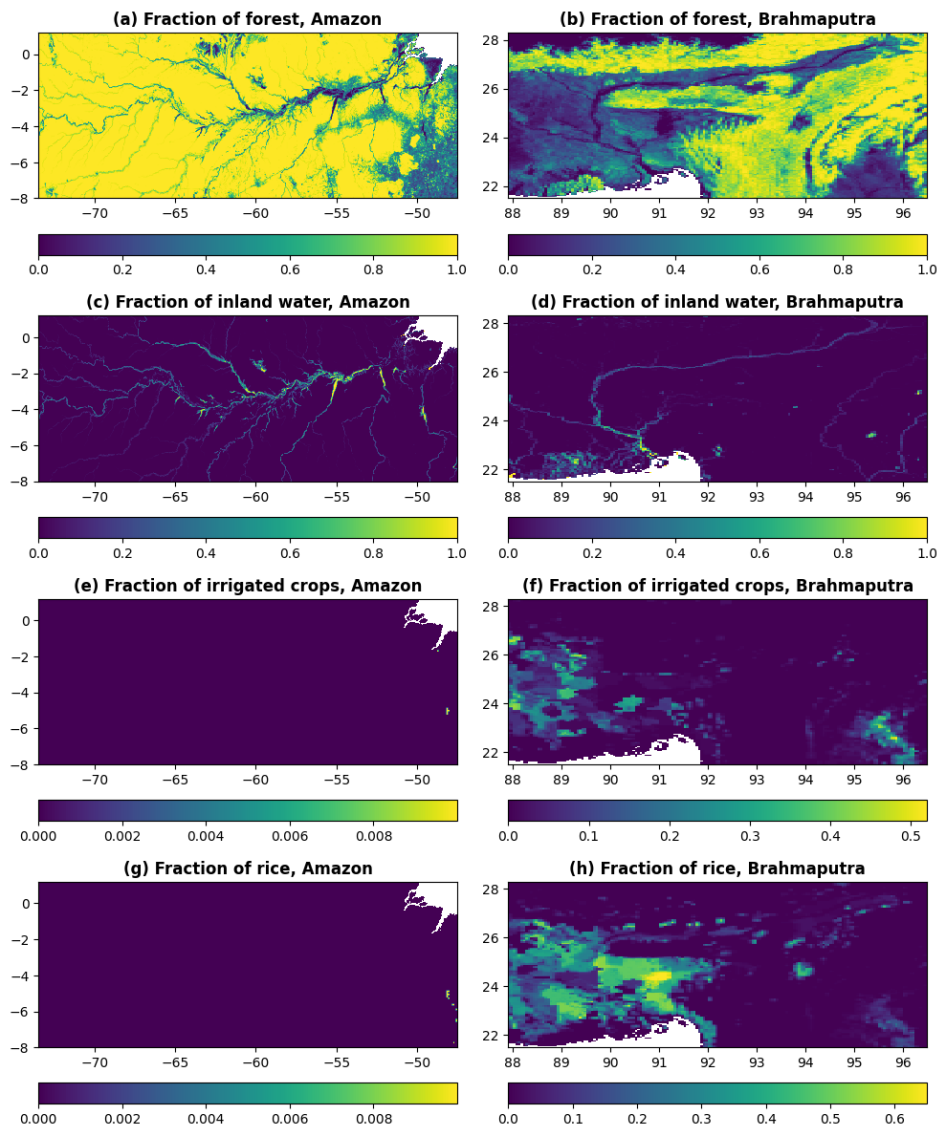
295 All fields in land use category are easy to interpret as they represent the fraction of grid cell covered by one or
296 another surface cover type. The most interesting ones are fraction of forest, fraction of inland water, fraction of
297 irrigated crops, and fraction of rice. These fractions are presented in Figure 8 for Po River area in 1 and 3 arcminute
298 resolution, and in Figure 9 for Amazon River and Brahmaputra River areas at 3 arcminute resolution. Figures
299 show high level of detail visible for the fields of fraction of forest and fraction of inland water (e.g. Amazon River)
300 especially at the highest spatial resolution (Po River).

301



302
303
304
305
306

Figure 8. Fraction of forest (upper row, plots a and b), fraction of inland water (second row, plots c and d), fraction of irrigated crops (third row, plots e and f), and fraction of rice (lower row, plots g and h) at 1 arcminute (~1.9 km at the equator, left column, plots a, c, e and g) and 3 arcminute (~5.6 km at the equator, right column, plots b, d, f and h) resolution for Po River area in Italy.



307
 308 **Figure 9.** Fraction of forest (upper row, plots a and b), fraction of inland water (second row, plots c and d), fraction of
 309 irrigated crops (third row, plots e and f), and fraction of rice (lower row, plots g and f) at 3 arcminute (~5.6 km at the
 310 equator) resolution for Amazon River area (left column, plots a, c, e and g) and Brahmaputra River area (right column,
 311 plots b, d, f and h).

312 5 Vegetation properties

313 5.1 General information

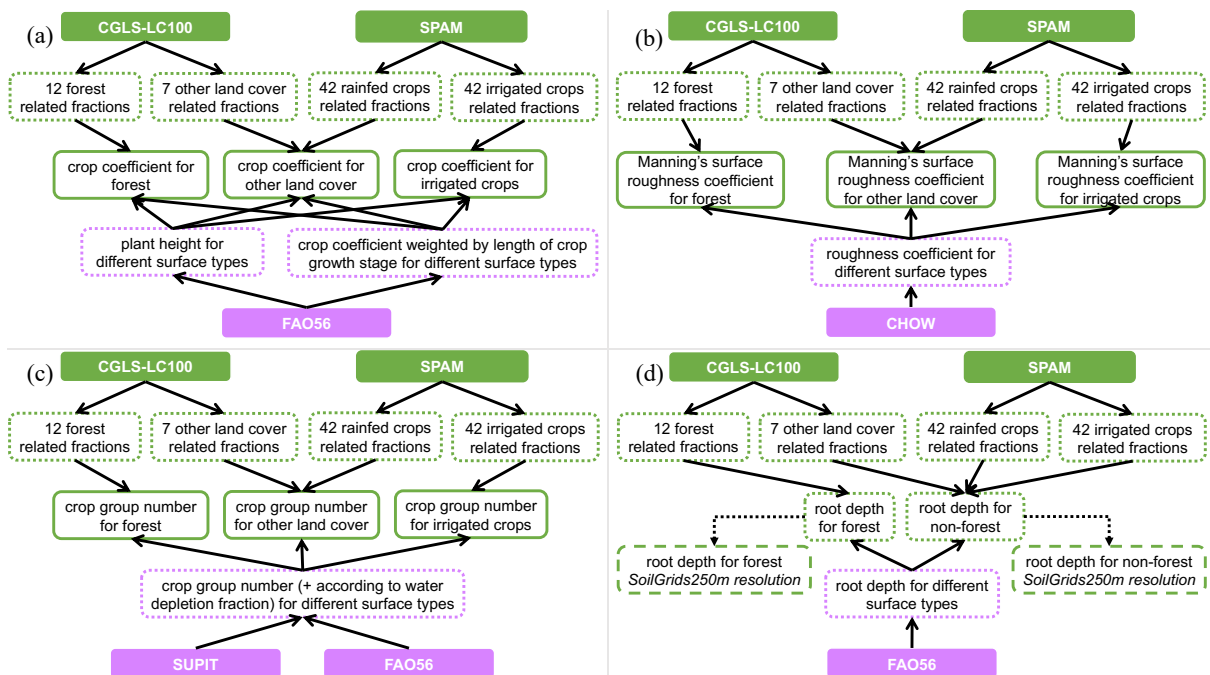
314 Vegetation-related information contributes to the computation of precipitation interception, evaporation,
 315 transpiration, and root water uptake. Depending on the model, vegetation dynamics can be represented with
 316 different degrees of complexity including in hydrology processes, vegetation growth and feedback on climate
 317 (Bonan et al., 2002). Rice being the world's most important food crop and having specific water demands, its
 318 water cycle is often considered explicitly. Rice planting and harvesting dates being critical information to
 319 represent the inter-annual variability in its water demand, provided the maximum three growing seasons. The
 320 variables allow to model how vegetation affects the hydrology, with a particular focus on root water uptake and
 321 transpiration depending on vegetation type and vegetation state (e.g. water stress conditions). For example, the
 322 crop group number depends on the critical amount of soil moisture below which water uptake from plants is
 323 reduced as they start closing their stomata. Alternative use of fields such as the Leaf Area Index LAI includes
 324 biomass allocation, which can be used for fire danger forecasting, and carbon stock monitoring. Rice planting/
 325 harvesting days are important for yearly cycle of methane modelling.

326 The dataset describes vegetation properties through four variables (note that LAI consists in total of 36 10-day
 327 average fields) for each of forest (*_f*), irrigated crops (*_i*) and other land cover types (*_o*), and another six (two
 328 types times three seasons) variables for rice (names in brackets in italics correspond to the field names in the data
 329 repository):

- 330 • Transpiration rate: crop coefficient (*cropcoef_f*, *cropcoef_i*, *cropcoef_o*, dimensionless);
- 331 • Water uptake: crop group number (*cropgrpn_f*, *cropgrpn_i*, *cropgrpn_o*, dimensionless);
- 332 • Surface runoff generation and water routing: Manning’s surface roughness coefficient (*manning_s_f*,
 333 *manning_s_o*, $s/m^{1/3}$), rice planting and harvesting days (*riceplantingday1*, *riceplantingday2*,
 334 *riceplantingday3*, calendar day number; *riceharvestday1*, *riceharvestday2*, *riceharvestday3*, calendar
 335 day number);
- 336 • Water interception and evaporation: leaf area index (*laif*, *laii*, *laio*, m^2/m^2).

337 5.2 Reference data and methodology

338 In complement to the land use fraction, the distribution of vegetation type and characteristics is required to capture
 339 the difference in environmental processes such as water intake of evaporation to be represented accurately. Here
 340 the vegetation properties are derived from many data sources using maps to account for the species spatial
 341 distribution (i.e. CGLS-LC100 and SPAM2010) and tables to obtain associated hydro-dynamics properties for
 342 crops, e.g. (i) The Food and Agriculture Organisation (FAO) of the United Nations Irrigation and Drainage Paper
 343 No. 56 (further referred as FAO56), and (iv) The Wofost 6.0 crop simulation model description (further referred
 344 as SUPIT); for river hydraulics The Open-Channel Hydraulics manual (further referred as CHOW). Time
 345 evolution of vegetation is based on The Copernicus Global Land Service (CGLS) Leaf Area Index (LAI) 1km
 346 Version 2 collection (further referred as CGLS-LAI); time evolution of crops is based on The RiceAtlas v3 (further
 347 referred as RiceAtlas). For reference data details see Appendix 1. This requires assumptions to be made in case
 348 different sources did not contain the same information, and transformations to be applied depending on the
 349 vegetation type. The main data sources and general transformation steps (see Figure 10) to derive the 18 vegetation
 350 properties fields are summarised in Table 3 and following text. Note that ‘crop group number’ variable
 351 corresponds to a water depletion value and can be averaged across different crop types.
 352



353 **Figure 10. Workflow of complex manipulations to create some of the vegetation property fields, e.g. crop coefficient**
 354 **(left column, upper row, plot a), Manning’s surface roughness coefficient (right column, upper row, plot b), crop group**
 355 **number (left column, lower row, plot c), root depth (right column, lower row, plot d); solid arrows indicate a function**
 356 **transformation, dotted – upscaling; dashed boxes indicate the intermediate fields used for other field generation, dotted**
 357 **– the fields only used for the vegetation-related fields.**

358 **Table 3. Vegetation property fields, their description, data source and applied transformations; cells with bold italics**
 359 **show required intermediate fields; name in brackets in italics next to each field corresponds to the name in the**
 360 **repository.**

<i>Field type</i>	<i>Description</i>	<i>Data source</i>	<i>Transformation (in order)</i>
Crop coefficient for forest, irrigated crops and other land cover type (<i>cropcoef_f</i> , <i>cropcoef_i</i> , <i>cropcoef_o</i>)	Ratio between the potential (reference) evapotranspiration rate, in mm/day, and the potential evaporation rate of a specific crop (averaged by time and ecosystem type)	CGLS-LC100 (discrete_classification = '111', '112', '113', '114', '115', '116', '121', '122', '123', '124', '125', '126' [forest types], '20', '30', '40', '60', '70', '90', '100' [other land cover types])	Force Fox Basin and Caspian Sea to be fully covered with water; Unit conversion class to fraction (in total 12 forest related and 7 other land cover related fraction fields); Reprojecting and upscaling to final grid and resolution with mean
		SPAM (spam2010v1r0_global_physical-area_CROP_i/r, 42 crops, 'i' – irrigated, 'r' – rainfed)	Shapefile gridding to its native resolution (~10 km); Unit conversion ha to fractions (in total 42 irrigated crop related and 42 rainfed crop related fraction fields); Reprojecting and downscaling to final grid and resolution with nearest neighbour; Limiting values to 0.0-1.0 interval
		FAO56 (Table 11, 12 – information on crop coefficient and crop height); Intara et al. (2018); Burek et al. (2014)	Average crop coefficient value across climate zones for each crop growing stage and crop/ land cover type; Weighted average of crop coefficient per different crop growth stages (weighted by stage duration in days if available, otherwise mean); Average crop height value across climate zones for each crop/ land cover type
			Weighted average of relevant crop coefficient for forest, irrigated crops and other land cover type (weighted by crop height and fraction) following Eq. (2); Note: for other land cover type computation of crop coefficient of all rainfed crops is used for CGLS-LC100 (discrete_classification = '40'); Zero/ NoData filling with global mean
Crop group number for forest, irrigated crops and other land cover type (<i>cropgrp_n_f</i> , <i>cropgrp_n_i</i> , <i>cropgrp_n_o</i>)	Represents a vegetation type and is an indicator of its adaptation to dry climate (averaged by ecosystem type)	CGLS-LC100 (discrete_classification = '111', '112', '113', '114', '115', '116', '121', '122', '123', '124', '125', '126' [forest types], '20', '30', '40', '60', '70', '90', '100' [other land cover types])	Same steps as for crop coefficient
		SPAM (spam2010v1r0_global_physical-area_CROP_i/r, 42 crops, 'i' – irrigated, 'r' – rainfed)	Same steps as for crop coefficient
		FAO56 (Table 22 – information on crop depletion fraction); SUPIT (Table 6.1, 6.2 – information on crop groups); Burek et al. (2014)	Applying function (SUPIT) to water depletion fraction (FAO56) for each crop/ land cover type $cropgrp_n = 10 \cdot fr_{dep} - 1.5$, where fr_{dep} – water depletion fraction; Limiting values to 1.0-5.0 interval; Note: if fr_{dep} missing – using precomputed crop group number (Burek et al., 2014)
			Same steps as for crop coefficient, but in Eq. (2) weighted by fraction only
Manning's surface roughness coefficient for forest and other land cover type (<i>mannings_f</i> , <i>mannings_o</i>)	Roughness or friction applied to the flow by the surface on which water is flowing (averaged by ecosystem type)	CGLS-LC100 (discrete_classification = '111', '112', '113', '114', '115', '116', '121', '122', '123', '124', '125', '126' [forest types], '20', '30', '40', '60', '70', '90', '100' [other land cover types])	Same steps as for crop coefficient
		SPAM (spam2010v1r0_global_physical-area_CROP_i/r, 42 crops, 'i' – irrigated, 'r' – rainfed)	Same steps as for crop coefficient

		CHOW (Table 5, 6 – information on roughness coefficient n); Burek et al. (2014)	Matching roughness coefficient for each crop/ land cover type
			Same steps as for crop coefficient, but in Eq. (2) weighted by fraction only
Leaf area index for forest, irrigated crops and other land cover type (<i>laif</i> , <i>lail</i> , <i>laio</i>)	Defined as half the total area of green elements of the canopy per unit horizontal ground area m ² /m ² (10-day average; 36 fields in total)	CGLS-LAI 10-day average for 2010-2019; <i>fracforest</i> ; <i>fracirrigated</i> ; <i>fracother</i>	Upscaling to final temporal resolution (in total 36 LAI fields); Reprojecting and upscaling to final grid and spatial resolution with unweighted mean; Filtering sparse areas of relevant fractions $fr < 0.7$, where fr – fraction; NoData filling DEEP (upscaling to 1, 3, 15 arcminute, 1, 3, 15, 60 degrees spatial resolution with unweighted mean; replacing NoData at final resolution with first available precomputed less coarser resolution, if not – with zero)
Rice planting day (<i>riceplantingday1</i> , <i>riceplantingday2</i> , <i>riceplantingday3</i>)	Most probable day of the year when rice is planted for the first, second and third time	RiceAtlas (PLANT_PKn, 3 seasons)	Ordering planting seasons by increasing Julian day (in total 3 planting dates per spatial unit); Shapefile gridding to final grid and spatial resolution (in total 3 fields); Note: if less than 3 seasons – repeating last available planting/ harvesting seasons date; NoData filling with global unweighted mode date of first planting/ harvesting season (i.e. 105 – 15 th April/ 227 – 15 th August)
Rice harvest day (<i>riceharvestday1</i> , <i>riceharvestday2</i> , <i>riceharvestday3</i>)	Most probable day of the year when rice is harvested after planting for the first, second and third time	RiceAtlas (HARV_PKn, 3 seasons)	
Root depth for forest and non-forest (<i>root_depth_f</i> , <i>root_depth_o</i>)	Deepest soil depth reached by the crop roots	CGLS-LC100 (discrete_classification = ‘111’, ‘112’, ‘113’, ‘114’, ‘115’, ‘116’, ‘121’, ‘122’, ‘123’, ‘124’, ‘125’, ‘126’ [forest types], ‘20’, ‘30’, ‘40’, ‘60’, ‘70’, ‘90’, ‘100’ [other land cover types])	Same steps as for crop coefficient
		SPAM (spam2010v1r0_global_physical-area_CROP_i/r, 42 crops, ‘i’ – irrigated, ‘r’ – rainfed)	Same steps as for crop coefficient
		FAO56 (Table 22 – information on crop rooting depth); Burek et al. (2014)	Matching rooting depth for each crop/ land cover type
			Same steps as for crop coefficient, but in Eq. (2) weighted by fraction only; Downscaling to native SoilGrids250m resolution with nearest neighbour (for soil depth calculations)

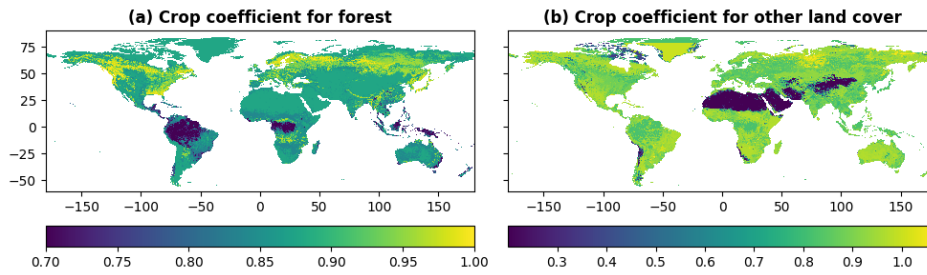
361
362
363
364
365
366
367
368
369
370
371
372
373

The final step of the crop coefficient, crop group number, Manning’s surface roughness coefficient, and additional crop height (for crop coefficient calculation) and root depth (for soil depth calculation, see Section 6.2) for forest, irrigated crops and other land cover type is to compute weighted average of their components (e.g. different forest types) following Eq. (2):

$$K = \frac{A_1 \cdot fr_1 \cdot K_1 + A_2 \cdot fr_2 \cdot K_2 + \dots + A_N \cdot fr_N \cdot K_N}{A_1 \cdot fr_1 + A_2 \cdot fr_2 + \dots + A_N \cdot fr_N} \quad (2)$$

where A is a scaling parameter (equals 1, except for crop coefficient where it equals to crop height), fr refers to the fraction of crop or land cover type, K – default (i.e. source table based) variable in question values, $1..N$ – number of crop or land cover types included in the field (i.e. for forest $N=12$, irrigated crops $N=41$, other land cover type $N=7$ and for CGLS-LC100 type ‘40’ (cropland) default values are based on 42 rainfed crops).

The generated vegetation property fields, e.g. crop coefficient for forest (see Figure 11a) and other land cover (see Figure 11b), follow main features of e.g. generated forest fraction.

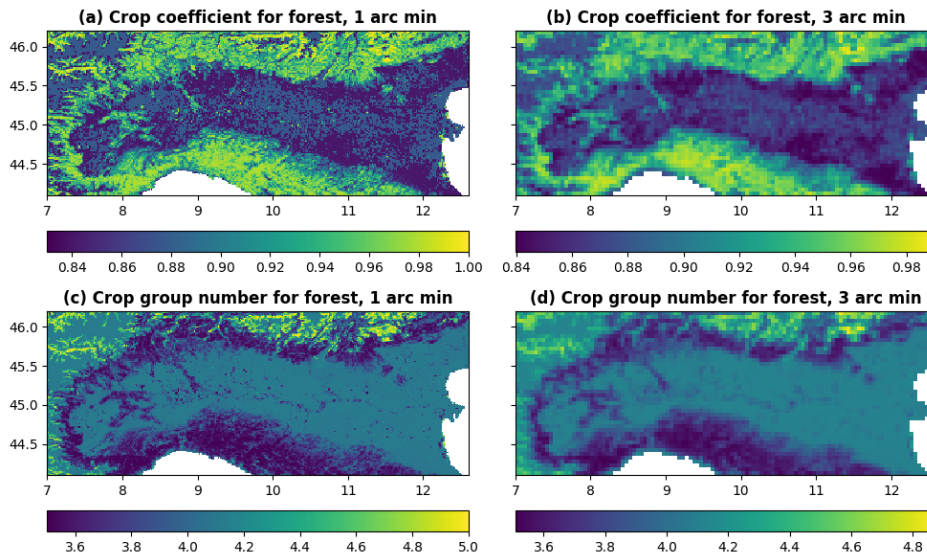


374
375
376

Figure 11. Crop coefficient for forest (left column, plot a) and crop coefficient for other land cover type (right column, plot b) at 3 arcminute (~5.6 km at the equator) resolution for global region.

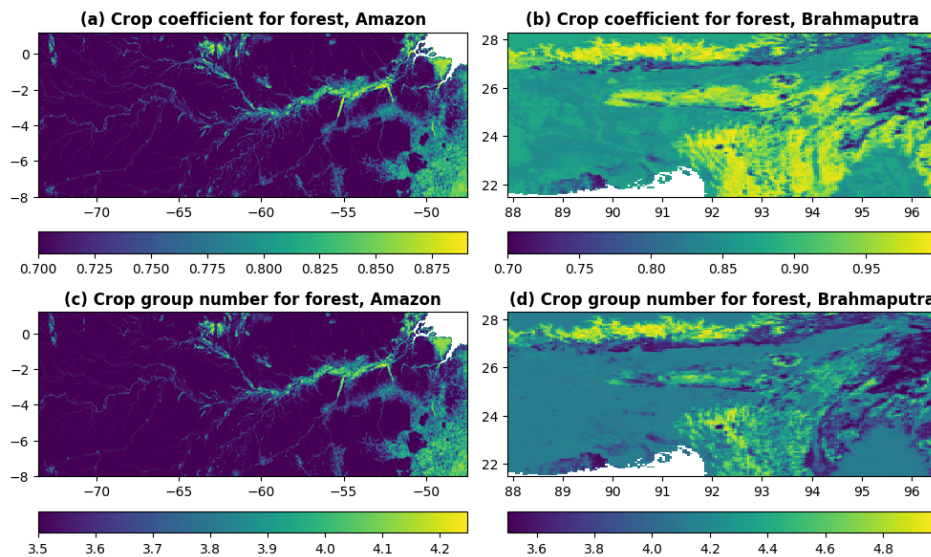
377 5.3 Regional examples

378 All fields in the vegetation properties category are complementary to the land use fractions, and help to understand
 379 for example the difference in evaporation water intake. The fields easiest to interpret are the crop coefficient and
 380 the crop group number which are presented for forest in Figure 12 for Po River area in 1 and 3 arcminute
 381 resolution, and in Figure 13 for Amazon River and Brahmaputra River areas at 3 arcminute resolution. For
 382 example, fields of crop group number for forest (i.e. different forest types) show transition of vegetation resilience
 383 towards dry conditions in the Brahmaputra River area.
 384



385
386
387
388

Figure 12. Crop coefficient for forest (upper row, plots a and b) and crop group number for forest (lower row, plots c and d) at 1 arcminute (~1.9 km at the equator, left column, plots a and c) and 3 arcminute (~5.6 km at the equator, right column, plots b and d) resolution for Po River area in Italy.



389
390
391
392 **Figure 13. Crop coefficient for forest (upper row, plots a and b) and crop group number for forest (lower row, plots c and d) at 3 arcminute (~5.6 km at the equator) resolution for Amazon River area (left column, plots a and c) and Brahmaputra River area (right column, plots b and d).**

393 6 Soil properties

394 6.1 General information

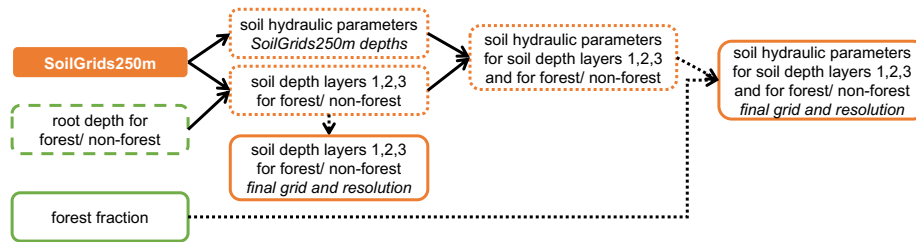
395 In land surface and distributed hydrological models, the water movement, storage and plants' water-uptake from
396 the soil are often described by the soil / water retention curve (SWRC). The SWRC is derived empirically by
397 measuring how water is retained and released by different soil types. Throughout time different SWRC have been
398 developed and integrated into models. The most widely applied are Van Brooks and Corey (Brooks and Corey,
399 1964), Fredlund and Xing (Fredlund and Xing, 1994), van Genuchten (van Genuchten, 1980), and Gardner
400 (Gardner, 1956) SWRCs. Different SWRC equations require different parameters, some shared between different
401 SWRC concepts, e.g. referring to physical soil characteristics such as water saturated and unsaturated content,
402 hydraulic conductivity and pore size, others uniquely describing the SWRC function shape, not directly related to
403 soil properties. Often, for computational reasons, the soil profile from ground level to bedrock depth is sliced into
404 layers, at the modeller's choice, and the SWRC function is applied to each soil layer. Alternative use of soil
405 properties is for soil moisture calculations.

406 The dataset includes variables required to apply the Van Genuchten SWRC equations (van Genuchten, 1980) to
407 describe the water dynamics through a vertical soil profile composed of three layers (1, 2, 3). Each variable is
408 required for each soil layer and for forest (_f) or non-forest (_o) land use, with different soil depth in forest (_f)
409 and non-forest (_o) areas following root depth values from Allen et al. (1998), referred as FAO56, (total of 29
410 variables; names in brackets in italics correspond to the field names in the data repository):

- 411 • Soil profile: surface layer depth (*soildepth1_f, soildepth1_o*, mm), middle layer depth (*soildepth2_f,*
412 *soildepth2_o*, mm), subsoil depth (*soildepth3_f, soildepth3_o*, mm);
- 413 • Soil hydraulic properties: saturated (*thetas1_f, thetas1_o, thetas2_f, thetas2_o, thetas3, m³/m³*) and
414 residual (*thetar1, thetar2, thetar3, m³/m³*) volumetric soil moisture content, pore size index (*lambda1_f,*
415 *lambda1_o, lambda2_f, lambda2_o, lambda3, dimensionless*), Van Genuchten equation parameter
416 (*genual_f, genual_o, genua2_f, genua2_o, genua3, cm⁻¹*), saturated soil conductivity (*ksat1_f, ksat1_o,*
417 *ksat2_f, ksat2_o, ksat3, mm/day*).

418 6.2 Reference data and methodology

419 Soil proprieties are derived from The International Soil Reference and Information Centre (ISRIC) SoilGrids250m
420 global gridded soil information release 2017 (further referred as SoilGrids250m). For reference data details see
421 Appendix 1. Soil proprieties are computed for both forested and non-forested (also known in literature as 'others')
422 areas, expressed as fractions (main source is forest fraction based on CGLS-LC100, see Section 4.2), where non-
423 forested area is the complementary fraction of forest. Soil depth layers are derived first and used as input to the
424 soil hydraulic equations used to derive the properties, following a sequential workflow (see Figure 14 and Table
425 4). Equations used are from Toth et al. (2015).



427
428
429
430
431
432
Figure 14. Workflow to generate the soil related fields; solid arrows indicate a function transformation, dotted – upscaling; dashed boxes indicate the intermediate fields used for other field generation, dotted – the fields only used for the soil-related fields; ‘SoilGrids250m depths’ – fields at the SoilGrids250m native grid and resolution with six default depths, ‘final grid and resolution’ – fields at the dataset’s final grid and resolution, boxes with no explicit indication – fields at SoilGrids250m native grid and resolution only.

433
434
Table 4. Soil property fields, their description, and applied transformations; name in brackets in italics next to each field corresponds to the name in the data repository.

<i>Field type</i>	<i>Description</i>	<i>Data Source</i>	<i>Transformation (in order)</i>
Soil depth layers 1, 2, 3 for forest and non-forest (<i>soildepth1_f, soildepth1_o, soildepth2_f, soildepth2_o, soildepth3_f, soildepth3_o</i>)	Root depths assumed to divide the total soil depth between topsoil (surface [layer 1] and middle [layer 2]) and subsoil (bottom [layer 3])	SoilGrids250m (<i>absolute_depth_to_bedrock; root_depth_f; root_depth_o</i>)	Transforming at SoilGrids250m native grid and resolution as described in Appendix 3 ‘Soil Depth’ (in total 3 forest and 3 non-forest soil depth layer fields); Reprojecting and upscaling to final grid and resolution with unweighted mean; NoData filling DEEP (upsampling to 1, 3, 15 arcminute, 1, 3, 15, 60 degrees spatial resolution with unweighted mean; replacing NoData at final resolution with first available precomputed less coarser resolution, if not – with zero)
Saturated volumetric soil moisture content for soil depth layers 1, 2, 3, and for forest and non-forest (<i>thetas1_f, thetas1_o, thetas2_f, thetas2_o, thetas3</i>)	Saturated water content soil hydraulic property representing the maximum water content in the soil	SoilGrids250m (<i>clay_content, silt_content, bulk_density; soildepth1_f; soildepth1_o; soildepth2_f; soildepth2_o; soildepth3_f; soildepth3_o; fracforest</i>)	Transforming at SoilGrids250m native grid and resolution as described in Appendix 3 ‘Soil hydraulic parameters’ (in total 5 fields per soil hydraulic parameter, except <i>thetar</i> – only 3 as no forest/ non-forest separation);
Residual volumetric soil moisture content for soil depth layers 1, 2, 3 (<i>thetar1, thetar2, thetar3</i>)	Residual water content soil hydraulic property representing the minimum water content in the soil	SoilGrids250m (<i>clay_content, silt_content; soildepth1_f; soildepth1_o; soildepth2_f; soildepth2_o; soildepth3_f; soildepth3_o; fracforest</i>)	Limiting values and weighting by forest/ non-forest fraction (limits <i>thetas</i> < 1.0, <i>thetar</i> < <i>thetas</i> , <i>lambda</i> ≤ 0.42, <i>genua</i> ≤ 0.055, <i>ksat</i> > 0.0);
Pore size index for soil depth layers 1, 2, 3, and for forest and non-forest (<i>lambda1_f, lambda1_o, lambda2_f, lambda2_o, lambda3</i>)	Van Genuchten parameter λ (also referred as ‘n-1’ in literature) soil hydraulic property representing the pore size index of the soil	SoilGrids250m (<i>clay_content, silt_content, bulk_density, organic_carbon_content; soildepth1_f; soildepth1_o; soildepth2_f; soildepth2_o; soildepth3_f; soildepth3_o; fracforest</i>)	Upscaling to final grid and resolution with unweighted mean; NoData filling DEEP (upsampling to 1, 3, 15 arcminute spatial resolution with unweighted mean; replacing NoData at final resolution with first available precomputed less coarser resolution, if not – with global unweighted mean)
Van Genuchten equation parameter for soil depth layers 1, 2, 3, and for forest and non-forest (<i>genua1_f, genua1_o, genua2_f, genua2_o, genua3</i>)	Van Genuchten parameter α soil hydraulic property	SoilGrids250m (<i>clay_content, silt_content, bulk_density, organic_carbon_content; soildepth1_f; soildepth1_o; soildepth2_f; soildepth2_o; soildepth3_f; soildepth3_o; fracforest</i>)	
Saturated soil conductivity for soil depth layers 1, 2, 3,	Saturated hydraulic conductivity soil	SoilGrids250m (<i>clay_content, silt_content, soil pH,</i>	

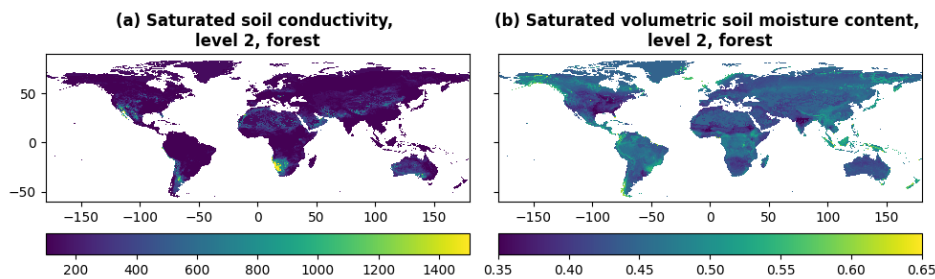
and for forest and non-forest (<i>ksat1_f</i> , <i>ksat1_o</i> , <i>ksat2_f</i> , <i>ksat2_o</i> , <i>ksat3</i>)	hydraulic property representing the ease with which water moves through pore spaces of the soil	cation_exchange_capacity); <i>soildepth1_f</i> ; <i>soildepth1_o</i> ; <i>soildepth2_f</i> ; <i>soildepth2_o</i> ; <i>soildepth3_f</i> ; <i>soildepth3_o</i> ; <i>fracforest</i>	
--	---	--	--

435
436
437
438
439
440
441
442
443
444
445
446
447
448
449
450
451
452
453
454
455

Two of the most common soil parameters of land surface and hydrological models, saturated hydraulic conductivity *ksat* and saturated water content, are shown in Figure 15.

Saturated hydraulic conductivity *ksat* (see Figure 15a) ranges from 2 to 7445 mm/day. The highest *ksat* values are concentrated in desertic areas such as the Sahara, Arabian Peninsula, Gobi, Patagonian, Sonoran-Mojave and Kalahari and Namib deserts. Low *ksat* between, 2 and 18 mm/day, are found in the Amazon river basin, the lower Mississippi river basin and South East Asia. *ksat* was visually compared against 8 global datasets developed with different input data and/ or PTFs (Zhang and Schaap, 2019; Gupta et al., 2021); a general agreement is noticeable in areas that show low variability across all datasets. Northern Russia, Canada, South East Asia and Sonoran-Mojave Desert are the areas with high variability among datasets, with values ranging from very low to very high *ksat*. Source of uncertainties in *ksat* values are primarily due to little availability of soil samples and measurements carried out in those areas. Moreover, the climatic context plays a relevant role in clay mineralogy composition, organic composition and soil pores structure (Hodnett and Tomasella, 2002), which influence how water flows through the soil. Therefore, the PTF developed using soil samples collected in temperate areas (such as Europe) are expected to have a different hydraulic behaviour compared to those collected in tropical climates (Gupta et al., 2021), as also seen in Figure 15a.

Saturated water content (see Figure 15b) ranges between 0.27 to 0.79, with 80% of values between 0.40 and 0.46. A comparison with other global datasets was not carried out, however uncertainties are expected to be of the same order of magnitude than those of *ksat* given the fact the saturated water content is calculated using bulk density and clay content data.

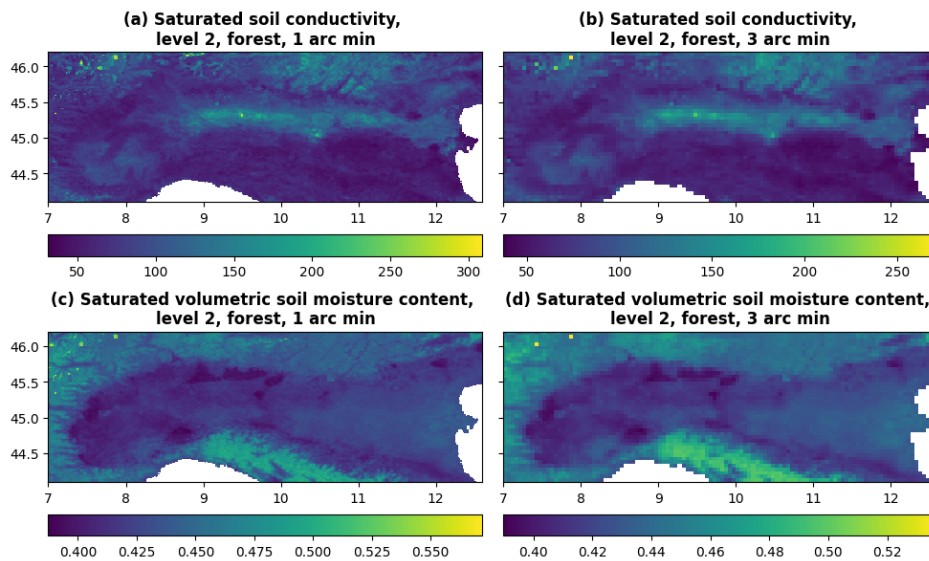


456
457
458
459

Figure 15. Saturated soil hydraulic conductivity for forested areas of soil depth layer 2 in mm per day (left column, plot a) and saturated volumetric soil moisture (i.e. water) content for forested areas of soil depth layer 2 (right column, plot b) at 3 arcminute (~5.6 km at the equator) resolution for global region.

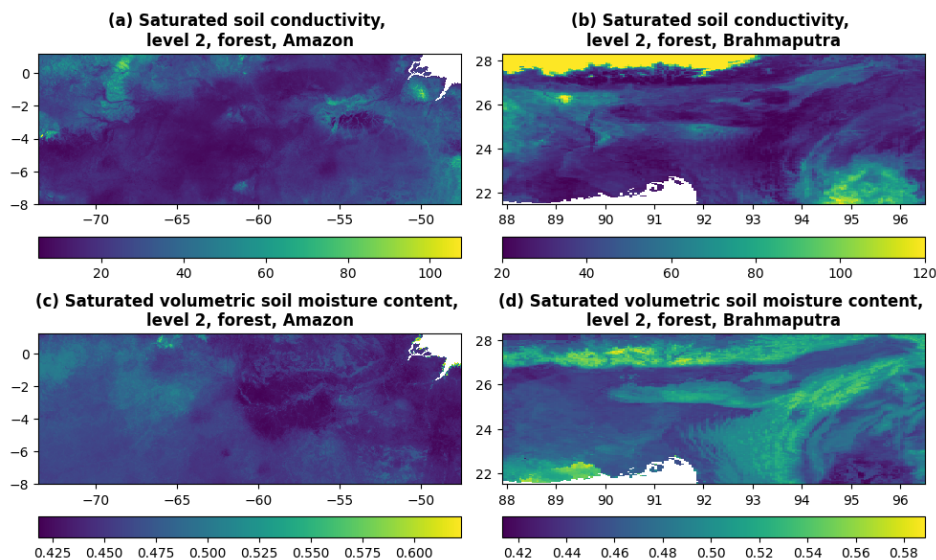
460 6.3 Regional examples

461 The majority of soil properties fields are easy to interpret. Saturated soil conductivity *ksat* and saturated volumetric
462 soil moisture content are presented for forested areas of soil depth layer 2 in Figure 16 for the Po River area in 1
463 and 3 arcminute resolution, and in Figure 17 for the Amazon River and the Brahmaputra River areas at 3 arcminute
464 resolution. The field of saturated soil conductivity for forest shows how easy it is for water to penetrate soil
465 depending on forest type. The field of saturated volumetric soil moisture content shows what is the maximum
466 amount of water that the soil can absorb depending on forest type. These fields have interesting features over
467 Brahmaputra River area.
468



469
470
471
472
473

Figure 16. Saturated soil hydraulic conductivity for forested areas of soil depth layer 2 in mm per day (upper row, plots a and b) and saturated volumetric soil moisture (i.e. water) content for forested areas of soil depth layer 2 (lower row, plots c and d) at 1 arcminute (~1.9 km at the equator, left column, plots a and c) and 3 arcminute (~5.6 km at the equator, right column, plots b and d) resolution for Po River area in Italy.



474
475
476
477
478

Figure 17. Saturated soil hydraulic conductivity for forested areas of soil depth layer 2 in mm per day (upper row, plots a and b) and saturated volumetric soil moisture (i.e. water) content for forested areas of soil depth layer 2 (lower row, plots c and d) at 3 arcminute (~5.6 km at the equator) resolution for Amazon River area (left column, plots a and c) and Brahmaputra River area (right column, plots b and d).

479 7 Lakes

480 7.1 General information

481 Lakes (and reservoirs) are important as they influence river discharge variability but also the atmosphere
482 regionally and globally. The area covered by lakes can be used for computing evaporation from open water,
483 freshwater storage, unregulated surface water extent, fresh water scarcity indexes, and biogenic green house gas
484 emission, as well as for reproducing different climate mitigation scenarios. The CEMS_SurfaceFields_2022
485 dataset only includes data on lake extent and not reservoirs (generally smaller). Lake mask describes the presence
486 of lakes, is consistent with fraction of inland water. The field's name in the data repository is *lakemask*,
487 dimensionless.

488 **7.2 Reference data and methodology**

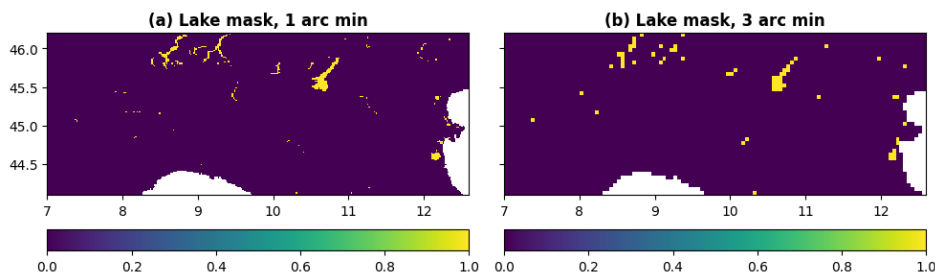
489 The lake mask field is derived from The Global Lakes and Wetlands Database (further referred as GLWD). For
 490 reference data details see Appendix 1, for workflow see Table 7.

491 **Table 5. Lake field, its description, data source and transformation; name in brackets in italics next to the lake field**
 492 **corresponds to the name in the data repository.**

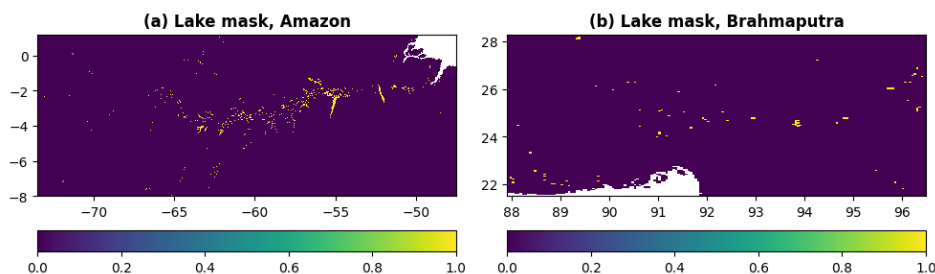
<i>Field type</i>	<i>Description</i>	<i>Data source</i>	<i>Transformation (in order)</i>
Lake mask (<i>lakemask</i>)	Area covered by lakes only (binary representation)	GLWD (GLWD-1, GLWD-2, lake type only); <i>fracwater</i>	Filtering non-lake spatial units; Shapefile gridding to final grid and resolution; If <i>fracwater</i> > 0 and GLWD is 'lake', then <i>lakemask</i> is 1, otherwise 0

494 **7.3 Regional examples**

495 The lake mask field is easy to interpret as it shows which grid cells from fraction of inland water field have lakes.
 496 The lake mask field is presented in Figure 18 for Po River area at 1 and 3 arcminute resolution, and in Figure 19
 497 for Amazon River and Brahmaputra River areas at 3 arcminute resolution. Figures show the abundance of lakes
 498 over Amazon River area and detailed lake shapes over Po River area described by the 1 arcminute resolution field.
 499



500 **Figure 18. Lake mask at 1 arcminute (~1.9 km at the equator, left column, plot a) and 3 arcminute (~5.6 km at the**
 501 **equator, right column, plot b) resolution for Po River area in Italy.**



503 **Figure 19. Lake mask at 3 arcminute (~5.6 km at the equator) resolution for Amazon River area (left column, plot a)**
 504 **and Brahmaputra River area (right column, plot b).**

506 **8 Water demand**

507 **8.1 General information**

508 Some environmental models explicitly represent a number of the human interventions impacting on the water
 509 cycle. One of the most common is water demand, which represents the withdrawal of water from natural water
 510 sources (e.g. rivers, reservoirs, groundwater) to satisfy the water demand for anthropogenic use. The segregation
 511 of the total water demand for anthropogenic use into four main sectors, namely domestic, energy, industrial, and
 512 livestock water withdrawal, enables a more accurate representation of the processes, and follows the Food and
 513 Agriculture Organisation of the United Nations (FAO) terminology (Kohli et al., 2012). Domestic water
 514 withdrawal represents indoor and outdoor household water use as well as other uses (e.g. industrial and urban
 515 agriculture) connected to the municipal system (e.g., water use by shops, schools, and public buildings). Electricity
 516 (energy) water withdrawal is the water use for the cooling of thermoelectric and nuclear power plants. Water
 517 withdrawal for industry is the water used for fabricating, processing, washing, cooling or transporting products,

518 also includes water within the final products and water used for sanitation within the manufacturing facility.
519 Livestock withdrawal is the demand for drinking and cleaning purposes of livestock.
520 Higher accuracy in environmental modelling is achieved by differentiating water demand sources and by
521 allocating different levels of priority to different usages. Within LISFLOOD, for instance, water demand for the
522 energy sector and flooded irrigation (rice crops) is supplied by surface water bodies only. Non-flooded irrigation,
523 domestic, industrial, livestock water demand can be supplied by both groundwater and surface water bodies.
524 Moreover, domestic water demand has the highest priority in case of water scarcity conditions.
525 It must be noted that the fields of water demand for agriculture are not included in this dataset because LISFLOOD
526 computes crops water demand internally by accounting for climatic conditions, information on land cover (see
527 Section 4.2), crops properties (see Section 5.2), and soil properties (see Section 6.2). Conversely, fields
528 representing the volume of water to satisfy the domestic, energy, industrial, and livestock demand must be
529 provided as input. Domestic, industrial, energy, and livestock water demand volumes have seasonal (e.g. due to
530 temperature differences) and inter-annual variations (e.g. due to population changes and different economic
531 conditions). In order to account for this variability, in LISFLOOD the four sectoral water demand fields provide
532 daily water demand data with monthly or annual variability from 01.01.1979 to 31.12.2019. The water demand
533 values are provided in mm/day, one field per month (the first day of each month is used as representative
534 timestamp for the entire month) for domestic and energy demand, one value per year (the monthly fields are
535 repeated twelve times per each year) for industrial and livestock demand.
536 Water availability, ecosystem long term ecological status, and anthropogenic needs must be accounted for to
537 evaluate the long term sustainability of water withdrawals. However, the spatial scales of water use data and
538 available water resources data often do not match due to different ways of data surveying and/or modelling
539 (McManamay et al., 2021; Zhang et al., 2023) and this creates a technical hurdle. Alternative use of the gridded
540 sectoral water demand information is e.g. for (i) the statistical analysis of long term spatiotemporal patterns and
541 trends of water demand; (ii) the evaluation of the long term sustainability and impacts of water withdrawals (e.g.
542 in connection to remote sensing-derived datasets of surface water extent or groundwater total storage); (iii) the
543 analysis of ecosystem–water–food–energy nexus (Karabulut et al., 2016); (iv) the evaluation of the impacts on
544 water resources of economical and price policies (Dolan et al., 2021); (v) the analysis of the responses in sectoral
545 water use during hydro climatic extremes (Belleza et al., 2023).
546 The CEMS_SurfaceFields_2022 dataset includes water demand for four main sectors (note that each sector
547 consists in total of 12 daily water demand fields per 41 (1979-2019) years, so 492 fields per sector) for (names in
548 brackets in italics correspond to the field names in the data repository): livestock (*liv*, mm/day), industry (*ind*,
549 mm/day), energy production, (*ene*, mm/day) and domestic use (*dom*, mm/day). The temporal extension of the
550 water demand fields presented in this manuscript includes the most recent information of water demand at the
551 time of the dataset’s preparation. Readers that are interested in using more recent water demand data are invited
552 to follow the protocol presented in Section 8.2 to further extend in time the provided fields.

553 8.2 Reference data and methodology

554 Global gridded water demand fields with monthly variability were generated for the four sectors using the main
555 data sources listed here and following the transformations summarised in Table 8 (for additional information and
556 extra details see GitHub repository ‘lisflood-utilities/src/lisfloodutilities/water-demand-historic at master · ec-
557 jrc/lisflood-utilities · GitHub’, last accessed: 21.01.2024): (i) AQUASTAT, (ii) United States Geological Survey
558 National Water Information System (further referred as USGS NWIS), (iii) Global Change Analysis Model
559 (further referred as GCAM), (iv) The Gridded Livestock of the World (GLW) version3 (further referred as
560 GLW3), (v) The Global Human Settlement Population Grid multitemporal version R2019A (further referred as
561 GHS-POP). For the full list of reference data and details see Appendix 1.
562 The water demand values are provided in mm/day, one field per month from 01.01.1979 to 31.12.2019 (the first
563 day of each month is used as the representative timestamp for the entire month). The methodology applied largely
564 follows Huang et al. (2018), with the key differences being the use of freely available datasets and the higher
565 resolution of the resulting fields. Spatial downscaling was achieved following the approach of Hejazi et al. (2014);
566 temporal downscaling was performed following the approaches of Wada et al. (2011), Voisin et al. (2013) and
567 Huang et al. (2018). It should be noted that country-scale estimates (from AQUASTAT) were integrated with
568 state-level water withdrawal estimates (from USGS NWIS). The protocol for the integration of local information
569 with global data sources was developed for further use in the future, to enable the integration of other regional or
570 national datasets as soon as they become available.

571
572 **Table 6. Water demand fields, their description, data source and applied transformations; cells with bold italics show**
573 **required intermediate fields; name in brackets in italics next to each field corresponds to the name in the data**
574 **repository.**

<i>Field type</i>	<i>Description</i>	<i>Data source</i>	<i>Transformations (in order)</i>
-------------------	--------------------	--------------------	-----------------------------------

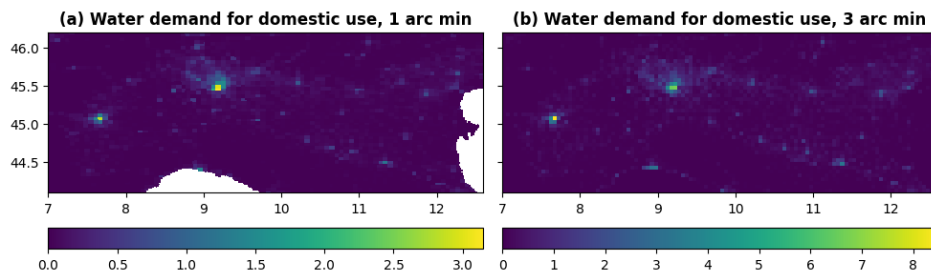
Population density (<i>pop</i>)	Number of people per grid cell	GHS-POP R2019A (1975, 1990, 2000, 2015)	Reprojecting and upscaling from native (9 arc sec) to the final grid and intermediate resolution of 0.01°x0.01° with sum (in total four fields); Transforming from population number to density per grid cell (i.e. dividing by grid cell area) and upscaling from intermediate to final resolution with mean (in total four fields); NoData filling (year) with linear interpolation till 2015, and with years 2000 and 2015 trend extrapolation 2016 onwards (pop_{year}^{grid} ; in total 41 fields)
		TM ‘country borders’, US CB ‘state borders’	Shapefile (country, US State) gridding to final grid and intermediate resolution of 0.01°x0.01°, then to final resolution; Transforming from population density per grid cell to population per country (i.e. multiplying by grid cell area and summing grid cells according to the country mask from step above); $pop_{year}^{country}$; in total one table)
Water demand for domestic use (<i>dom</i>)	Daily supply of water volume for indoor and outdoor household purposes and for all the uses that are connected to the municipal system (e.g., water used by shops, schools, and public buildings)	AQUASTAT (per country), USGS NWIS (per US State), <i>pop</i>	Unit conversion from native to km ³ /year; NoData filling (year): for countries – with linear interpolation and forward/ backward extrapolation based on $pop_{year}^{country}$, for US states – with linear interpolation and nearest neighbour extrapolation ($demand_{year}^{country}$, in total one table)
		<i>pop</i> , TM ‘country borders’, US CB ‘state borders’	Transforming water demand ($demand_{year}^{country}$) to water demand per capita per country/ US State per year (in total one table): $perCapitaDemand_{year}^{country} = \frac{demand_{year}^{country}}{pop_{year}^{country}}$; NoData filling (country) with nearest neighbour; Transforming from water demand per capita to water demand per grid cell (i.e. weighting by pop_{year}^{grid} , in total one field per year): $demand_{year}^{grid} = perCapitaDemand_{year}^{country} \cdot pop_{year}^{grid}$
		MSWX, Huang et al. (2018) [Table 3, Eq. (2)].	Temporal downscaling (month) to account for the withdrawal fluctuations between the warmest and coldest months based on Huang et al. (2018) Eq. (2) (in total 12 fields per year): $demand_{month,year}^{grid} = \frac{demand_{year}^{grid}}{month_{number}} \cdot \left(\frac{\bar{T}_{month,year}^{grid} - avg_{year} \bar{T}_{year}^{grid}}{max_{year} \bar{T}_{year}^{grid} - min_{year} \bar{T}_{year}^{grid}} \cdot R + 1 \right)$, where $avg_{year} \bar{T}_{year}^{grid}$, $max_{year} \bar{T}_{year}^{grid}$, $min_{year} \bar{T}_{year}^{grid}$ are the average, maximum, minimum monthly temperatures in a year; $\bar{T}_{month,year}^{grid}$ is the average temperature in a month of the year; R is the amplitude of the monthly fluctuations from Huang et al. (2018) [Table 3]; $month_{number}$ is number of months in a year, i.e. 12; Temporal downscaling (day; in total 12 fields per year): $demand_{day,month,year}^{grid} = \frac{demand_{month,year}^{grid}}{day_{number}}$, where day_{number} is number of days in a month of a certain year
Water demand for industrial use (<i>ind</i>)	Daily supply of water volume for fabricating, processing, washing and sanitation, cooling or transporting a product, incorporating water into a product	AQUASTAT (per country), USGS NWIS (per US State), GCAM (per region), Vassolo and Doll (2005), World Bank (MVA), <i>pop</i> , TM ‘country borders’	Unit conversion from native to km ³ /year; NoData filling (year; in total one table): <ul style="list-style-type: none"> regional data – downscaling (spatial) to country values (i.e. weighting by $pop_{year}^{country}$), then linear interpolation (between years) and nearest neighbour extrapolation in time, finally rescaling values according to Vassolo and Doll (2005); country data – with linear interpolation (between years) and forward/ backward extrapolation based on MVA or $pop_{year}^{country}$, value disaggregation from industrial water demand to manufacturing and thermoelectric water demands according to regional data results; for US States data – with linear interpolation (between years) and nearest neighbour extrapolation; mosaicking results from US States and country data, from regional data, if not – with zero
		<i>pop</i> , TM ‘country borders’, US CB ‘state borders’	Transforming from water demand per country/ US State to per grid cell (i.e. weighting by $pop_{year}^{grid}/pop_{year}^{country}$; in total one field per year): $demand_{year}^{grid} = \frac{demand_{year}^{country}}{pop_{year}^{country}} \cdot pop_{year}^{grid}$;

			Temporal downscaling (day; in total one field per year): $demand_{day,year}^{grid} = \frac{demand_{year}^{grid}}{day_{year}^{number}}$, where day_{year}^{number} is number of days in a year
Water demand for thermoelectric use (<i>ene</i>)	Daily supply of water volume for the cooling of thermoelectric and nuclear power plants	AQUASTAT (per country), USGS NWIS (per US State), GCAM (per region), Vassolo and Doll (2005), World Bank (MVA), <i>pop</i> , TM ‘country borders’	Same steps as for water demand for industrial use, but using the energy withdrawals as input data (in total one table)
		<i>pop</i> , TM ‘country borders’, US CB ‘state borders’	Same steps as for water demand for industrial use (in total one field per year)
		GCAM (per region), MSWX, Huang et al. (2018) [Eq. (3)-(10)].	Temporal downscaling (month) to account for the withdrawal fluctuations between the warmest and coldest months based on Huang et al. (2018) Eq. (3)-(10) (in total 12 fields per year)
Water demand for livestock use (<i>liv</i>)	Daily supply of water volume for domestic animal needs	AQUASTAT (per country), USGS NWIS (per US State), GCAM (per region), GLW3, TM ‘country borders’	Unit conversion from native to km ³ /year; NoData filling (year; in total one table): <ul style="list-style-type: none"> regional data – spatial downscaling from regional withdrawals to country values (i.e. weighting by total livestock mass estimates per country from GLW3, $livestock_{year}^{country}$): $demand_{year}^{country} = \frac{withdrawal_{year}^{region}}{livestock_{year}^{region}} \cdot livestock_{year}^{country}$, then value linear interpolation (between years) and nearest neighbour extrapolation, finally rescaled with country data (if available) for US States data – with linear interpolation (between years) and nearest neighbour extrapolation; mosaicking results from US States and regional data, if not – with zero
		GLW3, TM ‘country borders’, US CB ‘state borders’	Transforming from water demand per country/ US State to per grid cell (i.e. weighting by $\frac{livestockDensity_{year}^{grid}}{livestockDensity_{year}^{country}}$; in total one field per year): $demand_{year}^{grid} = \frac{demand_{year}^{country}}{livestockDensity_{year}^{country}} \cdot livestockDensity_{year}^{grid}$, Temporal downscaling (day; in total one field per year): $demand_{day,year}^{grid} = \frac{demand_{year}^{grid}}{day_{year}^{number}}$, where day_{year}^{number} is number of days in a year

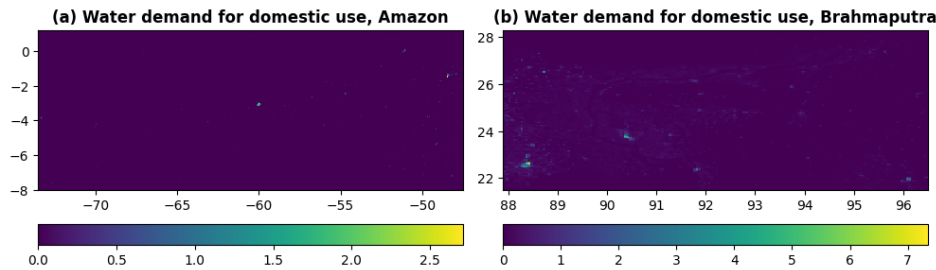
575 To the best of the authors’ knowledge, no other publicly accessible temporally varying global water demand field
576 set exists (only static datasets). A rigorous validation of the temporally varying water demand fields is not
577 straightforward at the global scale, as the only comprehensive global data source, FAO AQUASTAT, was used
578 to create the fields.

579 8.3 Regional examples

580 In general fields in water demand category are easy to interpret as they show how much water per day is needed
581 to satisfy certain type of human induced needs. In reality water demand fields are mainly covering urbanised areas
582 and are scattered around (i.e. not continuously looking field), with relatively small variations in field values from
583 month to month. Example for domestic water use is presented for August 2018 in Figure 20 for Po River area in
584 1 and 3 arcminute resolution, and in Figure 21 for Amazon River and Brahmaputra River areas at 3 arcminute
585 resolution.
586



587
588 **Figure 20. Water demand for domestic use in mm per day at 1 arcminute (~1.9 km at the equator, left column, plot a)**
589 **and 3 arcminute (~5.6 km at the equator, right column, plot b) resolution for Po River area in Italy.**



590
591 **Figure 21. Water demand for domestic use in mm per day at 3 arcminute (~5.6 km at the equator) resolution for**
592 **Amazon River area (left column, plot a) and Brahmaputra River area (right column, plot b).**

593 9 Data, access, licensing, documentation

594 The new CEMS_SurfaceFields_2022 is an open-source dataset of the Copernicus Emergency Management
595 Service describing key components of the Earth surface generally required in environmental and hydrological
596 modelling, including Earth system modelling and numerical weather prediction. The dataset includes static fields
597 (e.g. forest fraction), yearly cycle fields (e.g. 10-day average LAI, in total 36 fields), and yearly varying fields
598 (e.g. water demand). The surface fields are based on 25 different sources, including global and regional high
599 resolution (up to 100 m) gridded and vector datasets. They were processed into two set of fields (i) at 1 arcminute
600 resolution (~1.86 km at the equator) over Europe (72.25 N/ 22.75 N, 25.25 W/ 50.25 E; 4530x2970 grid cells),
601 and (ii) at 3 arcminute resolution (~5.57 km at the equator) over the Globe (90.00 N/ 90.00 S, 180.00 W/ 180.00
602 E; 7200x3600 grid cells), to provide an up-to-date surface state for six main field groups: (1) catchment
603 morphology and river network, (2) land use fields, (3) vegetation properties, (4) soil properties, (5) lakes, (6) water
604 demand.

605 The CEMS_SurfaceFields_2022 dataset consist in total of 140 gridded fields at EPSG:4326 – WGS84: World
606 Geodetic System projection in NetCDF format with information on Earth’s surface state (see Table 9 for the full
607 list of fields), which are grouped thematically in sub-folders. The 1 arcminute European fields have a total volume
608 of 9.3 GB and the 3 arcminute global fields have a total volume of 22.7 GB. The CEMS_SurfaceFields_2022
609 dataset is freely available for download from the Joint Research Centre (JRC) Data Catalogue
610 (<https://data.jrc.ec.europa.eu/>). The set of global surface fields at 3 arcminute resolution can be found here (JRC
611 Data Catalogue – LISFLOOD static and parameter maps for GloFAS – European Commission (europa.eu),
612 <https://data.jrc.ec.europa.eu/dataset/68050d73-9c06-499c-a441-dc5053cb0c86>) and the set of surface fields for
613 the European domain at 1 arcminute resolution can be found here (JRC Data Catalogue – LISFLOOD static and
614 parameter maps for Europe – European Commission (europa.eu), [https://data.jrc.ec.europa.eu/dataset/f572c443-
615 7466-4adf-87aa-c0847a169f23](https://data.jrc.ec.europa.eu/dataset/f572c443-7466-4adf-87aa-c0847a169f23)). The README.txt file that can be found there contains the basic description of
616 each surface fields including general information, data description, file overview, methodological information and
617 data access and sharing information. For detailed technical description of how the surface fields were generated
618 refer to the LISFLOOD User Guide, available online: [https://ec-jrc.github.io/lisflood-code/4
619 Static-Maps-introduction/](https://ec-jrc.github.io/lisflood-code/4%20Static-Maps-introduction/). The changelog.txt file – provides users with information on updates to the datasets. The
620 copyright.txt file – information about the data license (CC BY 4.0).

621
622 **Table 9. Full list of surface fields with short description and units included in CEMS_SurfaceFields_2022 dataset; name**
623 **in *italics* corresponds to the field’s file name in the data repository.**

<i>Field group</i>	<i>Description</i>	<i>Name</i>	<i>Units</i>
Main	model’s field (i.e. in technical for model operation/ running sense)	<i>mask</i>	dimensionless

Catchment morphology and river network	local drainage direction (i.e. flow direction from one cell to another)	<i>LDD</i>	dimensionless
	grid cell area	<i>pixarea</i>	m ²
	grid cell length	<i>pixlength</i>	m
	upstream drainage area	<i>upArea</i>	m ²
	standard deviation of elevation	<i>elvstd</i>	m
	gradient	<i>gradient</i>	m/m
	channel bottom width	<i>chanbw</i>	m
	channel length	<i>chanlength</i>	m
	channel gradient	<i>changrad</i>	m/m
	Manning's roughness coefficient for channels	<i>chanman</i>	s/m ^{1/3}
	channel mask (i.e. presence of river channel)	<i>chan</i>	dimensionless
	channel side slope (i.e. channel's horizontal distance divided by vertical distance)	<i>chans</i>	m/m
	bankfull channel depth	<i>chanbnkf</i>	m
channel floodplain (i.e. width of the area where the surplus of water is distributed when the water level in the channel exceed the channel depth)	<i>chanflpn</i>	m	
Land use fields	fraction of forest	<i>fracforest</i>	dimensionless
	fraction of sealed surface	<i>fracsealed</i>	dimensionless
	fraction of inland water	<i>fracwater</i>	dimensionless
	fraction of irrigated crops	<i>fracirrigated</i>	dimensionless
	fraction of rice	<i>fracrice</i>	dimensionless
	fraction of other cover types	<i>fracother</i>	dimensionless
Vegetation properties (for forest [f], irrigated crops [i], other land cover types [o])	crop coefficient	<i>cropcoef_f, cropcoef_i, cropcoef_o</i>	dimensionless
	crop group number	<i>cropgrp_n_f, cropgrp_n_i, cropgrp_n_o</i>	dimensionless
	Manning's surface roughness coefficient	<i>mannings_f, mannings_o,</i>	s/m ^{1/3}
	rice planting days (3 seasons)	<i>riceplantingday1, riceplantingday2, riceplantingday3</i>	calendar day number
	rice harvesting days (3 seasons)	<i>riceharvestday1, riceharvestday2, riceharvestday3</i>	calendar day number
	leaf area index	<i>laif, laii, laio</i>	m ² /m ²
Soil properties (for [1, 2, 3] layers; for forest [f], non-forest [o])	surface layer depth	<i>soildepth1_f, soildepth1_o</i>	mm
	middle layer depth	<i>soildepth2_f, soildepth2_o,</i>	mm
	subsoil depth	<i>soildepth3_f, soildepth3_o</i>	mm
	saturated volumetric soil moisture content	<i>thetas1_f, thetas1_o, thetas2_f, thetas2_o, thetas3</i>	m ³ /m ³
	residual volumetric soil moisture content	<i>thetar1, thetar2, thetar3</i>	m ³ /m ³
	pore size index	<i>lambda1_f, lambda1_o, lambda2_f, lambda2_o, lambda3</i>	dimensionless
	Van Genuchten equation parameter	<i>genua1_f, genua1_o, genua2_f, genua2_o, genua3</i>	cm ⁻¹
	saturated soil conductivity	<i>ksat1_f, ksat1_o, ksat2_f, ksat2_o, ksat3</i>	mm/day
Lakes	lake mask (i.e. presence of lakes)	<i>lakemask</i>	dimensionless
Water demand	livestock	<i>liv</i>	mm/day
	industry	<i>ind</i>	mm/day
	thermoelectric production	<i>ene</i>	mm/day
	domestic use	<i>dom</i>	mm/day

624
625
626
627
628
629
630

Whilst the CEMS_SurfaceFields_2022 dataset followed strict requirements of the LISFLOOD-OS model (e.g. format, treatment of missing values, number of soil layers, etc...) it definitely can be used outside the LISFLOOD context, using the full dataset or its parts, for applications such as modelling risk assessment. The workflow and methodology used to generate the dataset and published in this manuscript can be used as reference and be easily modified if further adaptation to the dataset is needed (e.g. using different set of equations to describe the soil properties, or sourcing new/ more relevant local datasets).

631 10 Conclusion

632 The Earth's surface has a strong impact on the surface energy and water balance that drives lower atmosphere
633 weather conditions and river discharge fluctuations. Depending on the surface type (e.g. land use, terrain or soil),

634 weather in the region can be colder/ warmer, more/ less humid, drier/ rainier, and/ or calmer/ windier than its
635 surroundings. Depending on the surface type also the terrestrial water cycle can differ, with water infiltrating
636 more/ less in the soil, leaving as evaporation in a larger/ smaller rate, and reaching rivers faster/ slower. Surface
637 information is provided by land use and ecosystem type (e.g., forest, rice paddy, bare ground, urban), river
638 geometry (e.g., channel width, channel length), soil properties (e.g., depth, porosity, hydraulic properties),
639 amongst others.

640 Information of underlying surface fields can be accounted for in Earth system and environmental models (e.g.
641 atmospheric, hydrological, etc.) to simulate the evolution in space and time of water, energy and carbon cycles. If
642 artificial influences and human intervention are included within the modelled processes (e.g. irrigation or water
643 management through reservoirs), the information required to describe the processes must also be integrated within
644 the modelling framework. Generally, this is achieved through a set of independent files used as input to the models.
645 Because of the temporal non-stationarity of some surface fields, typically associated with human intervention such
646 as land use and water use, but also due to climatic variation such as lake extent (new lakes forming or lakes
647 shrinking), input surface fields must be as representative as possible to the simulated period of interest. For
648 medium-range forecasting systems, this should be as close from present as possible, for example. When simulating
649 long periods, especially looking at past or future decades, caution must be given to results. Especially, if some
650 surface fields which have substantially changed during the simulation period do not explicitly incorporate time
651 and instead are based on the most recent period. Most recent period may not be representative to the full study
652 period and can introduce substantial biases that grow with time. Same is applicable if surface fields are used for
653 collecting statistical data in general, as stats based on stationary fields represent only the period used to generate
654 stationary field in question.

655 In addition, in recent years the horizontal resolution of global Earth system and environmental models has been
656 constantly increasing reaching the kilometre scale milestone. This has been supported by the technological
657 developments in the field of High Performance Computers and the wealth of high resolution datasets freely
658 available. This imposes another condition to the input surface fields – fields must be of rather high horizontal
659 resolution (i.e. ~2 and 6 km at the equator).

660 Thanks to the availability of a wide range of high resolution environmental data derived from the use of ground,
661 unconventional and satellite measurement sensors, new high resolution datasets describing the Earth's surface are
662 nowadays released regularly. Even though each dataset may have a very low absolute and root mean square errors
663 compared against available independent data, merging different datasets for modelling purposes (e.g. to model
664 hydrological surface parameters) might lead to questionable results and even model crash, due to possible
665 discontinuity or inconsistency in the combined datasets. In the specific case of hydrological modelling where river
666 flow is also represented, high horizontal resolution does not guarantee better modelling per se. Sources of
667 potentially large errors can be easily hidden in high resolution datasets. This is the case for instance of errors in
668 the Digital Elevation Models when they are used to obtain the rivers drainage network. Small errors in the
669 elevation of a grid cell can lead to a totally inaccurate representation of the location and the direction in which the
670 river is flowing in the model compared to reality. Mislocating a river or having a slightly inaccurate catchment
671 area can represent a trivial inaccuracy for most applications, but it can also lead to missed flood warning for
672 thousands of people within a flood awareness system. To benefit from different recent high resolution datasets
673 based on satellite and ground measurements, it is essential that a well-defined, thorough workflow is designed and
674 implemented so that the final products are consistent and compatible with each other, and can be used in
675 combination.

676 The work presented in this manuscript is focused not only on the final surface field set generation (i.e.
677 CEMS_SurfaceFields_2022), but also on deriving robust reproducible methodology that could be re-applied once
678 new versions of 25 or less input sources are released. Understanding of the methodology applied helps to interpret
679 values in the final surface fields and possibly even numerical model results that use these surface fields. The
680 collection of input sources and their preparation for actual use is a very important step as it includes going through
681 all technical documentation, comparison and verification of papers, and investigation of the actual data, as well
682 as data gridding, interpolation, and scaling. All input sources for CEMS_SurfaceFields_2022 are ranked according
683 to their quality and up-to-date in order to favour one value in ambiguous situations when several datasets provide
684 different information for the same location. Consistency check between all surface type fractions is carried out to
685 address that ambiguity during the merge of information of different origin (i.e. adjust fractions to sum to one in
686 each grid cell). Some fields, like forest fraction, were rather straightforward to create from available source, yet it
687 was noted that prior correction of the source was needed to delete erroneous forest grid cells from the Fox Basin
688 in Canada (the mismatch was only spotted during the investigation of the actual data, as it was absent from the
689 documentation). Other fields, like soil hydraulic properties, are created not only from the source information but
690 also from the forest fraction that had to be generated prior. The soil hydraulic property methodology also includes
691 several steps that have to be performed at the data native resolution (i.e. 250 m) using information from several
692 global fields simultaneously which becomes technically and computationally challenging. Surface fields with
693 clear multi-annual changes, like water demand maps, are created using temporal interpolation and extrapolation

694 from multiple data sources to create time series fields. A final and non-trivial task is to have all resulting fields on
695 the identical required grid without deterioration of the actual value precision, even after several file type
696 translations (e.g. local drainage direction field can be automatically checked and corrected if needed for required
697 boundaries only in PCRaster format, not NetCDF). Due to the number of data sources and surface fields required
698 to represent the main variables (i.e. 70) used in Earth system and environmental models, the overall effort to
699 generate the CEMS_SurfaceFields_2022 dataset (both human and computing resources) was substantial.
700 The CEMS_SurfaceFields_2022 dataset is a new data source open to all offering a kilometre-scale resolution of
701 high-quality data describing the Earth's surface, providing exceptional opportunity for the research and scientific
702 community to extend and multiply European and global applications in wide ranging fields of the water-energy-
703 food nexus. The CEMS_SurfaceFields_2022 surface fields use can be vast, here are only few of them. Standard
704 deviation of elevation and other orographic sub-grid parameters are critical for radiation parametrization,
705 especially for shadowing effect. Channel geometry fields are vital to describe overbank inundation and infer
706 inundated areas in wetland methane and soil carbon modelling. Land use fractions are needed for skin temperature
707 calculations, biogenic flux calculations, urban planning, and climate mitigation plan preparation. LAI use include
708 biomass allocation, which can be used for fire danger forecasting, and carbon stock monitoring. Rice planting/
709 harvesting days are important for yearly cycle of methane modelling. Soil properties are used for soil moisture
710 calculations. The area covered by lakes can be used for computing evaporation from open water, freshwater
711 storage, unregulated surface water extent, fresh water scarcity indexes, and biogenic green house gas emission, as
712 well as for reproducing different climate mitigation scenarios. All of the above state that
713 CEMS_SurfaceFields_2022 surface fields can be used for weather prediction, Earth system modelling,
714 hydrological and environmental modelling, or statistical analysis in general, with a spatial scale allowing for
715 global, regional and even national applications.

716
717 *Data availability.* The CEMS_SurfaceFields_2022 datasets are freely available for download from the JRC Data
718 Catalogue – global at ~5.6 km at the equator or 3 arcminute resolution:
719 <https://data.jrc.ec.europa.eu/dataset/68050d73-9c06-499c-a441-dc5053cb0c86>), over Europe at ~1.9 km at the
720 equator or 1 arcminute resolution: <https://data.jrc.ec.europa.eu/dataset/f572c443-7466-4adf-87aa-c0847a169f23>,
721 and are documented in this paper.

722
723 *Author contributions.* CP and PS shaped initial plan of the research; MC and FM executed initial plan; CM, SG
724 and JD reviewed initial results and provided guidance in further research. MC, FM and CP prepared a first draft
725 of the paper, which was adapted to its present state by contributions from CM, SG, JD, PS and HB.

726
727 *Competing interests.* The authors declare that they have no conflict of interest.

728
729 *Acknowledgements.* CEMS_SurfaceFields_2022 is a product and service of the Copernicus Emergency
730 Management Service. Financial support for MC, FM, CM and CP was provided by contract 941462-IPR-2021.
731 Authors thank two anonymous reviewers for their valuable comments and suggestions that helped to shape the
732 manuscript to its current state.

733
734 *Financial support.* This research has been supported by contract 941462-IPR-2021.

735 **References**

- 736 Alfieri, L., Lorini, V., Hirpa, F. A., Harrigan, S., Zsoter, E., Prudhomme, C., and Salamon, P.: A global streamflow
737 reanalysis for 1980–2018. *Journal of Hydrology X*, 6, 100049, ISSN 2589-9155,
738 <https://doi.org/10.1016/j.hydroa.2019.100049>, 2020. (Available online
739 <https://www.sciencedirect.com/science/article/pii/S2589915519300331>, last accessed: 21.01.2024).
- 740 Allen, R. G., Pereira, L. S., Raes, D., and Smith, M.: *FAO Irrigation and Drainage Paper No. 56: Crop*
741 *Evapotranspiration (guidelines for computing crop water requirements)*, 1998. (Available online:
742 https://www.researchgate.net/publication/284300773_FAO_Irrigation_and_drainage_paper_No_56,
743 last accessed: 21.01.2024).
- 744 Balsamo, G.: Interactive lakes in the Integrated Forecasting System. *ECMWF Newsletter No. 137 – Autumn 2013*,
745 pp. 30–34, <https://doi.org/10.21957/rffv1gir>, 2013. (Available online: <https://www.ecmwf.int/en/elibrary/80145-interactive-lakes-integrated-forecasting-system>, last accessed: 21.01.2024).
- 747 Bates, P. D. and De Roo, A. P. J.: A simple raster-based model for flood inundation simulation. *Journal of*
748 *hydrology*, vol. 236, 1-2, pp. 54–77, ISSN 0022-1694, [https://doi.org/10.1016/S0022-1694\(00\)00278-X](https://doi.org/10.1016/S0022-1694(00)00278-X), 2000.
749 (Available online: <https://www.sciencedirect.com/science/article/abs/pii/S002216940000278X>, last accessed:
750 21.01.2024).

751 Beck, H. E., van Dijk, A. I. J. M., Larraondo, P. R., McVicar, T. R., Pan, M., Dutra, E., and Miralles, D. G.:
752 MSWX: Global 3-Hourly 0.1° Bias-Corrected Meteorological Data Including Near-Real-Time Updates and
753 Forecast Ensembles. *Bulletin of the American Meteorological Society*, 103(3), pp. E710-E732,
754 <https://doi.org/10.1175/BAMS-D-21-0145.1>, 2022. (Available online:
755 <https://journals.ametsoc.org/view/journals/bams/103/3/BAMS-D-21-0145.1.xml>, last accessed: 21.01.2024).
756 Belleza, G. A. C., Bierkens, M. F. P., and van Vliet M. T. H.: Sectoral water use responses to droughts and
757 heatwaves: analyses from local to global scales for 1990–2019. *Environ. Res. Lett.*, 18 (10), 104008,
758 <https://doi.org/10.1088/1748-9326/acf82e>, 2023.
759 Best, M. J., Pryor, M., Clark, D. B., Rooney, G. G., Essery, R. L. H., Menard, C. B., Edwards, J. M., Hendry, M.
760 A., Porson, A., Gedney, N., Mercado, L. M., Sitch, S., Blyth, E., Boucher, O., Cox, P. M., Grimmond, C. S. B.,
761 and Harding, R. J.: The Joint UK Land Environment Simulator (JULES), model description – Part 1: Energy and
762 water fluxes. *Geosci. Model Dev.*, 4, 677–699, <https://doi.org/10.5194/gmd-4-677-2011>, 2011. (Available online:
763 www.geosci-model-dev.net/4/677/2011/, last accessed: 21.01.2024).
764 Bhardwaj, A.: Evaluation of Openly Accessible MERIT DEM for Vertical Accuracy in Different Topographic
765 Regions of India. 39th INCA International Congress, Dehradun (India), vol. 39, pp. 239–245, 2021. (Available
766 online:
767 https://www.researchgate.net/publication/356726804_Evaluation_of_openly_Accessible_MERIT_DEM_for_ve
768 [rtical_accuracy_in_different_topographic_regions_of_india](https://www.researchgate.net/publication/356726804_Evaluation_of_openly_Accessible_MERIT_DEM_for_vertical_accuracy_in_different_topographic_regions_of_india), last accessed: 21.01.2024).
769 Bonan, G., Levis, S., Sitch, S., Vertenstein, M., and Oleson, K.: A dynamic global vegetation model for use with
770 climate models: Concepts and description of simulated vegetation dynamics. *Global Change Biology*, 9, pp. 1543–
771 1566, <https://doi.org/10.1046/j.1365-2486.2003.00681.x>, 2003.
772 Brooks, R. H. and Corey, A. T.: Hydraulic properties of porous media. Hydrology paper No. 3, Colorado State
773 Univ., Fort Collins, 1964.
774 Buchhorn, M., Smets, B., Bertels, L., De Roo, B., Lesiv, M., Tsendbazar, N.-E., Herold, M., and Fritz, S.:
775 Copernicus Global Land Service: Land Cover 100m: collection 3: epoch 2015: Globe (V3.0.1) [Data set]. Zenodo,
776 <https://doi.org/10.5281/zenodo.3939038>, 2020.
777 Buchhorn, M., Smets, B., Bertels, L., De Roo, B., Lesiv, M., Tsendbazar, N.-E., Li, L., and Tarko, A.: Copernicus
778 Global Land Service: Land Cover 100m: version 3 Globe 2015-2019: Product User Manual (Dataset v3.0, doc
779 issue 3.4). Zenodo, <https://doi.org/10.5281/zenodo.4723921>, 2021.
780 Burek, P., Van Der Knijff, J., and De Roo, A.: LISFLOOD – Distributed Water Balance and Flood Simulation
781 Model – Revised User Manual. Luxembourg: Publications Office of the European Union, JRC78917, 2013.
782 (Available online: <https://publications.jrc.ec.europa.eu/repository/handle/JRC78917>, last accessed: 21.01.2024).
783 Burek, P., Bianchi, A., and Gentile, A.: JRC Technical Report: A Pan-European Data Set for hydrological
784 modelling. Luxembourg: Publications Office of the European Union, 2014.
785 Büttner, G. and Kosztra, B.: CLC2018 Technical Guidelines, Environment Agency, Austria, 2017. (Available
786 online: <https://land.copernicus.eu/en/technical-library/clc-2018-technical-guidelines/@@download/file>, last
787 accessed: 21.01.2024).
788 Calvin, K., Patel, P., Clarke, L., Asrar, G., Bond-Lamberty, B., Cui, R. Y., Di Vittorio, A., Dorheim, K., Edmonds,
789 J., Hartin, C., Hejazi, M., Horowitz, R., Iyer, G., Kyle, P., Kim, S., Link, R., McJeon, H., Smith, S. J., Snyder, A.,
790 Waldhoff, S., and Wise, M.: GCAM v5.1: representing the linkages between energy, water, land, climate, and
791 economic systems. *Geosci. Model Dev.*, 12, 677–698, <https://doi.org/10.5194/gmd-12-677-2019>, 2019.
792 Carver, G.: Ten years of OpenIFS at ECMWF. ECMWF Newsletter No. 170 – Winter 2021/22, pp. 6-7, 2022.
793 (Available online: <https://www.ecmwf.int/en/newsletter/170/news/ten-years-openifs-ecmwf>, last accessed:
794 21.01.2024).
795 Chai, L. T., Wong, C. J., James, D., Loh, H. Y., Liew, J. J. F., Wong, W. V. C., and Phua, M. H.: Vertical accuracy
796 comparison of multi-source Digital Elevation Model (DEM) with Airborne Light Detection and Ranging
797 (LiDAR). *IOP Conf. Ser.: Earth Environ. Sci.*, 1053, 012025, 2022. (Available online:
798 <https://iopscience.iop.org/article/10.1088/1755-1315/1053/1/012025/pdf>, last accessed: 21.01.2024).
799 Clark, D. B., Mercado, L. M., Sitch, S., Jones, C. D., Gedney, N., Best, M. J., Pryor, M., Rooney, G. G., Essery,
800 R. L. H., Blyth, E., Boucher, O., Harding, R. J., Huntingford, C., and Cox, P. M.: The Joint UK Land Environment
801 Simulator (JULES), model description – Part 2: Carbon fluxes and vegetation dynamics. *Geosci. Model Dev.*, 4,
802 701–722, <https://doi.org/10.5194/gmd-4-701-2011>, 2011. (Available online: [www.geosci-model-](http://www.geosci-model-dev.net/4/701/2011/)
803 [dev.net/4/701/2011/](http://www.geosci-model-dev.net/4/701/2011/), last accessed: 21.01.2024).
804 De Roo, A. P. J., Van Der Knijff, J., Schmuck, G., and Bates, P.: A simple floodplain inundation model to assist
805 in floodplain management. *New trends in water and environmental engineering for safety and life: Eco-compatible*
806 *solutions for aquatic environments*, 1–10, Balkema, Rotterdam, The Netherlands, 2000.
807 De Roo, A., Odijk, M., Schmuck, G., Koster, E., and Lucieer, A.: Assessing the effects of land use changes on
808 floods in the Meuse and Oder catchment. *Physics and Chemistry of the Earth, Part B: Hydrology, Oceans and*
809 *Atmosphere*, vol. 26, 7-8, 593–599, Pergamon, 2001.

810 Defourny, P., Lamarche, C., Bontemps, S., De Maet, T., Van Bogaert, E., Moreau, I., Brockmann, C., Boettcher,
811 M., Kirches, G., Wevers, J., and Santoro, M.: Land Cover CCI PRODUCT USER GUIDE VERSION 2.0 Tech.
812 Rep. ESA, 2017. (Available online: [https://maps.elie.ucl.ac.be/CCI/viewer/download/ESACCI-LC-Ph2-](https://maps.elie.ucl.ac.be/CCI/viewer/download/ESACCI-LC-Ph2-PUGv2_2.0.pdf)
813 [PUGv2_2.0.pdf](https://maps.elie.ucl.ac.be/CCI/viewer/download/ESACCI-LC-Ph2-PUGv2_2.0.pdf), last accessed: 21.01.2024).

814 Dolan, F., Lamontagne, J., Link, R., Hejazi, M., Reed, P., and Edmonds, J.: Evaluating the economic impact of
815 water scarcity in a changing world. *Nat Commun* 12, 1915, <https://doi.org/10.1038/s41467-021-22194-0>, 2021.

816 Eerola, K., Rontu, L., Kourzeneva, E., Kheyrollah Pour, H., and Duguay, C.: Impact of partly ice-free Lake
817 Ladoga on temperature and cloudiness in an anticyclonic winter situation – a case study using a limited area
818 model. *Tellus A*, 66, 23929, <https://doi.org/10.3402/tellusa.v66.23929>, 2014.

819 Florczyk, A. J., Corbane, C., Ehrlich, D., Freire, S., Kemper, T., Maffenini, L., Melchiorri, M., Pesaresi, M.,
820 Politis, P., Schiavina, M., Sabo, F., Zanchetta, L., European Commission, Joint Research Centre: GHSL Data
821 Package 2019 – Public release GHS P2019, EUR 29788 EN, Publications Office of the European Union,
822 Luxembourg, ISBN 978-92-76-13186-1, JRC 117104, <https://data.europa.eu/doi/10.2760/290498>, 2019.

823 Fredlund, D.G. and Xing, A.: Equations for the Soil-Water Characteristic Curve. *Canadian Geotechnical Journal*,
824 31, 521–532, <http://dx.doi.org/10.1139/t94-061>, 1994.

825 Freire, S., MacManus, K., Pesaresi, M., Doxsey-Whitfield, E., and Mills, J.: Development of new open and free
826 multi-temporal global population grids at 250 m resolution. *Geospatial Data in a Changing World*; Association of
827 Geographic Information Laboratories in Europe (AGILE), 2016.

828 Gardner, W. R.: Calculation of capillary conductivity from pressure plate outflow data. *Soil Science Society*
829 *Proceeding*, 20(3), pp. 317–320, <https://doi.org/10.2136/sssaj1956.03615995002000030006x>, 1956.

830 Google Earth Engine: Frequently Asked Questions (GEE: FAQ), 2023. (Available online:
831 <https://earthengine.google.com/faq/>, last accessed: 21.01.2024).

832 Gilbert, M., Nicolas, G., Cinardi, G., Van Boeckel, T. P., Vanwambeke, S. O., Wint, G. R. W., and Robinson, T.
833 P.: Global distribution data for cattle, buffaloes, horses, sheep, goats, pigs, chickens and ducks in 2010. *Sci Data*
834 5, 180227, <https://doi.org/10.1038/sdata.2018.227>, 2018.

835 Gorelick, N., Hancher, M., Dixon, M., Ilyushchenko, S., Thau, D., and Moore, R.: Google Earth Engine:
836 Planetary-scale geospatial analysis for everyone. *Remote Sensing of Environment*, vol. 202, pp. 18–27,
837 <https://doi.org/10.1016/j.rse.2017.06.031>, 2017. (Available online:
838 <https://www.sciencedirect.com/science/article/pii/S0034425717302900>, last accessed: 21.01.2024).

839 Grimaldi, S., Salamon, P., Disperati, J., Zsoter, E., Russo, C., Ramos, A., Carton De Wiart, C., Barnard, C.,
840 Hansford, E., Gomes, G., and Prudhomme, C.: River discharge and related historical data from the Global Flood
841 Awareness System. v4.0. Copernicus Climate Change Service (C3S) Climate Data Store (CDS) [Data set],
842 <https://doi.org/10.24381/cds.a4fdd6b9>, 2022. (Available online:
843 <https://cds.climate.copernicus.eu/cdsapp#!/dataset/10.24381/cds.a4fdd6b9?tab=form>, last accessed: 21.01.2024).

844 Gupta, S., Lehmann, P., Bonetti, S., Papritz, A., and Or, D.: Global prediction of soil saturated hydraulic
845 conductivity using random forest in a Covariate-based GeoTransfer Function (CoGTF) framework. *Journal of*
846 *Advances in Modeling Earth Systems*, 13(4), e2020MS002242, <https://doi.org/10.1029/2020MS002242>, 2021.

847 Harrigan, S., Zsoter, E., Cloke, H., Salamon, P., and Prudhomme, C.: Daily ensemble river discharge reforecasts
848 and real-time forecasts from the operational Global Flood Awareness System. *Hydrol. Earth Syst. Sci.*, 27, 1–19,
849 <https://doi.org/10.5194/hess-27-1-2023>, 2023. (Available online: <https://hess.copernicus.org/articles/27/1/2023/>,
850 last accessed: 21.01.2024).

851 Hejazi, M., Edmonds, J., Clarke, L., Kyle, P., Davies, E., Chaturvedi, V., Wise, M., Patel, P., Eom, J., Calvin, K.,
852 Moss, R., and Kim, S.: Long-term global water projections using six socioeconomic scenarios in an integrated
853 assessment modeling framework. *Technol. Forecast. Social Change*, 81, pp. 205–226,
854 <https://doi.org/10.1016/j.techfore.2013.05.006>, 2014. (Available online:
855 <https://www.sciencedirect.com/science/article/abs/pii/S0040162513001169>, last accessed: 21.01.2024).

856 Hengl, T., de Jesus, J. M., MacMillan, R. A., Batjes, N. H., Heuvelink, G. B. M., Ribeiro, E., Samuel-Rosa, A.,
857 Kempen, B., Leenaars, J. G. B., Walsh, M. G., and Ruiperez Gonzalez, M.: SoilGrids1km – Global Soil
858 Information Based on Automated Mapping. *PLOS ONE* 9(8): e105992,
859 <https://doi.org/10.1371/journal.pone.0105992>, 2014.

860 Hengl, T., de Jesus, J. M., Heuvelink, G. B. M., Ruiperez Gonzalez, M., Kilibarda, M., Blagotić, A., Shangquan,
861 W., Wright, M. N., Geng, X., Bauer-Marschallinger, B., Guevara, M. A., Vargas, R., MacMillan, R. A., Batjes,
862 N. H., Leenaars, J. G. B., Ribeiro, E., Wheeler, I., Mantel, S., and Kempen, B.: SoilGrids250m: Global gridded
863 soil information based on machine learning. *PLOS ONE* 12(2): 1–40,
864 <https://doi.org/10.1371/journal.pone.0169748>, 2017.

865 Hirpa, F. A., Salamon, P., Beck, H. E., Lorini, V., Alfieri, L., Zsoter, E., and Dadson, S. J.: Calibration of the
866 Global Flood Awareness System (GloFAS) using daily streamflow data. *Journal of Hydrology*, vol. 566, 595–
867 606, <https://doi.org/10.1016/j.jhydrol.2018.09.052>, 2018.

868 Hodnett, M. G. and Tomasella, J.: Marked differences between van Genuchten soil water-retention parameters for
869 temperate and tropical soils: a new water-retention pedo-transfer functions developed for tropical soils. *Geoderma*,
870 vol. 108 (3-4), pp. 155–180, ISSN 0016-7061, [https://doi.org/10.1016/S0016-7061\(02\)00105-2](https://doi.org/10.1016/S0016-7061(02)00105-2), 2002.

871 Huang, Z., Hejazi, M., Li, X., Tang, Q., Vernon, C., Leng, G., Liu, Y., Döll, P., Eisner, S., Gerten, D., Hanasaki,
872 N., and Wada, Y.: Reconstruction of global gridded monthly sectoral water withdrawals for 1971–2010 and
873 analysis of their spatiotemporal patterns. *Hydrol. Earth Syst. Sci.*, 22, 2117–2133, <https://doi.org/10.5194/hess-22-2117-2018>, 2018.

875 Huijnen, V., Le Sager, P., Köhler, M. O., Carver, G., Rémy, S., Flemming, J., Chabrillat, S., Errera, Q., and van
876 Noije, T.: OpenIFS/AC: atmospheric chemistry and aerosol in OpenIFS 43r3. *Geosci. Model Dev.*, 15, 6221–
877 6241, <https://doi.org/10.5194/gmd-15-6221-2022>, 2022.

878 International Food Policy Research Institute (IFPRI): Global Spatially-Disaggregated Crop Production Statistics
879 Data for 2010 Version 2.0 [Data set]. Harvard Dataverse, <https://doi.org/10.7910/DVN/PRFF8V>, 2019.
880 (Available online: <https://dataverse.harvard.edu/dataset.xhtml?persistentId=doi:10.7910/DVN/PRFF8V>, last
881 accessed: 21.01.2024).

882 Intara, Y. I., Nusantara, A. D., Supanjani, Caniago, Z., and Ekawita, R.: Oil Palm Roots Architecture in Response
883 to Soil Humidity. *International Journal of Oil Palm* Vol. 1, Nr. 2, ISSN: 2614-2376, 2018. (Available online:
884 <https://ijop.id/index.php/ijop/article/view/11/10>, last accessed: 21.01.2024).

885 Karabulut, A., Egoh, B. N., Lanzanova, D., Grizzetti, B., Bidoglio, G., Pagliero, L., Bouraoui, F., Aloe, A.,
886 Reynaud, A., Maes, J., Vandecasteele, I., and Mubareka, S.: Mapping water provisioning services to support the
887 ecosystem–water–food–energy nexus in the Danube river basin. *Ecosystem Services*, 17, 278–292,
888 <https://doi.org/10.1016/j.ecoser.2015.08.002>, 2016. (Available online:
889 <https://www.sciencedirect.com/science/article/pii/S221204161530019X>, last accessed: 21.01.2024).

890 Karssenber, D., Schmitz, O., Salamon, P., de Jong, K., and Bierkens, M. F. P.: A software framework for
891 construction of process-based stochastic spatio-temporal models and data assimilation. *Environmental Modelling
892 & Software*, 25(4), pp. 489–502, <https://doi.org/10.1016/j.envsoft.2009.10.004>, 2010.

893 Kimpson, T., Choulga, M., Chantry, M., Balsamo, G., Boussetta, S., Dueben, P., and Palmer, T.: Deep learning
894 for quality control of surface physiographic fields using satellite Earth observations. *Hydrol. Earth Syst. Sci.*,
895 27(24), 4661–4685, <https://doi.org/10.5194/hess-27-4661-2023>, 2023.

896 Köhler, M. O., Hill, A. A., Huijnen, V., and Le Sager, P.: Enhancing OpenIFS by adding atmospheric composition
897 capabilities. *ECMWF Newsletter No. 175 – Spring 2023*, pp. 27-31, <http://doi.org/10.21957/np36mk1s9d>, 2023.
898 (Available online: [https://www.ecmwf.int/en/newsletter/175/earth-system-science/enhancing-openifs-adding-
899 atmospheric-composition](https://www.ecmwf.int/en/newsletter/175/earth-system-science/enhancing-openifs-adding-atmospheric-composition), last accessed: 21.01.2024).

900 Kohli, A., Frenken, K., and Spottorno, C.: Disambiguation of water statistics. *FAO AQUASTAT Report*,
901 *AQUASTAT Programme*, FAO, pp. 1-6, 2012. (Available online: <https://www.fao.org/3/bc816e/bc816e.pdf>, last
902 accessed: 21.01.2024).

903 Laborte, A. G., Gutierrez, M. A., Balanza, J. G., Saito, K., Zwart, S. J., Boschetti, M., Murty, M. V. R., Villano,
904 L., Aunario, J. K., Reinke, R., Koo, J., Hijmans, R. J., and Nelson, A.: RiceAtlas, a spatial database of global rice
905 calendars and production [Data set]. Harvard Dataverse, V3, <https://doi.org/10.7910/DVN/JE6R2R>, 2017a.

906 Laborte, A. G., Gutierrez, M. A., Balanza, J. G., Saito, K., Zwart, S. J., Boschetti, M., Murty, M. V. R., Villano,
907 L., Aunario, J. K., Reinke, R., Koo, J., Hijmans, R. J., and Nelson, A.: RiceAtlas, a spatial database of global rice
908 calendars and production. *Sci Data.*, 4:170074, PMID: 28556827, PMCID: PMC5448352,
909 <https://doi.org/10.1038/sdata.2017.74>, 2017b. (Available online:
910 <https://www.ncbi.nlm.nih.gov/pmc/articles/PMC5448352/>, last accessed: 21.01.2024).

911 Lawrence, D. M., Fisher, R. A., Koven, C. D., Oleson, K. W., Swenson, S. C., Bonan, G., Collier, N., Ghimire,
912 B., van Kampenhout, L., Kennedy, D., Kluzek, E., Lawrence, P. J., Li, F., Li, H., Lombardozzi, D., Riley, W. J.,
913 Sacks, W. J., Shi, M., Vertenstein, M., Wieder, W. R., Xu, C., Ali, A. A., Badger, A. M., Bisht, G., van den
914 Broeke, M., Brunke, M. A., Burns, S. P., Buzan, J., Clark, M., Craig, A., Dahlin, K., Drewniak, B., Fisher, J. B.,
915 Flanner, M., Fox, A. M., Gentine, P., Hoffman, F., Keppel-Aleks, G., Knox, R., Kumar, S., Lenaerts, J., Leung,
916 L. R., Lipscomb, W. H., Lu, Y., Pandey, A., Pelletier, J. D., Perket, J., Randerson, J. T., Ricciuto, D. M.,
917 Sanderson, B. M., Slater, A., Subin, Z. M., Tang, J., Thomas, R. Q., Val Martin, M., and Zeng, X.: The Community
918 Land Model version 5: Description of new features, benchmarking, and impact of forcing uncertainty. *Journal of
919 Advances in Modeling Earth Systems*, 11(12), pp. 4245-4287, <https://doi.org/10.1029/2018MS001583>, 2019.

920 Lehner, B. and Döll, P.: Development and validation of a global database of lakes, reservoirs and wetlands. *Journal
921 of Hydrology*, vol. 296(1-4), pp. 1–22, <https://doi.org/10.1016/j.jhydrol.2004.03.028>, 2004. (Available online:
922 <http://dx.doi.org/10.1016/j.jhydrol.2004.03.028>, last accessed: 21.01.2024).

923 Lv, S., Zeng, Y., Wen, J., Zhao, H., and Su, Z.: Estimation of Penetration Depth from Soil Effective Temperature
924 in Microwave Radiometry. *Remote Sens.*, vol. 10(4), 519. <https://doi.org/10.3390/rs10040519>, 2018.

925 Marthews, T. R., Dadson, S. J., Clark, D. B., Blyth, E. M., Hayman, G. D., Yamazaki, D., Becher, O. R. E.,
926 Martinez-de la Torre, A., Prigent, C., and Jimenez, C.: Inundation prediction in tropical wetlands from JULES-
927 CaMa-Flood global land surface simulations. *Hydrology and Earth System Sciences*, vol. 26(12), 3151–3175,

928 <https://doi.org/10.5194/hess-26-3151-2022>, 2022. (Available online:
929 <https://hess.copernicus.org/articles/26/3151/2022/>, last accessed: 21.01.2024).

930 Martínez-Sánchez, E.: Scientific Quality Evaluation of LAI/FAPAR/FCOVER Collection 1km Version 1 and
931 Version 2 Issue 11.00, 2020. (Available online:
932 [https://land.copernicus.eu/global/sites/cgls.vito.be/files/products/CGLOPS1_SQE2019_LAI1km-](https://land.copernicus.eu/global/sites/cgls.vito.be/files/products/CGLOPS1_SQE2019_LAI1km-V1%26V2_11.00.pdf)
933 [V1%26V2_11.00.pdf](https://land.copernicus.eu/global/sites/cgls.vito.be/files/products/CGLOPS1_SQE2019_LAI1km-V1%26V2_11.00.pdf), last accessed: 21.01.2024).

934 McManamay, R. A., KC, B., Allen-Dumas, M. R., Kao, S. C., Brelsford, C. M., Ruddell, B. L., Sanyal, J., Stewart,
935 R. N., and Bhaduri, B. L.: Reanalysis of water withdrawal for irrigation, electric power, and public supply sectors
936 in the conterminous United States, 1950–2016. *Water Resources Research*, 57(2), e2020WR027751,
937 <https://doi.org/10.1029/2020WR027751>, 2021.

938 Moiret-Guigand, A.: Copernicus Land monitoring services – CLC2018 / CLCC1218 VALIDATION REPORT,
939 Issue 1.3, 2021 (Available online: [https://land.copernicus.eu/en/technical-library/clc-2018-and-clc-change-2012-](https://land.copernicus.eu/en/technical-library/clc-2018-and-clc-change-2012-2018-validation-report/@@download/file)
940 [2018-validation-report/@@download/file](https://land.copernicus.eu/en/technical-library/clc-2018-and-clc-change-2012-2018-validation-report/@@download/file), last accessed: 21.01.2024).

941 Notaro, M., Holman, K., Zarrin, A., Fluck, E., Vavrus, S., and Bennington, V.: Influence of the Laurentian Great
942 Lakes on Regional Climate. *J. Climate*, 26(3), pp. 789–804, <https://doi.org/10.1175/JCLI-D-12-00140.1>, 2013.

943 O’Callaghan, J. F. and Mark, D. M.: The Extraction of Drainage Networks from Digital Elevation Data. *Computer*
944 *Vision, Graphics, and Image Processing*, 28(3), pp. 323–344, [https://doi.org/10.1016/S0734-189X\(84\)80011-0](https://doi.org/10.1016/S0734-189X(84)80011-0),
945 1984.

946 Pesaresi, M. and Politis, P.: GHS-BUILT-S R2022A - GHS built-up surface grid, derived from Sentinel2
947 composite and Landsat, multitemporal (1975-2030) [Data set]. European Commission, Joint Research Centre
948 (JRC), <https://doi.org/10.2905/D07D81B4-7680-4D28-B896-583745C27085>, 2022. (Available online:
949 <http://data.europa.eu/89h/d07d81b4-7680-4d28-b896-583745c27085>, last accessed: 21.01.2024).

950 Rosbjerg, D. and Madsen, H.: Concepts of hydrologic modeling. In *Encyclopedia of Hydrological Sciences* (eds
951 M.G. Anderson and J.J. McDonnell), 10, 1–9, <https://doi.org/10.1002/0470848944.hsa009>, 2006.

952 Samuelsson, P., Kourzeneva, E., and Mironov, D.: The impact of lakes on the European climate as simulated by
953 a regional climate model. *Boreal Environ. Res.*, 15(2), pp. 113–129, <http://hdl.handle.net/10138/233079>, 2010.
954 (Available online: [https://helda.helsinki.fi/server/api/core/bitstreams/feb9f8de-e831-4e9e-9ee6-](https://helda.helsinki.fi/server/api/core/bitstreams/feb9f8de-e831-4e9e-9ee6-07ac7df898eb/content)
955 [07ac7df898eb/content](https://helda.helsinki.fi/server/api/core/bitstreams/feb9f8de-e831-4e9e-9ee6-07ac7df898eb/content), last accessed: 21.01.2024).

956 Schiavina, M., Freire, S., and MacManus, K.: GHS-POP R2019A - GHS population grid multitemporal (1975,
957 1990, 2000, 2015). European Commission, Joint Research Centre (JRC) [Data set],
958 <https://doi.org/10.2905/0C6B9751-A71F-4062-830B-43C9F432370F>, 2019. (Available online:
959 <https://data.jrc.ec.europa.eu/dataset/0c6b9751-a71f-4062-830b-43c9f432370f>, last accessed: 21.01.2024).

960 Schiavina, M., Melchiorri, M., Pesaresi, M., Politis, P., Freire, S., Maffenini, L., Florio, P., Ehrlich, D., Goch, K.,
961 Tommasi, P., Kemper, T., European Commission, Joint Research Centre: GHSL Data Package 2022 – Public
962 release GHS P2022, Publication Office of the European Union, JRC 129516, ISBN 978-92-76-53071-8,
963 <https://doi.org/10.2760/19817>, 2022.

964 Smets, B.: Product User Manual of LAI/FAPAR/FCOVER Collection 1km Version 2 Issue 1.33, 2019. (Available
965 online: [https://land.copernicus.eu/global/sites/cgls.vito.be/files/products/CGLOPS1_PUM_LAI1km-](https://land.copernicus.eu/global/sites/cgls.vito.be/files/products/CGLOPS1_PUM_LAI1km-V2_11.33.pdf)
966 [V2_11.33.pdf](https://land.copernicus.eu/global/sites/cgls.vito.be/files/products/CGLOPS1_PUM_LAI1km-V2_11.33.pdf), last accessed: 21.01.2024).

967 Smith, P. J., Pappenberger, F., Wetterhall, F., Del Pozo, J. T., Krzeminski, B., Salamon, P., Muraro, D., Kalas,
968 M., and Baugh, C.: On the operational implementation of the European Flood Awareness System (EFAS). *Flood*
969 *forecasting: A Global Perspective*, Academic Press, pp. 313–348, [https://doi.org/10.1016/B978-0-12-801884-](https://doi.org/10.1016/B978-0-12-801884-2.00011-6)
970 [2.00011-6](https://doi.org/10.1016/B978-0-12-801884-2.00011-6), 2016.

971 Sparrow, S., Bowery, A., Carver, G. D., Köhler, M. O., Ollinaho, P., Pappenberger, F., Wallom, D., and
972 Weisheimer, A.: OpenIFS@home version 1: a citizen science project for ensemble weather and climate
973 forecasting. *Geosci. Model Dev.*, 14(6), 3473–3486, <https://doi.org/10.5194/gmd-14-3473-2021>, 2021.

974 Supit, I., Hoojer, A. A., and Van Diepen, C. A.: System description of the Wofost 6.0 crop simulation model
975 implemented in CGMS. Volume 1: Theory and Algorithms, 1994. (Available online:
976 [https://www.researchgate.net/publication/282287246_System_description_of_the_Wofost_60_crop_simulation_](https://www.researchgate.net/publication/282287246_System_description_of_the_Wofost_60_crop_simulation_model_implemented_in_CGMS_Volume_1_Theory_and_Algorithms)
977 [model_implemented_in_CGMS_Volume_1_Theory_and_Algorithms](https://www.researchgate.net/publication/282287246_System_description_of_the_Wofost_60_crop_simulation_model_implemented_in_CGMS_Volume_1_Theory_and_Algorithms), last accessed: 21.01.2024).

978 Te Chow, V.: *Open-channel Hydraulics*. Civil engineering series (publisher McGraw-Hill Book Company Inc.),
979 ISBN 07-010776-9, 1959. (Available online: [https://heidarpour.iut.ac.ir/sites/heidarpour.iut.ac.ir/files/u32/open-](https://heidarpour.iut.ac.ir/sites/heidarpour.iut.ac.ir/files/u32/open-chow.pdf)
980 [chow.pdf](https://heidarpour.iut.ac.ir/sites/heidarpour.iut.ac.ir/files/u32/open-chow.pdf), last accessed: 21.01.2024).

981 Tóth, B., Weynants, M., Nemes, A., Makó, A., Bilas, G., and Tóth, G.: New generation of hydraulic pedotransfer
982 functions for Europe. *Eur J Soil Sci*, 66(1), pp. 226-238, <https://doi.org/10.1111/ejss.12192>, 2015.

983 Van Der Knijff, J. and De Roo, A.: LISFLOOD – Distributed Water Balance and Flood Simulation Model,
984 Revised User Manual. EUR 22166 EN/2, Office for Official Publications of the European Communities,
985 Luxembourg, 109 pp, 2008.

986 Van Der Knijff, J. M., Younis, J., and De Roo, A. P. J.: LISFLOOD: A GIS-based distributed model for river
987 basin scale water balance and flood simulation. *Int. J. Geogr. Inf. Sci.*, 24(2), 189–212, 2010.

- 988 van Genuchten, M. T.: A closed-form equation for predicting the hydraulic conductivity of unsaturated soils. *Soil*
989 *Sci. Soc. Am. J.*, 44, 892–898, 1980.
- 990 Vanham, D., Alfieri, L., Flörke, M., Grimaldi, S., Lorini, V., De Roo, A., and Feyen, L.: The number of people
991 exposed to water stress in relation to how much water is reserved for the environment: a global modelling study.
992 *The Lancet Planetary Health*, vol. 5(11), pp. e766–e774, [https://doi.org/10.1016/S2542-5196\(21\)00234-5](https://doi.org/10.1016/S2542-5196(21)00234-5), 2021.
993 (Available online: <https://www.sciencedirect.com/science/article/pii/S2542519621002345>, last accessed:
994 21.01.2024).
- 995 Vassolo, S. and Döll, P.: Global-scale gridded estimates of thermoelectric power and manufacturing water use.
996 *Water Resour. Res.* 41(4), <https://doi.org/10.1029/2004WR003360>, 2005.
- 997 Vavrus, S., Notaro, M., and Zarrin, A.: The role of ice cover in heavy lake-effect snowstorms over the Great Lakes
998 Basin as simulated by RegCM4. *Mon. Weather Rev.*, 141, 148–165, 2013.
- 999 Voisin, N., Liu, L., Hejazi, M., Tesfa, T., Li, H., Huang, M., Liu, Y., and Leung, L. R.: One-way coupling of an
1000 integrated assessment model and a water resources model: evaluation and implications of future changes over the
1001 US Midwest. *Hydrol. Earth Syst. Sci.*, 17(11), 4555–4575, <https://doi.org/10.5194/hess-17-4555-2013>, 2013.
- 1002 Wada, Y., van Beek, L. P. H., Viviroli, D., Dürr, H. H., Weingartner, R., and Bierkens, M. F. P.: Global monthly
1003 water stress: 2. Water demand and severity of water stress. *Water Resour. Res.*, 47(7), W07518,
1004 <https://doi.org/10.1029/2010WR009792>, 2011.
- 1005 Yamazaki, D., Oki, T., and Kanae, S.: Deriving a global river network map and its sub-grid topographic
1006 characteristics from a fine-resolution flow direction map. *Hydrol. Earth Syst. Sci.*, 13(11), 2241–2251,
1007 <https://doi.org/10.5194/hess-13-2241-2009>, 2009.
- 1008 Yamazaki, D., Kanae, S., Kim, H., and Oki, T.: A physically based description of floodplain inundation dynamics
1009 in a global river routing model. *Water Resour. Res.*, 47(4), W04501, <https://doi.org/10.1029/2010WR009726>,
1010 2011.
- 1011 Yamazaki, D., Ikeshima, D., Tawatari, R., Yamaguchi, T., O’Loughlin, F., Neal, J. C., Sampson, C. C., Kanae, S.,
1012 and Bates, P. D.: A high-accuracy map of global terrain elevations. *Geophys. Res. Lett.*, 44(11), pp. 5844–5853,
1013 <https://doi.org/10.1002/2017GL072874>, 2017.
- 1014 Yamazaki, D., Ikeshima, D., Sosa, J., Bates, P. D., Allen, G. H., and Pavelsky, T. M.: MERIT Hydro: A high-
1015 resolution global hydrography map based on latest topography datasets. *Water Resources Research*, vol. 55(6),
1016 pp. 5053–5073, <https://doi.org/10.1029/2019WR024873>, 2019.
- 1017 Yu, Q., You, L., Wood-Sichra, U., Ru, Y., Joglekar, A. K. B., Fritz, S., Xiong, W., Lu, M., Wu, W., and Yang,
1018 P.: A cultivated planet in 2010 – Part 2: The global gridded agricultural-production maps. *Earth Syst. Sci. Data*,
1019 12(4), 3545–3572, <https://doi.org/10.5194/essd-12-3545-2020>, 2020.
- 1020 Zhang, Y. and Schaap, M. G.: Estimation of saturated hydraulic conductivity with pedotransfer functions: A
1021 review. *Journal of Hydrology*, vol. 575, pp. 1011–1030, ISSN 0022-1694,
1022 <https://doi.org/10.1016/j.jhydrol.2019.05.058>, 2019.
- 1023 Zhang, J., Liu, D., Guo, S., Xiong, L., Liu, P., Chen, J., and Yin, J.: High resolution annual irrigation water use
1024 maps in China based-on input variables selection and convolutional neural networks. *Journal of Cleaner*
1025 *Production*, 405, 136974, <https://doi.org/10.1016/j.jclepro.2023.136974>, 2023. (Available online:
1026 <https://www.sciencedirect.com/science/article/pii/S0959652623011320>, last accessed: 21.01.2024).

1027 **Appendix**

1028 **Appendix 1**

1029 All data sources used to produce dataset’s surface fields, mentioned in Sections 3 to 9, are described here. All data
1030 considered were open source, freely available, updated as recently as possible, with recognised reference on their
1031 quality.

1032 **1.1 Catchment morphology and river network**

1033 **The MERIT DEM: Multi-Error-Removed Improved-Terrain Digital Elevation Model v.1.0.3** [15 October,
1034 2018] (further referred as MERIT DEM) is a high accuracy global DEM at 3 arc second resolution (~90 m at the
1035 equator) covering land area from 90 N to 60 S, selected for its ability to clearly represent landscapes such as river
1036 networks and hill-valley structures even in flat areas where height errors could be larger than topography
1037 variability (Yamazaki et al., 2017; Bhardwaj, 2021; Chai et al., 2022). It is derived from seven different open-
1038 source datasets, delivered as 57 GeoTiff files 30° by 30° region each, at ~90 m resolution (in total 90.0 GB),
1039 representative of the year 2018. More detail on method, data content and access can be found in Yamazaki et al.
1040 (2017) and MERIT DEM web-page http://hydro.iis.u-tokyo.ac.jp/~yamada/MERIT_DEM.
1041 The MERIT DEM was used to compute standard deviation of elevation, gradient and channel geometry fields.

1042 **The Catchment-based Macro-scale Floodplain (CaMa-Flood) Global River Hydrodynamics Model v4.0**
1043 **maps** (further referred as CaMa-Flood) are used for the basic maps describing all physical properties of the river
1044 network. It is derived from MERIT Hydro (MERIT Hydro is a global hydrography dataset, created by using
1045 elevation (i.e. MERIT DEM) and several inland water maps; more detail can be found in Yamazaki et al. (2019)
1046 and MERIT Hydro web-page http://hydro.iis.u-tokyo.ac.jp/~yamada/MERIT_Hydro) for high resolution river
1047 routing applications using the FLOW algorithm (Yamazaki et al., 2009; Yamazaki et al., 2011). The maps include
1048 information on channel length, river topography parameters, floodplain elevation profile, channel width and
1049 channel depth. The maps exist at 15, 6, 5, 3 and 1 arcminute resolutions covering land area from 90 N to 60 S,
1050 representative of the year 2017, and for each resolution, they are available as one single file with all variables in
1051 NetCDF format (for 1 arcminute 737.0 MB). More detail on method, data content and access can be found in
1052 Yamazaki et al. (2011) and CaMa-Flood web-page <http://hydro.iis.u-tokyo.ac.jp/~yamada/cama-flood/index.html>. Note that whilst the CaMaFlood maps were originally generated for the specific use of the
1053 CaMa-Flood model, they can also serve as basic to derive alternative maps for other environmental models, as
1054 done here.
1055 The CaMa-Flood maps were used to create the local drainage direction (LDD), upstream drainage area, channel
1056 geometry and land masks fields.
1057

1058 1.2 Land use fields

1059 **The Copernicus Global Land Service (CGLS) Land Cover (LC) 100m map** (further referred as CGLS-LC100)
1060 is a global land cover map of the year 2015 (Buchhorn et al., 2020). It is derived from the PROBA-V 100 m
1061 satellite image collection, a database of high quality land cover training sites and ancillary datasets, reaching an
1062 accuracy of 80 % at Level1 (Buchhorn et al., 2021). It contains 23 classes for discrete classification and 10 classes
1063 for continuous cover fractions; and it is delivered as 15 files in GeoTiff format (in total 39.3 GB) at 100 m
1064 resolution covering land area from 90 N to 60 S and representative of the year 2015. More detail on method, data
1065 content and access can be found in Buchhorn et al. (2021) and Copernicus web-site
1066 <https://land.copernicus.eu/global/products/lc>.

1067 The CGLS-LC100 was used to generate crop parameters and Manning's surface roughness coefficient for forest
1068 and other land cover types, to generate forest, inland water, and sealed surface fraction fields, following a basic
1069 quality check on large water bodies (i.e. correcting Fox Basin and Caspian Sea).

1070 **The Coordination of Information on the Environment (CORINE) Land Cover (CLC) inventory for 2018**
1071 (further referred as CLC2018) is a set of maps describing the land cover/ land use status of 2018 covering
1072 39 countries in Europe with a total area of over 5.8 Mkm². The dataset is derived from satellite imagery (mainly
1073 Sentinel-2, based on a constellation of two satellites orbiting Earth at altitude of 786 km 180° apart revisiting
1074 equator every 5 days, and for gap filling Landsat-8, making a constellation together with Landsat-9 satellite
1075 orbiting Earth at altitude of 705 km each revisiting equator every 16 days) and in-situ data and contains 44 classes,
1076 delivered as one GeoTiff raster file (125.0 MB) at 100m resolution covering land area over Europe, representative
1077 of the time period 2017-2018. The overall accuracy for CLC2018 is 92 % for the blind analysis (i.e. validation
1078 team had no knowledge of the CLC2018 thematic classes) but there are regional variations: the Black Sea
1079 geographical region has the lowest accuracy of 84 %; country-wise overall accuracy vary from 86 % for Portugal
1080 to 99 % for Iceland, lowest accuracy being linked to the landscape complexity (Moiret-Guigand, 2021). More
1081 detail on method, data content and access can be found in Büttner and Kosztra (2017) and Moiret-Guigand (2021),
1082 and Copernicus web-site <https://land.copernicus.eu/pan-european/corine-land-cover/clc2018>.

1083 The CLC2018 was used to generate the irrigated crop fraction and rice fraction fields.

1084 **The Spatial Production Allocation Model (SPAM) – Global Spatially-Disaggregated Crop Production**
1085 **Statistics Data for 2010 v2.0** (further referred as SPAM2010) is a global dataset generated in 2020, which
1086 redistributes crop production information from country and sub-national provinces level to a finer grid cell level
1087 (IFPRI, 2019). It is derived from numerous data sources, including crop production statistics, cropland data,
1088 biophysical crop “suitability” assessments, spatial distribution of specific crops or crop systems, and population
1089 density. SPAM2010 contains estimates of crop distributions within disaggregated units (based on a cross-entropy
1090 approach) for 42 crops and two production systems (irrigated and rainfed), and is delivered as 84 files in shapefile
1091 format at 10 km (5 arcminute) resolution covering land area from 90 N to 60 S and representative of the year 2010
1092 (in total 2.2 GB). Based on crop expert judgement from international (i.e. International Rice Research Institute,
1093 International Maize and Wheat Improvement Center) and national organisations (i.e. The Chinese Academy of
1094 Agricultural Sciences) SPAM2010 over Europe and America is more accurate than over Africa and South East
1095 Asia, with best performance in allocating rice; grid-by-grid comparison of crop areas with independent Cropland
1096 Data Layer (produced by using satellite images and vast amount of ground truth) over continental United States
1097 shows coefficient of determination (R^2) 0.7-0.9 and root mean square error (RMSE) 231-307 ha indicating a
1098 relatively high reliability, with highest R^2 and lowest RMSE values are for maize and soybean (Yu et al., 2020).

1099 More detail on method, data content and access can be found in Yu et al. (2020) and MapSPAM web-site
1100 <https://mapspam.info>.
1101 SPAM2010 was used to compute the irrigated crop and rice fractions, crop parameters and Manning's surface
1102 roughness coefficient for irrigated crop fields.

1103 1.3 Vegetation properties

1104 **The Food and Agriculture Organisation (FAO) of the United Nations Irrigation and Drainage Paper No.**
1105 **56** (further referred as FAO56) is a publication covering geographically referenced statistics for crop development
1106 stages, crop coefficients, crop height, rooting depth, and soil water depletion fraction for common crops found
1107 across the world; it also covers procedures for information aggregation, e.g. on the grid. It is delivered as an article
1108 with a set of tables and equations and can be considered as the most complete source of information on crop
1109 properties. More detail on method and data content can be found in Allen et al. (1998) and FAO online crop
1110 information web-page <http://www.fao.org/land-water/databases-and-software/crop-information/tobacco/en/>.

1111 FAO56 was used to compute the crop coefficients for forest, irrigated crops and other land cover types (online
1112 crop information was specifically used for tobacco); and for intermediate computations such as depletion fraction
1113 for different crop and surface types (table), crop height and root depth fields.

1114 **Intara et al. (2018)** is a publication covering oil palm roots architecture.

1115 Intara et al. (2018) was used for oil palm root depth information in addition to FAO56.

1116 **Burek et al. (2014)** is a publication covering summarised information for crop coefficients, rooting depth, crop
1117 group number and Manning's surface roughness coefficient for different surface types.

1118 Burek et al. (2014) was used for built-up, bare/ sparse vegetation, snow & ice, permanent inland water, ocean &
1119 seas, herbaceous wetland, moss & lichen surface types crop coefficients, rooting depth, crop group number and
1120 Manning's surface roughness coefficient information in addition to FAO56 and other sources.

1121 **The Wofost 6.0 crop simulation model description** (further referred as SUPIT) is a publication on developing,
1122 validating, and testing new or already existing agrometeorological models (Supit et al., 1994). It contains crop
1123 group information for several crops as examples, and relation of a crop group from water depletion fraction. The
1124 publication is delivered as a book with a set of tables and equations. Information on crop group is still considered
1125 up-to-date. More detail on method and data content can be found in Supit et al. (1994).

1126 SUPIT was used to compute the crop group fields for forest, irrigated crops and other land cover types.

1127 **The Open-Channel Hydraulics manual** (further referred as CHOW) is a publication on open-channel
1128 hydraulics, including basic principles and different types of flows, i.e. uniform, gradually varied, rapidly varied,
1129 and unsteady (Te Chow, 1959). It contains information on roughness coefficient over different surfaces. The
1130 publication is delivered as a book with a set of tables and equations. More detail on method and data content can
1131 be found in Te Chow (1959).

1132 CHOW was used to compute the Manning's surface roughness coefficient fields for forest, irrigated crops and
1133 other land cover types.

1134 **The Copernicus Global Land Service (CGLS) Leaf Area Index (LAI) 1km Version 2 collection** (further
1135 referred as CGLS-LAI) is a set of global maps without missing data describing vegetation dynamics – the annual
1136 evolution of LAI at 10-day intervals over the period of 1999-2020. The dataset is derived from
1137 SPOT/VEGETATION and PROBA-V data. The dataset's root mean square deviations over 20 GBOV sites over
1138 the period 2014-2018 is 0.92, compared to 1.19 for MODIS C6 LAI product (Martinez-Sanchez, 2020). The
1139 dataset is delivered as one multi-band file per year in NetCDF (netCDF4 CF-1.6) format (14.7 GB per year) at 1
1140 km resolution covering land area from 90 N to 60 S and representative of the 10-year period of 2010-2019. More
1141 detail on method, data content and access can be found in Smets (2019) and Martinez-Sanchez (2020), and
1142 Copernicus web-site <https://land.copernicus.eu/global/products/lai>.

1143 CGLS-LAI was used to compute the LAI fields for forest, irrigated crops and other land cover types.

1144 **The RiceAtlas v3** (further referred as RiceAtlas) is a spatial database of global rice calendars and production. It
1145 contains information on start, peak and end dates of sowing, transporting and harvesting rice, derived from global
1146 and regional databases, national publications, online reports, and expert knowledge. It is delivered as 7 files in
1147 shapefile format (in total 195.8 MB) for administrative units (in total 2725 spatial units) at 1 km resolution for the
1148 national production totals to match the years 2010-2012 (Laborte et al., 2017a). RiceAtlas is ~10 times more
1149 spatially detailed, and has ~7 times more special units comparing with other global datasets (Laborte et al., 2017b).
1150 More detail on method, data content and access can be found in Laborte et al. (2017a) and Laborte et al. (2017b).

1151 RiceAtlas was used to compute rice planting and rice harvesting days for three different seasons.

1152 1.4 Soil properties

1153 **The International Soil Reference and Information Centre (ISRIC) SoilGrids250m global gridded soil**
1154 **information release 2017** (further referred as SoilGrids250m) is an output of special predictions produced by the

1155 SoilGrids system, as a set of global soil property and class maps at 250 m resolution. It is derived from soil profile
1156 data (from ~150,000 sites globally) with the use of machine learning, and contains information on soil
1157 characteristics at six standard depths, including soil textures (clay, silt, sand), depth to bedrock, bulk density,
1158 organic carbon, pH and cation exchange capacity. It is delivered as 43 files in GeoTiff format (in total 111.8 GB)
1159 at 250 meters resolution covering land area with no permanent ice and representative for the year 2010 (according
1160 to land cover) (Hengl et al., 2017). SoilGrids250m pH comparison with SSURGO data over California (depth 0-
1161 200 cm) and Soil and Landscape Grid of Australia data over Tasmania (depth 0-5 cm) show high correlation, 0.79
1162 and 0.71 respectively (Hengl et al., 2017). Despite its limited accuracy (i.e. between 30 and 70 %, according to
1163 the SoilGrids web-site) due to the scarcity of soil profile observations (especially in Central Asia, Arctic regions
1164 coastal area and desert), low resolution of covariates data and algorithms, it was selected as the most recent source
1165 of information. More detail on method, data content and access can be found in Hengl et al. (2017) and
1166 SoilGrids250m web-site <https://www.isric.org/explore/soilgrids/faq-soilgrids-2017>.
1167 SoilGrids250m was used to compute the soil depth and soil hydraulic properties for forest and non-forest.

1168 1.5 Lakes

1169 **The Global Lakes and Wetlands Database** (further referred as GLWD) is a global database of water bodies. It
1170 is derived from a combination of global and regional lake data sets, registers and inventories (i.e. point information
1171 with descriptive attributes), and digital maps (i.e. polygons, rasterised global land cover and land use maps). The
1172 database consists of two global files in shapefile format at spatial resolutions of up to 1:1 million – GLWD-1 with
1173 3067 largest lake and 654 largest reservoir polygons (6.4 MB), and GLWD-2 with ~250000 smaller lake and
1174 reservoir polygons (32.0 MB); and of one global file in ADF raster format at 30 arc sec resolution – GLWD-3
1175 combines GLWD-1, GLWD-2 and additional information (8.9 MB). Validation against documented data shows
1176 that GLWD represents good wetland maximum extent, and describes comprehensively lakes with surface area
1177 greater or equal 1 km² (Lehner and Döll, 2004). More detail on method, data content and access can be found in
1178 Lehner and Döll (2004) and GLWD web-site [https://www.worldwildlife.org/pages/global-lakes-and-wetlands-](https://www.worldwildlife.org/pages/global-lakes-and-wetlands-database)
1179 [database](https://www.worldwildlife.org/pages/global-lakes-and-wetlands-database).
1180 GLWD (i.e. only GLWD-1 and GLWD-2) was used to compute the discrete lake mask field.

1181 1.6 Water demand

1182 **AQUASTAT** is the FAO's global information system on water resources and agricultural water management.
1183 AQUASTAT collects information on water use via the network of AQUASTAT National Correspondents who
1184 are required to fill the annual questionnaire and collaborate with AQUASTAT team in the data validation process.
1185 Five types of manual checks are followed by automatic implementation of almost 200 validation rules. The dataset
1186 includes data for 180 countries worldwide, yearly data from 1979 to 2019 were used to produce the maps presented
1187 by this manuscript. Float, lumped values for each country for the variables "Gross Domestic Product (GDP)",
1188 "Industry, value added to GDP", "Agricultural water withdrawal", "Industrial water withdrawal", "Municipal
1189 water withdrawal", "Total water withdrawal", and "Irrigation water withdrawal" were obtained in CSV format (2
1190 files, in total 2.0 MB) from the AQUASTAT data acquisition dashboard
1191 (https://tableau.apps.fao.org/views/ReviewDashboard-v1/country_dashboard). More detail on method, data
1192 content and access can be found in AQUASTAT web-site
1193 <https://www.fao.org/aquastat/en/overview/methodology/>.

1194 AQUASTAT variables were used accordingly to compute water demand fields for domestic, industrial, energy,
1195 livestock use.

1196 **United States Geological Survey National Water Information System** (further referred as USGS NWIS) is a
1197 national database on water use data for the United States (US) with annual statistics provided every 5 years since
1198 1950. The water use data are best estimates produced by the USGS in cooperation with local, state, and federal
1199 agencies as well as academic and private organisations. The water use data are lumped values (float numbers) for
1200 each state, delivered in plain text format (52 files, in total 56.0 MB). Following variables were used: "Domestic
1201 total self-supplied withdrawals, fresh, in Mgal/d", "Public Supply total self-supplied withdrawals, fresh, in
1202 Mgal/d", "Industrial total self-supplied withdrawals, fresh, in Mgal/d", "Total Thermoelectric Power total self-
1203 supplied withdrawals, fresh, in Mgal/d", "Total Thermoelectric Power power generated, in gigawatt-hours", and
1204 "Livestock total self-supplied withdrawals, fresh, in Mgal/d". More detail on method, data content and access can
1205 be found in USGS NWIS web-site <https://waterdata.usgs.gov/nv/nwis/wu>. For this study, data from 1985 to 2015
1206 were used.

1207 USGS NWIS variables were used accordingly to refine the global water demand fields for the domestic, industrial,
1208 energy, livestock use sectors for the US.

1209 **Global Change Analysis Model** (further referred as GCAM) is an integrated, multi-sector model developed by
1210 the Joint Global Change Research Institute (JGCRI) to explore the overall behaviour of human and physical

1211 systems dynamics and interactions. GCAM includes five main systems. One of these systems, the water module,
1212 provides information about water withdrawals for energy, agriculture, and municipal uses as lumped values of
1213 235 hydrologic basins; a detailed explanation can be found in Calvin et al. (2019). Estimates of industrial,
1214 thermoelectric water withdrawals (energy sector) and electricity consumption were computed by running the
1215 GCAM model, the output used are two files in CSV format (in total 4.0 MB). Data from the following sectors was
1216 used: "biomass", "electricity", "nuclearFuelGenII", "nuclearFuelGenIII", "regional coal", "regional natural gas",
1217 "regional oil", "SheepGoat", "Beef", "Dairy", "Pork", and "Poultry". More detail on method, data content and
1218 access can be found in the documentation of the open source package [https://github.com/JGCRI/gcam-](https://github.com/JGCRI/gcam-core/tree/gcam-v6.0)
1219 [core/tree/gcam-v6.0](https://github.com/JGCRI/gcam-core/tree/gcam-v6.0).

1220 GCAM variables were used accordingly to estimate water withdrawals for industrial, energy, livestock use.

1221 **Global-scale gridded estimates of thermoelectric power and manufacturing water use** (further referred as
1222 Vassolo and Doll, 2005) is a global-scale gridded estimate of water withdrawal for cooling of thermal power
1223 stations and for manufacturing. Estimates of values for the year 1995 are provided with a spatial resolution of 0.5°
1224 by 0.5°. Thermoelectric power water use is based on the geographical location of 63590 thermal power stations.
1225 Manufacturing water use is computed by estimating country-specific water withdrawal values, and spatial
1226 downscaling using city night-time lights. Dataset verification of Vassolo and Doll (2005) showed satisfactory
1227 representation of thermoelectric power water use but high uncertainty in the representation of manufacturing water
1228 use. The data are delivered as one shapefile (2.5 MB). More details on method, data content and validation, and
1229 data access can be found in Vassolo and Doll (2005).

1230 Vassolo and Doll (2005) dataset was used for the computation of energy demand fields.

1231 **The Gridded Livestock of the World (GLW) version3** (further referred as GLW3) is a spatial gridded dataset
1232 of the global distribution of eight livestock species for 2010. It is delivered as 8 GeoTiff files at 0.083333° (~10
1233 km at the equator) resolution (in total 208.0 MB). The species abundance was converted to total livestock mass.
1234 More detail on method, data content and access can be found in Gilbert et al. (2018).

1235 GLW3 was used to spatially disaggregate the water demand for livestock use.

1236 **World Bank manufacturing value added and gross domestic product** (further referred as World Bank) data
1237 provide "Manufacturing, value added (constant 2015 US\$)" values (further referred as MVA) and "Gross
1238 Domestic Product GDP (constant 2015 US\$)" values. The data provided as a table, downloaded in CSV format
1239 (6 files, in total 6.0 MB) from <https://data.worldbank.org>.

1240 World Bank dataset was used to temporally downscale the values of water demand fields for the industrial and
1241 energy sectors.

1242 **The Global Human Settlement Population Grid multitemporal version R2019A** (further referred as GHS-
1243 POP) is a spatial raster dataset that depicts the distribution of population, expressed as the number of people per
1244 grid cell (Freire et al., 2016; Florczyk et al., 2019; Schiavina et al., 2019). GHS-POP residential population
1245 estimates for target years provided by CIESIN GPWv4.10 were disaggregated from census or administrative units
1246 to grid cells, informed by the distribution and density of built-up as mapped in the Global Human Settlement
1247 Layer. The dataset has a spatial resolution of 9 arc sec (~300 m at the equator) resolution and is delivered as
1248 individual files in GeoTiff format for 1975, 1990, 2000 and 2015 (4 files, in total 6.5 GB; available online:
1249 https://ghsl.jrc.ec.europa.eu/ghs_pop2019.php, last accessed: 21.01.2024).

1250 GHS-POP was used to spatially disaggregate the country, state, basin-level information of domestic, industrial,
1251 energy water withdrawal.

1252 **Thematic Mapping Country Borders** shapefile (further referred as TM 'country borders') was derived from
1253 Thematic Mapping™, which is a tool enabling web browsers to create thematic maps and associated world
1254 datasets. For this work, the TM World Borders Dataset was downloaded as one shapefile (10.0 MB). **The United**
1255 **States Census Bureau** Cartographic Boundary Files – Shapefile (further referred as US CB) provides the State
1256 boundaries for the USA. For this work, the 2018 version was retrieved as one shapefile (3.2 MB; available online:
1257 <https://www.census.gov/geographies/mapping-files/time-series/geo/carto-boundary-file.html>, last accessed:
1258 21.01.2024). More detail on method, data content and access can be found in
1259 <http://thematicmapping.org/downloads/>.

1260 TM 'country borders' and US CB were used to spatially disaggregate the information of water withdrawal for
1261 domestic, industrial, energy use.

1262 **Multi-Source Weather** (further referred as MSWX) is a high-resolution (3-hourly, 0.1°), bias-corrected
1263 meteorological product with global coverage from 1979 to 7 months into the future. The data for 42 years
1264 (~316700 files in NetCDF format, in total 128.0 GB) were retrieved via www.gloh2o.org/mswx/. For more
1265 detailed information, see Beck et al. (2022).

1266 MSWX 2-meter daily and monthly maximum and minimum air temperature were used to account for the climate-
1267 induced intra- and inter- annual fluctuations of domestic, livestock, and energetic water demand.

1268 **Huang et al. (2018)** is a publication presenting 0.5° resolution global monthly gridded sectoral water withdrawal
1269 dataset for the period 1971–2010.

1270 Huang at al. (2018) Table 3 (calibrated R coefficient values) and Eq. (2) to (6) for temporal downscaling of
1271 domestic and energy water demands were used in this study, respectively.

1272 **Appendix 2**

1273 Unit conversion to fraction

1274 Hectare (ha): $fraction = ha \cdot 10^4 / GridCellArea_{m^2}$;

1275 Percentage (%): $fraction = \% / 100$;

1276 Class (landcover type): $fraction = 1$, i.e. assumes full 100 % coverage of the grid cell.

1277 **Appendix 3**

1278 Soil depth

1279 Soil depth layers are derived following Burek et al. (2014) in which the total soil depth is horizontally divided in
1280 three layers. The total soil depth is the ‘absolute_depth_to_bedrock’ from SoilGrids250m, whereas root depths of
1281 forest and non-forest are derived from FAO56 and CGLS-LC100 dataset at SoilGrids250m native (~250 m)
1282 resolution (see Section 6.2 for more details). The methodology implemented for the creation of three soil layers
1283 is the following.

1284 Soil depth layer 1 (surface) SD_1 is assumed constant, equal to 50 mm all over the world for consistency with
1285 satellite-derived datasets (satellite signal penetration depth of 50 mm is a good approximation to take into account
1286 different meteorological conditions at different hour of the day globally based on Lv et al. (2018)), and follow Eq.
1287 (A1):

$$1288 SD_1 = 50mm \quad (A1)$$

1289 Soil depth layer 2 (middle) SD_2 depends on the absolute depth to bedrock adb – if it is equal or less than 300 mm
1290 computation follow Eq. (A2), otherwise it is conditional of the root depths as per Eq. (A3), and must meet
1291 requirement from Eq. (A4):

$$1292 SD_2 = (adb - SD_1)/2, adb \leq 300mm \quad (A2)$$

$$1293 SD_2 = \min(\text{root_depth}, (adb - 300mm - SD_1)), adb > 300m \quad (A3)$$

$$1294 SD_2 = 50mm, SD_2 < 50mm \quad (A4)$$

1295 Soil depth layer 3 (bottom) SD_3 , is computed following Eq. (A5):

$$1296 SD_3 = adb - (SD_1 + SD_2) \quad (A5)$$

1297 This set of equations is used twice, once with the root depth of forest area and a second time with the root depth
1298 of non-forested areas, resulting in a total of six soil depth layers computed at SoilGrids250m native resolution.

1299 Soil hydraulic parameters

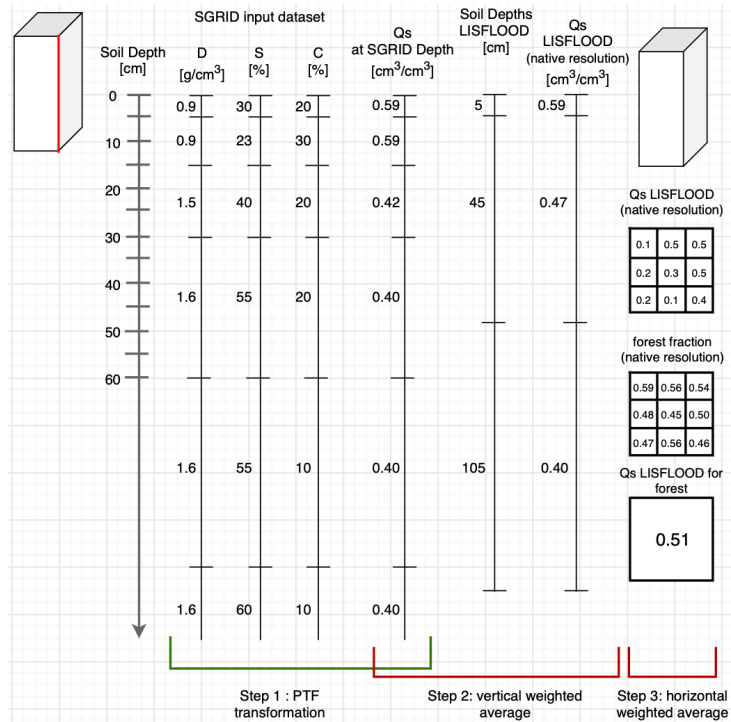
1300 Soil hydraulic parameters are derived by following three main steps (see Figure A1).

1301 First, soil hydraulic properties are derived at native resolution by applying pedotransfer functions (PTFs) to each
1302 SoilGrids250m soil characteristics layer at each available depth. Pedotransfer functions translate field measured
1303 soil information (such as soil texture, pH and structure) into proprieties and parameters needed to describe soil
1304 processes. The PTFs implemented here are the ones proposed by Toth et al. (2015). Users can decide to derive
1305 soil proprieties from different PTFs, but the general principle presented here remains valid.

1306 Second, the soil hydraulic parameters calculated at SoilGrids250m depths are vertically downscaled to the model
1307 soil depth (previously computed) by weighted average (Figure A1, Step 2 with theta saturated as an example) at
1308 the native SoilGrids250m resolution (~250 m).

1309 Third, the soil hydraulic parameters at the final soil depths are upscaled from native to final resolution by average
1310 using forest and non-forest fraction layers as weights (Figure A1, Step 3).

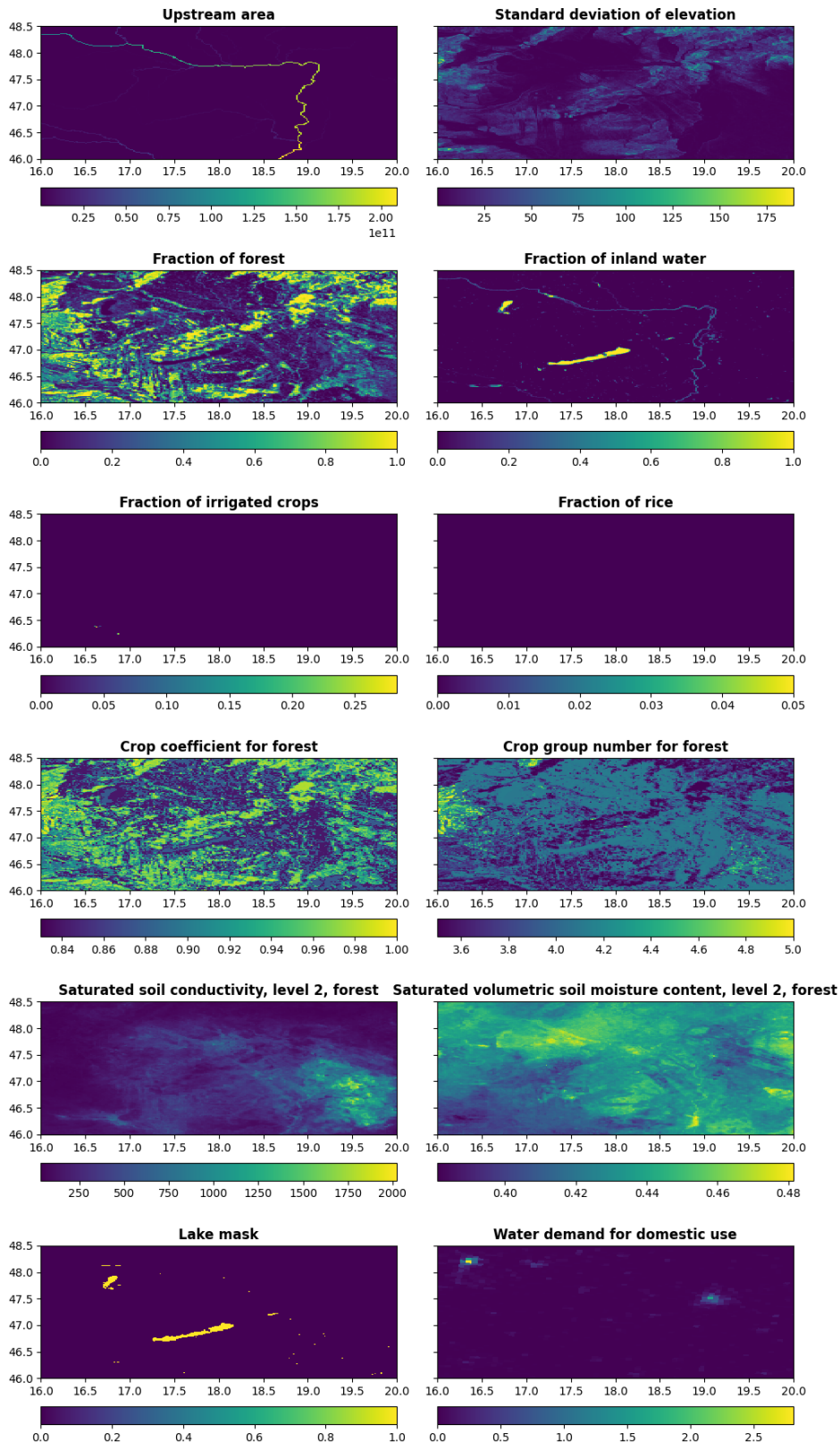
1311



1312
1313 **Figure A1. Creation of theta saturated parameter 'Qs' using SoilGrids250m dataset 'SoilGRID' and forest**
1314 **fraction.**

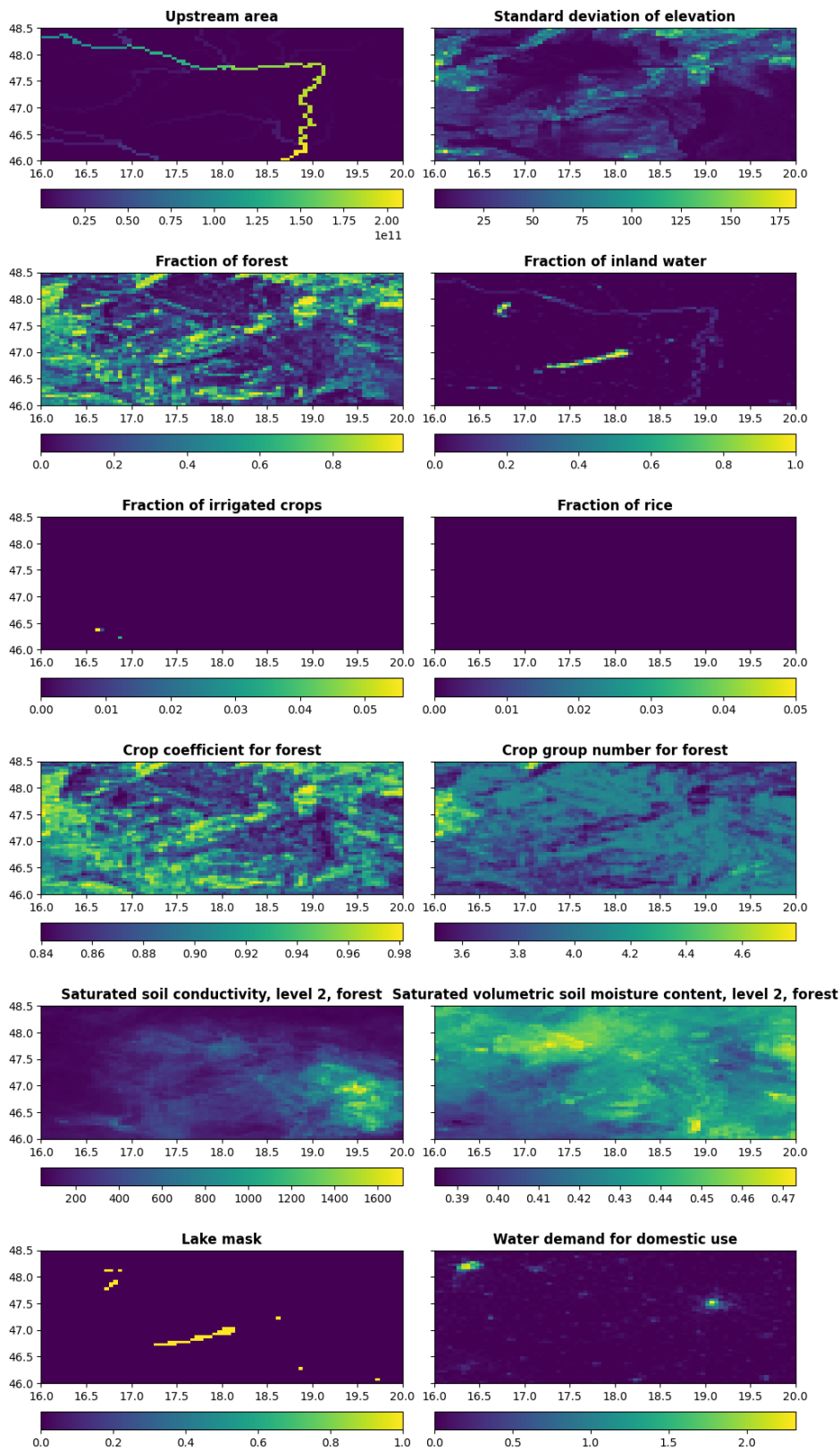
1315 **Appendix 4**

1316 Here more regional examples of the most interesting surface fields of CEMS_SurfaceFields_2022 are provided to
1317 show what level of details is available at each resolution and field, and to emphasise consistency through all the
1318 fields that is the most valuable requirement when running any type of surface model.
1319



1320
1321
1322
1323
1324
1325

Figure A2. Upstream drainage area in square meters, standard deviation of elevation in meters, fraction of forest, fraction of inland water, fraction of irrigated crops, fraction of rice, crop coefficient for forest, crop group number for forest, saturated soil hydraulic conductivity for forested areas of soil depth layer 2 in mm per day, saturated volumetric soil moisture (i.e. water) content for forested areas of soil depth layer 2, lake mask, and water demand for domestic use at 1 arcminute (~1.9 km at the equator) resolution for Danube River area in Europe.



1326
1327

Figure A3. Same as Figure A2, but at 3 arcminute (~5.6 km at the equator) resolution for Danube River area in Europe.

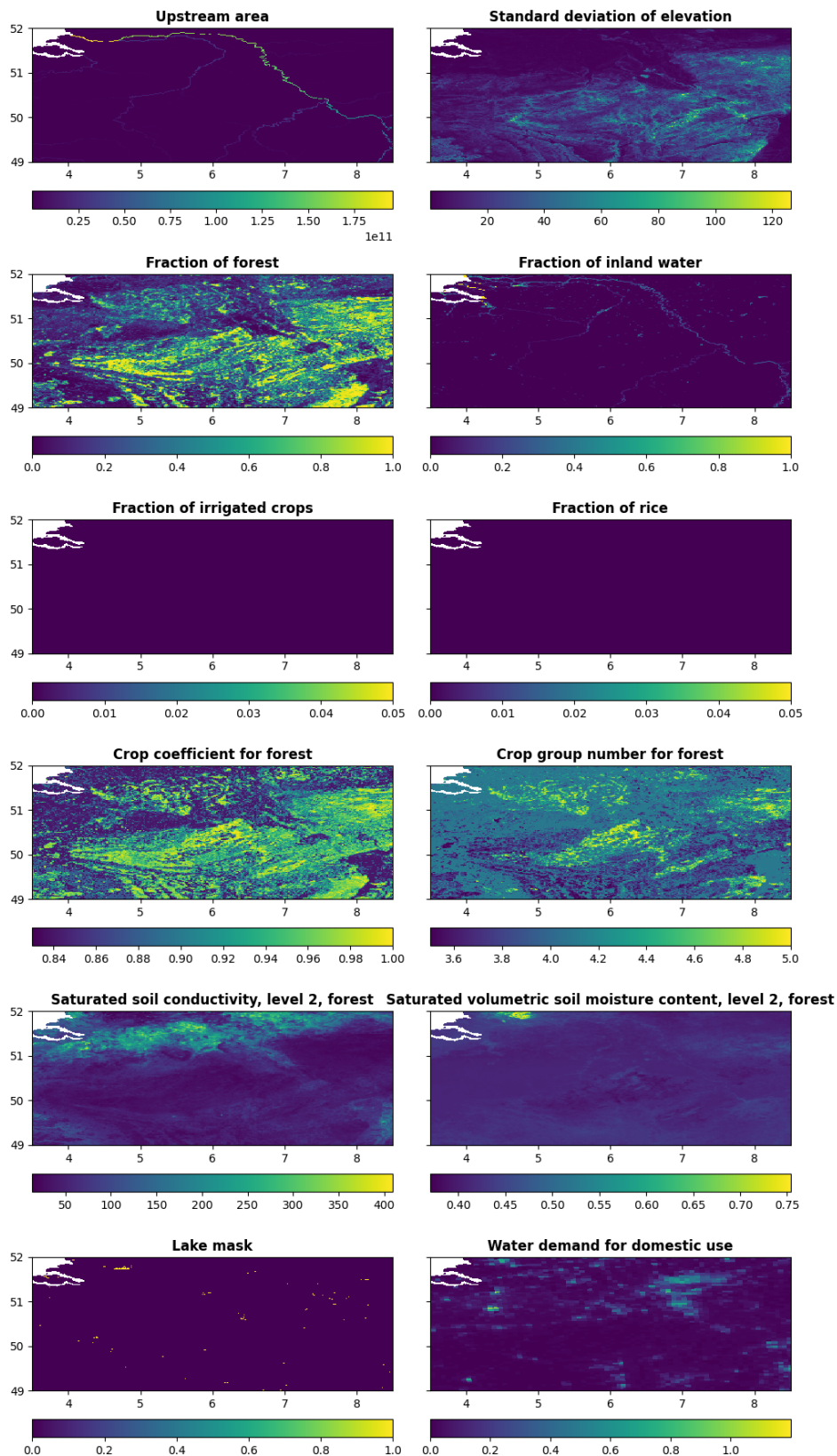
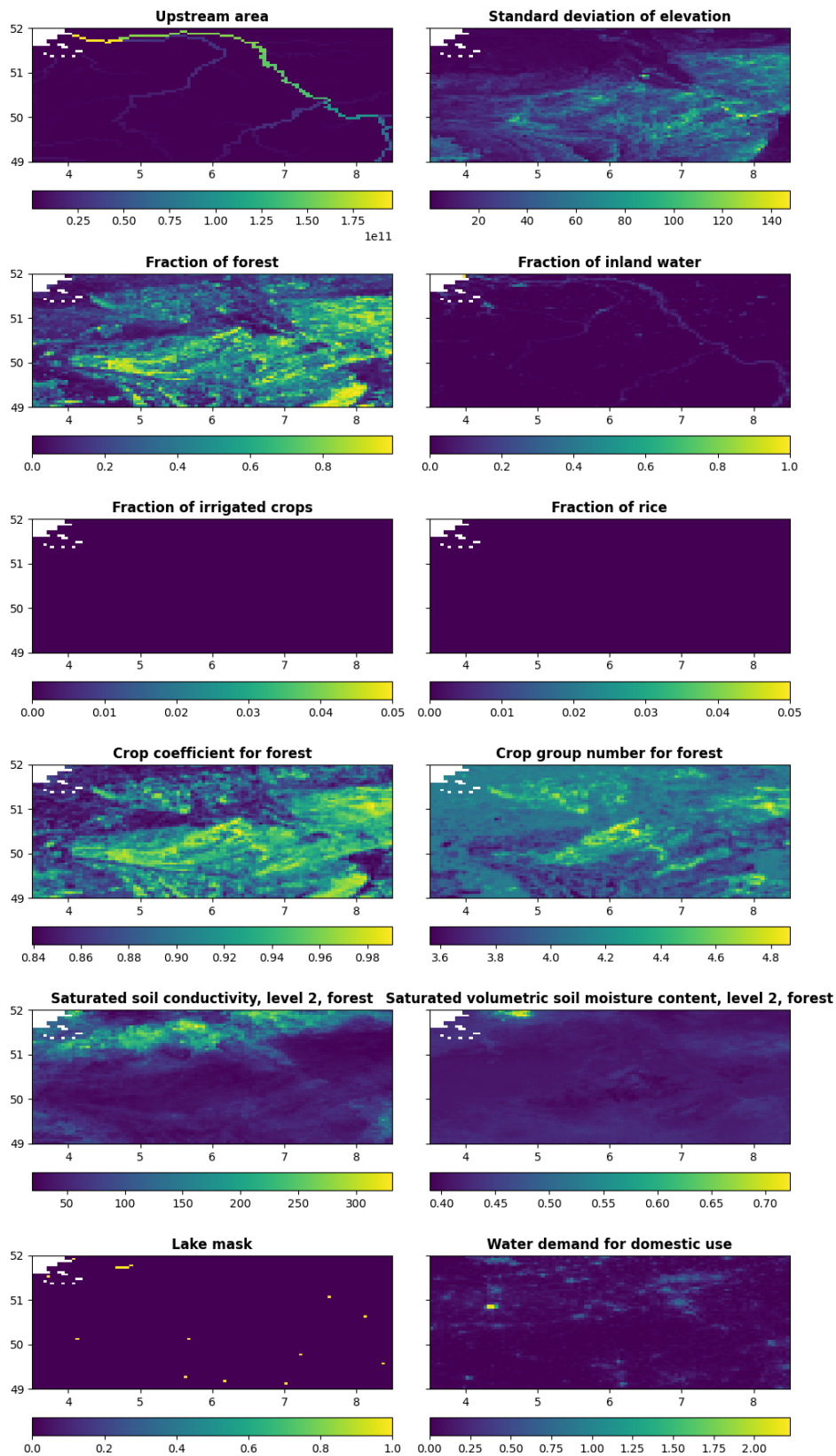


Figure A4. Same as Figure A2, but at 1 arcminute (~1.9 km at the equator) resolution for Rhine River area in Germany.

1328
1329



1330
1331

Figure A5. Same as Figure A2, but at 3 arcminute (~5.6 km at the equator) resolution for Rhine River area in Germany.

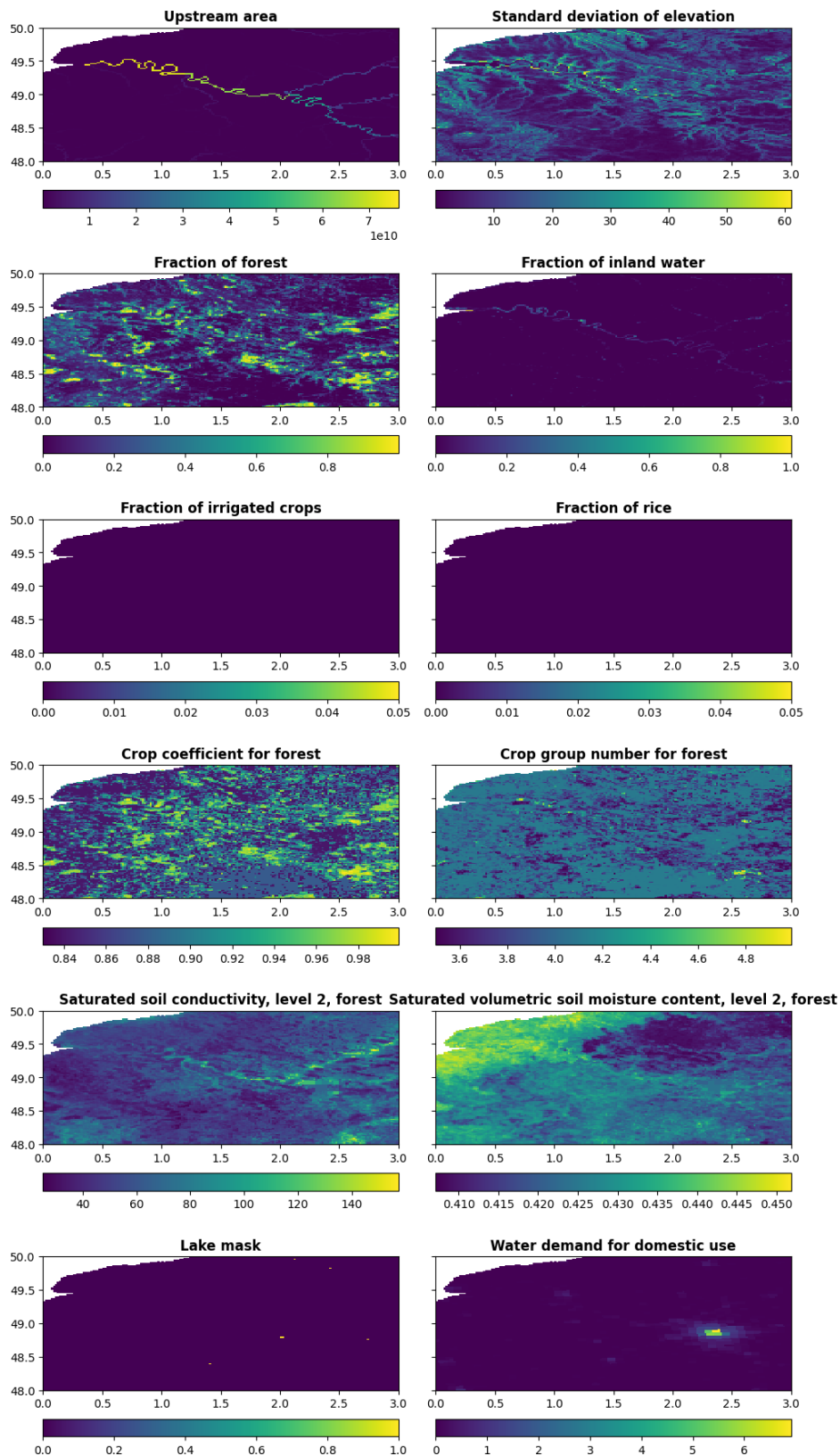


Figure A6. Same as Figure A2, but at 1 arcminute (~1.9 km at the equator) resolution for Seine River area in France.

1332
1333

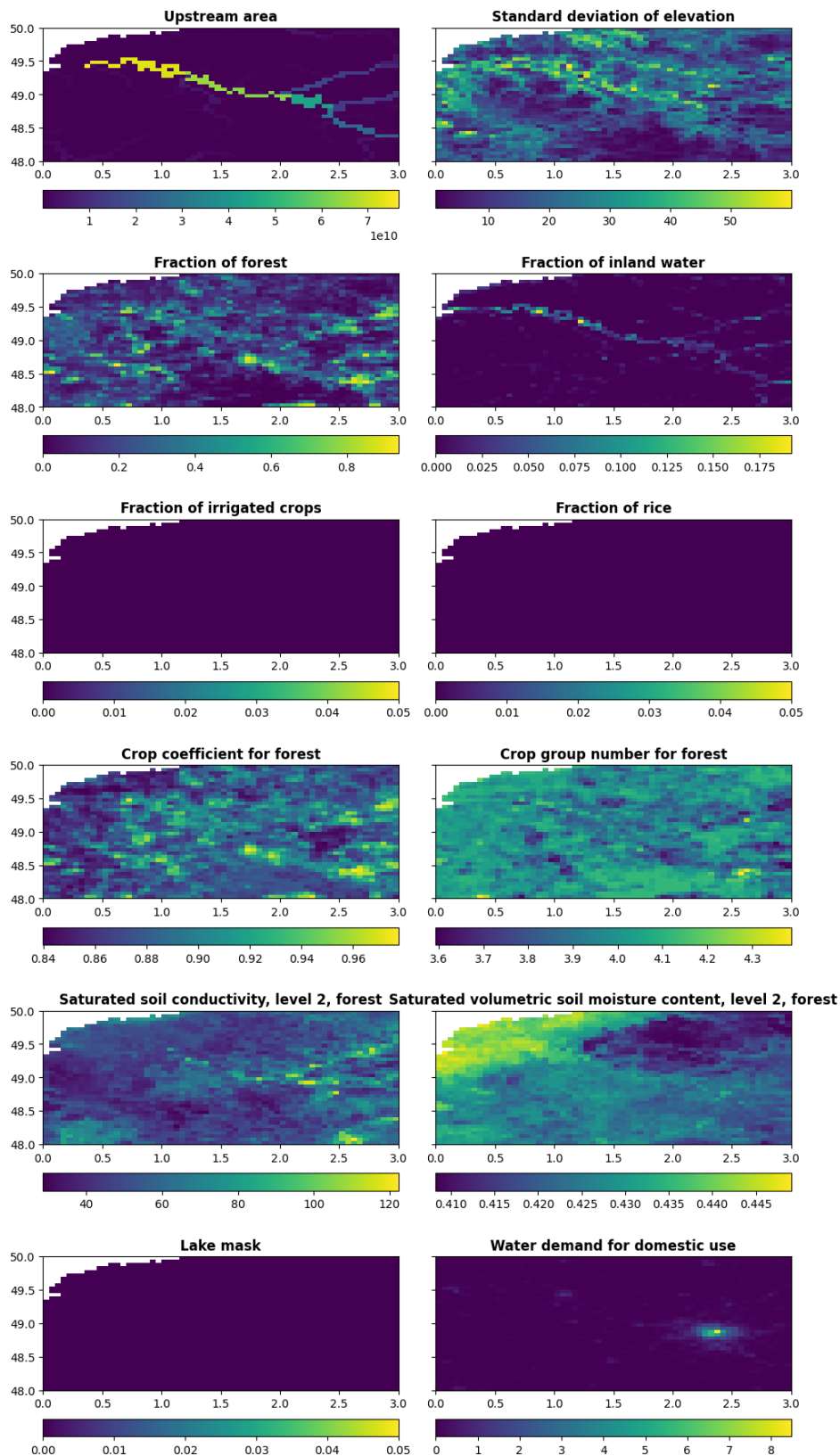


Figure A7. Same as Figure A2, but at 3 arcminute (~5.6 km at the equator) resolution for Seine River area in France.

1334
1335

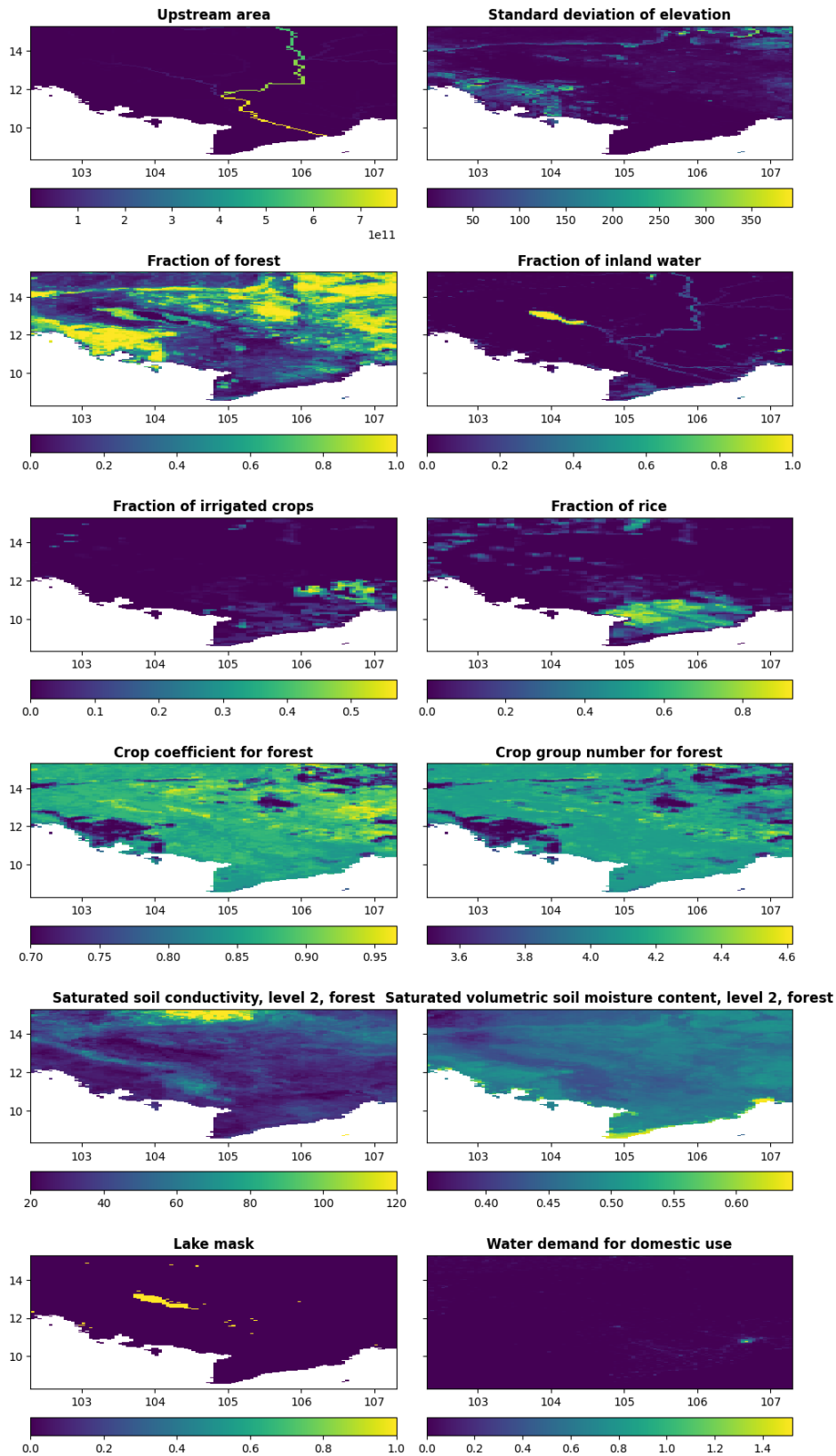


Figure A8. Same as Figure A2, but at 3 arcminute (~5.6 km at the equator) resolution for Seine Mekong area in Cambodia.

1336
1337
1338

1339
1340